Coherent Light Scattering from Photonic Crystals and Phase Lattices

Dissertation

zur Erlangung des Grades eines Doktors

der Naturwissenschaften

vorgelegt von

Dipl.-Phys. Björn Christian Brüser

geboren am 12.3.1981

in Siegen

eingereicht beim Department für Physik

der Naturwissenschaftlich-Technischen Fakultät

der Universität Siegen

Siegen 2011

Gutachter:

Prof. Dr. Ullrich Pietsch (U Siegen)

Prof. Dr. Susanna Orlic (TU Berlin)

Tag der mündlichen Prüfung: 26.07.2011

Zusammenfassung

Die vorliegende Arbeit befasst sich mit der Diffraktion von sichtbarem, kohärentem Licht sowohl an dreidimensionalen photonischen Kristallen als auch an dreidimensionalen photonischen Raumgittern. Der Unterschied in den beiden letztgenannten Strukturen liegt in der Darstellung der Brechungsindexverteilung, die sich in beiden Fällen durch eine periodische Modulation in der Größenordnung weniger Mikrometer in drei Dimensionen auszeichnet. Während sich diese für die photonischen Kristalle unstetig verhält, vergleichbar mit einer periodischen dreidimensionalen Stufenfunktion, ändert sich die Brechungsindexverteilung für photonische Raumgitter stetig und ist etwa durch eine sinusförmige Funktion in drei Dimensionen zu beschreiben.

In dieser Arbeit werden die zuvor beschriebenen photonischen Kristalle/Raumgitter auf ihre Streueigenschaften untersucht. Diese Untersuchung geschieht in erster Linie auf experimentellem Wege, allerdings wird eine Modellierung der Streukurven unter dem Gesichtspunkt der Anwendbarkeit von approximativen Lösungen ebenso diskutiert. Dazu wird zunächst skizziert welche rigorosen numerischen Methoden die Maxwellgleichungen lösen können. Im Anschluss daran werden approximative Lösungen diskutiert, die insbesondere vom Brechungsindexhub bzw. der -modulation der jeweiligen Gitter abhängen. Des Weiteren wird eine Einführung in die verwendete Streugeometrie gegeben sowie der experimentelle Arbeitsplatz erklärt.

Die photonischen Kristalle der sogenannten "Woodpile-struktur" werden in dieser Arbeit auf ihre Brechungsindexabhängigkeit untersucht. Dies geschieht auf experimentellem Wege durch Infiltration spezieller Brechungsindexflüssigkeiten. Es wird zudem nach einem Übergang bzw. einer Klassifikation von verschiedenen Streuregimen gesucht. Insbesondere wird der Übergang von der sogenannten "kinematischen" Streuung, also der klassischen Lauebeugung, zu einem "dynamischeren" Streuregime untersucht. Um die experimentellen Ergebnisse zu untermauern, werden auf der rigorosen Lösung der Maxwellgleichung basierende Simulationen vorgestellt, die die experimentelle Einteilung der Regimes weitestgehend bestätigen.

Wegen ihrer abweichenden Brechungsindexmodulation werden die holographischen Raumgitter separat untersucht. Da der Brechungsindexhub vergleichsweise gering ist und eine entsprechende Untersuchung bereits publiziert wurde, wird auf einen Vergleich mit einer rigorosen Lösung verzichtet. Stattdessen wird eine approximative Lösung diskutiert, die ins-

besondere auf der kinematischen Streutheorie beruht. Es wird weiterhin gezeigt, dass mit diesem relativ simplen Ansatz die Streuung an den gegebenen Strukturen gut beschrieben werden kann. Lediglich für die Beschreibung der Streueffizienzen ist dieses Modell nicht anwendbar.

Abstract

The present work deals with the diffraction of visible, coherent light from three-dimensional photonic crystals as well as three-dimensional phase lattices. The difference between the latter structures is their refractive index modulation. Although the periodic modulation of the refractive index in three dimensions is in both cases of the order of a few micrometers, the photonic phase lattices have a continuous modulation of the refractive index while the photonic crystals have a discontinuous modulation, respectively.

The scattering properties of the photonic crystals / phase lattices are investigated in this thesis. The major investigation is done experimentally, but a modelling of the scattering curves is done as well. This modelling focuses on the applicability of approximate solution approaches. Therefore, a short primer on the numerical solution methods of Maxwell's equations is given. Subsequently, approximate solutions are discussed where the attention is especially directed to the dependence and strength of the refractive index modulation. Furthermore, a short introduction of the used scattering geometry is given as well as a depiction of the experimental setup.

The scattering properties of the photonic crystals, given by the so-called 'woodpile structure', are specifically investigated regarding their refractive index dependence. Experimentally, this is achieved via infiltration of special refractive index liquids. Moreover, a classification of scattering regimes is sought which is based on the refractive index difference. In particular a transition of the so-called 'kinematic' scattering which can be described by the Laue equations to a more 'dynamic' scattering regime is investigated. In order to substantiate the experimental findings, simulations based on a rigorous numerical solution of Maxwell's equations are presented. Those results confirm the experimental classification of the scattering regimes.

Due to their differing refractive index modulation the holographic phase lattices are investigated in a separate part. Since the maximum refractive index difference is much smaller than the one for the previously mentioned photonic crystals and since such an investigation has been already published, a comparison of the experimental scattering efficiency of a phase lattice with a rigorous solution is omitted in favour of an approximate solution approach. This approach relies on the kinematic scattering theory. Furthermore, it is shown that this rather simple approach can well explain the light scattering from the considered structures.

Merely, the scattering efficiencies cannot be described properly by the model.

Contents

Eidesstattliche Erklärung

Curriculum Vitae

Preface

Diffraction is most pronounced for objects of a size comparable to the wavelength of the incident waves. Since Laue and co-workers' first experimental verification of this effect concerning X-rays and crystals in 1912, which are both characterized by wavelengths and dimensions of the same order, this phenomenon has become a powerful tool to investigate the structure of crystals and crystalline materials. The use of X-rays as investigation probes has the advantage of being a non-destructive method.

A photonic crystal (PCs) is basically every type of material that has a periodic modulation of its refractive index where the magnitude of the modulation is in the order of the wavelength of light. The modulation can be in one, two or three dimensions. Three-dimensional PCs have to be created artificially since they do not occur in nature. Visible light is the sort of electromagnetic wave that has the proper wavelength to cause diffraction when incident on a photonic crystal. A comparison of the classical Laue diffraction case for X-rays and the diffraction from PCs for visible light reveals that this cannot be reduced to a mere scaling problem and a subsequent one-to-one transfer of knowledge obtained from the X-ray regime is not valid in general. In [1] a first comparison of the diffraction of light and X-rays is given.

Previous works regarding light interaction with PCs

Nowadays most of the research and development concerning photonic crystals is directed towards creating crystals with a so-called photonic bandgap. That is why PCs are sometimes also called 'Photonic Bandgap Materials'. The photonic bandgap is the photonic counterpart to the electronic bandgap found in semiconductors [2]. Likewise the propagation of photons of a certain energy range is forbidden inside a PC with a photonic bandgap.

The first ones to introduce the concept of photonic crystals were Eli Yablonovitch [3] and Sajeev John [4] in 1987. In his article Yablonovitch mentions that one-dimensional periodic lattices of refractice index are used as reflective parts in Fabry-Perot resonators. Here, the propagation of light of a specific incident direction is forbidden, so Yablonovitch concluded that for a three-dimensional periodic structure the propagation of light incident from any direction is forbidden. Such kind of devices would be suitable to control spontaneous emission in semiconductor lasers. The paper by Sajeev John deals with the strong localization of light

where the terms dielectric superlattice and photonic bandgap are discussed.

Light scattering experiments which have been reported mostly focused on photonic crystals made of small $(200 - 700\text{nm})$ spherical polymer colloids (cf. [5], [6], [7], [8] and [9]). The purpose of those experiments was mostly the analysis of the PC quality and not a specific investigation of the diffraction efficiency. Regarding photonic crystals made by another technique, such as 'direct laser writing', Laue diffraction experiments have been reported [10]. However, this was used for structure determination and not for a basic interpretation of the scattering properties. In this thesis the light scattering from PCs follows mainly the approach developed in [11]. Further works concerning the so-called woodpile-structured photonic crystals are for example given by [12] and [13].

Another relevant issue, which is related to this thesis, is the diffraction from photonic lattices. They differ from classic PCs by their refractive index modulation. An approach of describing the scattering of a one-dimensional lattice was given by [14]. Moreover, an experimental and theoretical description regarding three-dimensional lattices can be found in [15].

Outline of the presented work

This work is embedded in the framework of the $BMBF^1$ funded project $NAMIROS^2$. The idea is to use photonic crystals as preselective diffractive-optical elements inside a new optical sensor by exploiting the well-known Laue diffraction effect. Required for this project is firstly the production of photonic lattices/crystals [16], secondly the analysis of the interaction of light with these lattices and finally the implementation of a prototype sensor system. The work presented in this thesis deals with the second part.

The research and development of photonic crystals where a photonic bandgap is a desired feature is characterized by a rather large $(\Delta n > 2)$ refractive index difference while compared to the research of the diffraction mechanism in this thesis a rather small $(\Delta n < 0.25)$ refractive index difference is considered. This is done because the validity of the Laue diffraction effect strongly depends on this Δn. Furthermore, a very detailed analysis of the refractive index dependence of the PC on the scattering process will be made.

Two different photonic structures will be discussed throughout the thesis, namely the woodpile-structured photonic crystals (WP PCs) and the photonic phase lattices. In chapter 1 the method of preparation and the crystallography of those structures will be discussed. Then attention is directed to the interaction of electromagnetic waves with periodic media which can be basically described by Maxwell's equations (cf. chapter 2). Subsequently, the

---

[1]German acronym: Bundesministerium für Bildung und Forschung
[2]German acronym: Nano- und Mikrostrukturierung von Polymeren und Nanokompositen als Raumgitter für die optische Sensorik

scattering geometry is explained in chapter 3 where the scattering curves used to describe the scattering properties of the PCs is introduced as well. Chapter 4 shortly summarizes the experimental setup while in chapter 5 the theoretical simulations used to describe light scattering from PCs are presented. Moreover, the experimental results are analysed by comparing them to previously discussed scattering models (cf. chapter 6 and 7). Eventually, the results will be summarized in chapter 8 while a short outlook is given in chapter 9.

1. Properties of Photonic Crystals

Photonic crystals (PCs) are artificial materials characterized by a periodic modulation of the refractive index. For photonic crystals the typical scale of periodicity is of the order of the wavelength of light. In order to describe the symmetry of PCs notations known from crystallography can be used which were originally developed for the characterization of usual crystals to describe the arrangement of atoms in a lattice, it can be easily adapted to photonic crystals.

Therefore, basic concepts of crystallography are shortly introduced at first (cf. [17]). This is necessary for the further understanding of the context. Figure 1.1 shows the basic composi-
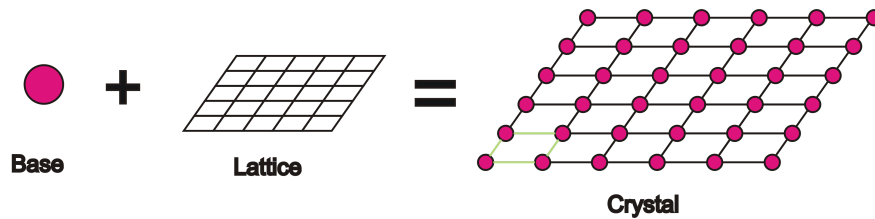
Fig. 1.1.: A crystal structure can be put together by a base and a lattice. The picture shows a case in two dimensions.

tion of a crystal, namely a lattice and a basis. The lattice is a mathematical construction that contains information about the periodicity and translation symmetry of a crystal whereas the basis is located at a lattice point. The basis is responsible for the physical aspects. For usual crystals it can be a single atom, molecules and in the case of PCs a refractive index modulation. A primitive unit cell of a crystal is the part sketched in green colour in figure 1.1. It is the smallest building block of a crystal. The boundaries consist of the shortest possible vectors that span the lattice.

1.1. Dielectric function

In general the interaction of electromagnetic waves with a material depends on the distribution of the dielectric function (permittivity) $\epsilon(\mathbf{r})$ and magnetic permeability $\mu(\mathbf{r})$. However, for all PCs considered in this work the magnetic permeability $\mu(\mathbf{r})$ is equal to one. The refractive index $n(\mathbf{r})$ which is defined as $n(\mathbf{r}) = \sqrt{\epsilon(\mathbf{r}) \cdot \mu(\mathbf{r})}$ reduces thus to a modulation of

the dielectric constant $n(\mathbf{r}) = \sqrt{\epsilon(\mathbf{r})}$. That is why it is possible to describe a PC either by a periodic permittivity modulation or equivalently by a periodic refractive index modulation. Figure 1.2 shows a subdivision of PCs depending on their dimensionality. While a variation

(a) 1D-multilayer structure (b) 2D-rod-like structure (c) 3D-structure
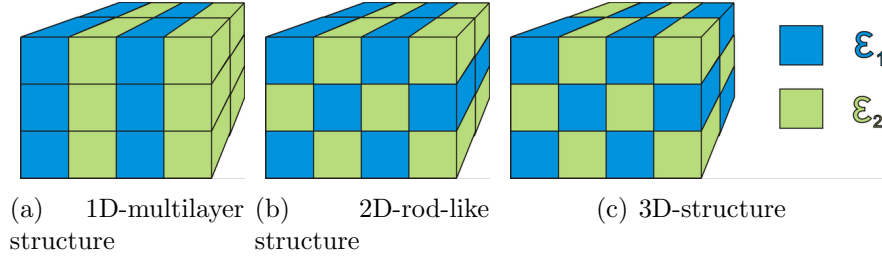
Fig. 1.2.: Definition of one-, two- and three-dimensional photonic crystals.

in one dimension is usually called a multilayer, an additional variation in another dimension results in a rod-like structure. A full three-dimensional photonic crystal has a permittivity modulation in each dimension (cf. [18] and [19]).

In addition to the dimensionality a further distinction into discontinuous (cf. figure 1.2) and continuous modulations (cf. figure 1.3) can be made. For the first case this means that there are sharp boundaries that separate regions of different dielectric constants as defined by (1.1).

$$\epsilon(\mathbf{r}) = \begin{cases} \epsilon_1, & \text{for } \mathbf{r} \text{ in region 1,} \\ \epsilon_2, & \text{for } \mathbf{r} \text{ in region 2.} \end{cases} \tag{1.1}$$

In contrast to discontinuous modulations, the dielectric function $\epsilon(\mathbf{r})$ can change smoothly. This means that there are no sharp transitions like shown in figure 1.2. This can be for example accomplished if the dielectric function has a sinusoidal modulation like

$$\epsilon(\mathbf{r}) = \epsilon_0 + \Delta\epsilon \cdot \sin(\mathbf{K} \cdot \mathbf{r}). \tag{1.2}$$

The discontinuous dielectric modulation reflects the situation for the later introduced woodpile-structured photonic crystal, while the so-called phase lattices (trigonal holographic photonic crystals, cf. 1.2) have a smooth modulation.

1.2. Phase lattices

In this section the term 'phase lattice' is introduced and brought into context. Then attention is directed to its manufacturing process, with a subsequent discussion of its crystallographic properties.
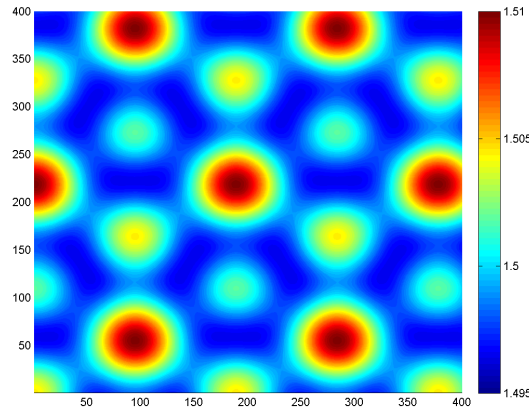
Fig. 1.3.: Example of a smoothly varying dielectric function. For a better visualization this picture just shows a slice through a 3D structure.

From literature [20] the terms 'phase grating' and 'amplitude grating' are already well-known and are special cases of the more general diffraction grating [21]. Whereas a phase grating modulates the phase of the incident light wave, the amplitude grating changes the amplitude of the incident light waves respectively.

The phase gratings are characterized by a periodic modulation of the refractive index. These modulations are just in one or two dimensions as implied by the choice of the word 'grating'.

The structures analysed in this work are similarly created as the phase gratings (holographic approach), however they have a refractive index modulation in three dimensions and therefore the term 'three-dimensional phase lattice' or simply 'phase lattice' is used.

1.2.1. Fabrication process

The phase lattice consists of a base material which is a so-called photo polymer. On the one hand there are several commercial vendors[3,4] that are able to provide such kind of photo polymers, on the other hand academic research groups are also developing such kind of polymers within the framework of a joint research project (NAMIROS) by themselves.

In the following the general process of lattice creation is described independently of the peculiarities of different polymers. Initially the photo polymer is either given as a layer with a certain thickness sandwiched between two glass plates (commercial polymers) or it is spin-coated onto a glass substrate (NAMIROS polymers). In both cases the photo polymer layer has a constant refractive index before processing.

---

[3]http://www.stxaprilis.com/
[4]http://www.inphase-tech.com/

Due to the light sensitivity of the polymer the modulation of the permittivity can be generated by irradiation with laser light. When the incident laser light intensity crosses a certain threshold an alteration of the polymer chains of the material is the result. This induced polymerization process is sufficient to cause a modulation of the refractive index. In literature the use of interfering lasers as a creation technique for photonic lattices is already documented (cf. [22] and [23]). The considered three-dimensional photonic lattices were created by the so-called umbrella-like beam configuration [24].

In the following a short reminder of interference patterns in one and two dimensions and their effect on a photo polymer are given before the more complicated umbrella-like configuration and its subsequent created lattice will be explained.

Interference in one and two dimensions

The illumination of a photo polymer with one laser beam would cause a large-scale refractive index change without periodic modulation. However, with the use of multiple laser beams an intensity interference pattern can be created and superposed locally with the material. Firstly, a laser beam is split into two beams to ensure a constant phase relation between both beams. If one takes a look at the intensity pattern of the light of these two interfering laser beams, while assuming the laser light to behave like plane waves, then one can see that it is cosinusoidally modulated (cf. (1.3)).

$$\mathbf{E}_1 = \mathbf{E}_{1,0} \exp\left(i \cdot \mathbf{k}_1 \mathbf{r}\right) \quad \mathbf{E}_2 = \mathbf{E}_{2,0} \exp\left(i \cdot \mathbf{k}_2 \mathbf{r}\right)$$

$$I_{1D} = |\mathbf{E}_1 + \mathbf{E}_2|^2 = |\mathbf{E}_{1,0}|^2 + |\mathbf{E}_{2,0}|^2 + \mathbf{E}_{1,0} \cdot \mathbf{E}_{2,0} \cdot \cos\left((\mathbf{k}_1 - \mathbf{k}_2) \cdot \mathbf{r}\right) \tag{1.3}$$

The direction of modulation is given by the difference vector $\mathbf{k}_1 - \mathbf{k}_2$ of the two laser beams and is therefore periodic in one dimension. A two-dimensional periodic modulation is obtained for three non-coplanar laser beams. This is comprehensible by considering (1.4). The intensity pattern depends on three difference vectors $\Delta\mathbf{k}_{12} = \mathbf{k}_1 - \mathbf{k}_2$, $\Delta\mathbf{k}_{13} = \mathbf{k}_1 - \mathbf{k}_3$ and $\Delta\mathbf{k}_{23} = \mathbf{k}_2 - \mathbf{k}_3$ which are always coplanar so that there is only a change in two dimensions.

$$I_{2D} = |\mathbf{E}_1 + \mathbf{E}_2 + \mathbf{E}_3|^2 = |\mathbf{E}_{1,0}|^2 + |\mathbf{E}_{2,0}|^2 + |\mathbf{E}_{3,0}|^2 + \mathbf{E}_{1,0} \cdot \mathbf{E}_{2,0} \cdot \cos\left((\mathbf{k}_1 - \mathbf{k}_2) \cdot \mathbf{r}\right) + ...$$

$$... + \mathbf{E}_{2,0} \cdot \mathbf{E}_{3,0} \cdot \cos\left((\mathbf{k}_2 - \mathbf{k}_3) \cdot \mathbf{r}\right) + \mathbf{E}_{1,0} \cdot \mathbf{E}_{3,0} \cdot \cos\left((\mathbf{k}_1 - \mathbf{k}_3) \cdot \mathbf{r}\right) \tag{1.4}$$

In order to have a periodic variation in all three dimensions, it is necessary to have an interference of four laser beams. It is clear that by adding more laser beams one cannot increase the dimensionality any more, it is even possible to destroy the periodicity by adding more beams [25].

Polymer response

The parts of the photo polymer where the threshold intensity is crossed undergo a change in the permittivity. The higher the intensity of the laser beams is the higher the change in the permittivity will be. For the considered photo polymers this relation is linear up to a certain illumination energy, for a higher energy the polymer chains will be destroyed. Therefore, it is possible to inscribe a (co)sinusoidal permittivity distribution inside the polymer in one, two or three dimensions due to the (co)sinusoidal intensity pattern of the interfering beams. In figure 1.3 a two-dimensional slice through a three-dimensional permittivity modulation is depicted. A more detailed discussion about the chemistry of the polymers with further references can be found in [15].

Geometry of the umbrella-like beam configuration

For inscribing three-dimensional structures a three-dimensional intensity pattern needs to be created and superposed with the photo polymer. Therefore, one usually starts by using one laser beam and splitting it into four beams. This ensures that the condition $|\mathbf{k}_1| = |\mathbf{k}_j|$ with $j = 1...4$ holds true. The beams are thus superposed in the umbrella-like configuration. This means that one beam will be directed parallel to the surface normal (central beam) and the other three will be equally distributed around this beam (non-central beams). In the umbrella-like configuration the non-central beams form a cone. It will be shown that the apex-angle θ of this cone is crucial for the properties of the crystal.

Previous works have proved (cf. [26], [22], [23] and [24]) that the resulting structure inside the polymer inscribed by the used beam configuration is trigonal. In order to make this clear one has to take a deeper look into the umbrella-like configuration.

By using spherical-like angles θ (cf. figure 1.4) and $\phi_n = 2n\pi/3$ (azimuthal angle) with $n = 0, 1, 2$ one can define the incoming beam directions:

$$\mathbf{k}_n = -k \cdot \begin{pmatrix} \sin\theta\cos\phi_n \\ \sin\theta\sin\phi_n \\ \cos\theta \end{pmatrix}, \quad \mathbf{k}_3 = -k \cdot \begin{pmatrix} 0 \\ 0 \\ 1 \end{pmatrix}, \quad n = 0, 1, 2 \tag{1.5}$$

The apex-angle θ is equal for the beams $n = 0, 1, 2$. Due to the direction of the vectors it is not equal to the angle between $\mathbf{k_4}$ and each one of the three vectors $\mathbf{k_n}, (n = 0, 1, 2)$ but it is connected via $\sphericalangle(\mathbf{k}_n, \mathbf{k}_3) = \pi - \theta$ (this should be mentioned because this definition differs from the one given in earlier cited references). Out of the four beam directions one can introduce non-coplanar reciprocal lattice vectors $\mathbf{a}_1^*$, $\mathbf{a}_2^*$ and $\mathbf{a}_3^*$. These reciprocal lattice
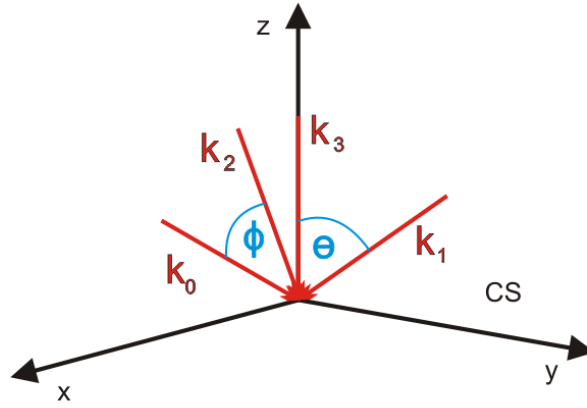
Fig. 1.4.: Definition of incoming beam directions in the umbrella-like configuration.

vectors can be used to describe the symmetry of the interference pattern.

$$\mathbf{a}_1^* = \mathbf{k}_0 - \mathbf{k}_3; \quad \mathbf{a}_2^* = \mathbf{k}_1 - \mathbf{k}_3; \quad \mathbf{a}_3^* = \mathbf{k}_2 - \mathbf{k}_3 \tag{1.6}$$

Inserting the definitions from (1.5) into (1.6) yields:

$$\mathbf{a}_1^* = \frac{k}{2} \cdot \begin{pmatrix} -2\sin\theta \\ 0 \\ 2(1-\cos\theta) \end{pmatrix}; \quad \mathbf{a}_2^* = \frac{k}{2} \cdot \begin{pmatrix} \sin\theta \\ -\sqrt{3}\sin\theta \\ 2(1-\cos\theta) \end{pmatrix}; \quad \mathbf{a}_3^* = \frac{k}{2} \cdot \begin{pmatrix} \sin\theta \\ \sqrt{3}\sin\theta \\ 2(1-\cos\theta) \end{pmatrix} \tag{1.7}$$

Independent of θ, the vectors $\mathbf{a}_1^*$, $\mathbf{a}_2^*$ and $\mathbf{a}_3^*$ have the same length and the same angle with each other which proves that the reciprocal lattice is indeed trigonal. The angle α between two reciprocal lattice vectors is given by:

$$\cos\alpha = \frac{\mathbf{a}_i^* \cdot \mathbf{a}_j^*}{\left|\mathbf{a}_i^* \cdot \mathbf{a}_j^*\right|} = \frac{1}{2}\left(\frac{3\cos^2\theta - 4\cos\theta + 1}{2 - 2\cos\theta}\right), \quad i \neq j \tag{1.8}$$

The connection between real space and reciprocal space is given by the standard equations:

$$\mathbf{a}_1 = \frac{2\pi}{V_{\text{Cell}}^*}\mathbf{a}_2^* \times \mathbf{a}_3^* \quad \mathbf{a}_2 = \frac{2\pi}{V_{\text{Cell}}^*}\mathbf{a}_3^* \times \mathbf{a}_1^* \quad \mathbf{a}_3 = \frac{2\pi}{V_{\text{Cell}}^*}\mathbf{a}_1^* \times \mathbf{a}_2^* \tag{1.9}$$

Where V_{Cell}^* is given by $V_{\text{Cell}}^* = \mathbf{a}_1^* \cdot (\mathbf{a}_2^* \times \mathbf{a}_3^*)$ and $\mathbf{a}_i \cdot \mathbf{a}_j^* = 2\pi\delta_{ij}$. In order to receive information about the lattice in real space one has to substitute the reciprocal lattice vectors in (1.9) with the formulas given in (1.7). By also substituting $k = 2\pi/\lambda$ one gets the real space

vectors as a function of the wavelength of the inscribing laser beams and the apex angle θ.

$$\mathbf{a}_1 = \frac{\lambda}{3} \cdot \begin{pmatrix} -\frac{2}{\sin\theta} \\ 0 \\ \frac{1}{1-\cos\theta} \end{pmatrix} \qquad \mathbf{a}_2 = \frac{\lambda}{3} \cdot \begin{pmatrix} \frac{1}{\sin\theta} \\ -\frac{\sqrt{3}}{\sin\theta} \\ \frac{1}{1-\cos\theta} \end{pmatrix} \qquad \mathbf{a}_3 = \frac{\lambda}{3} \cdot \begin{pmatrix} \frac{1}{\sin\theta} \\ \frac{\sqrt{3}}{\sin\theta} \\ \frac{1}{1-\cos\theta} \end{pmatrix} \qquad (1.10)$$

Once more one can see that the angles between the vectors are the same as well as their length. So this means that the lattice in real space is also trigonal.

1.2.2. Crystallography of phase lattices

In the previous section it was shown that the resulting lattice vectors of the three-dimensional photonic lattices have trigonal symmetry. In this part focus is directed on the crystallographic structure. Although the resulting structure has a smooth variation of the permittivity and no 'photonic atoms' one defines the crystallographic structure by introducing a lattice with lattice points corresponding to the points of maximum permittivity change.

In figure 1.5(a) the general form of the trigonal structure is depicted. Visible are here the lattice points and not the permittivity distribution. The structure can be easily understood if one decomposes the structure into a set of two-dimensional layers. The lattice points are hexagonally arranged for each layer. The next two layers are also hexagonal but shifted as it can be seen in figure 1.5(b) which is a top view along the stacking direction of the layer of the structure. There are multiple equivalent crystallographic notations that can be used to
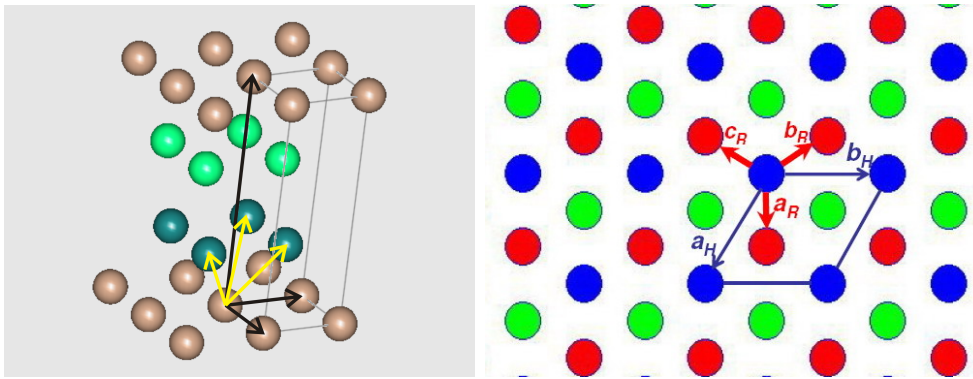
(a) Isometric view. Trigonal (yellow) and hexagonal(black) base vectors.

(b) Top view along the hexagonal $\mathbf{c}_H$-vector. Trigonal (red) and hexagonal(blue) base vectors [27].

Fig. 1.5.: Crystallographic arrangement of the trigonal lattice structure with hexagonal and trigonal base vectors.

describe the trigonal structure. In order to employ the lattice points one can use the trigonal system, the hexagonal one or the cubic one.

The trigonal system would be the natural choice because it reflects the symmetry of the crystal best. However, for better comparison with other crystal structures the hexagonal unit cell and unit vectors are more suitable. In order to be able to use both notations a small comparison of the features of both systems has been compiled. Additionally, the different base vectors are drawn in figure 1.5(a). The yellow arrows represent the trigonal base vectors and the black ones the hexagonal base vectors.

For the rhombohedral unit cell[5] the lengths of the base vectors are equal $a_T = b_T = c_T$ and also the angles between the unit vectors $\alpha_T = \beta_T = \gamma_T \neq 90°$. The subscript T indicates the trigonal crystallographic system. The hexagonal basis vectors have the following relations $a_H = b_H \neq c_H$, $\alpha_H = \beta_H = 90°$ and $\gamma_T = 120°$. Therefore the hexagonal unit vectors can be defined in a physical (cartesian) coordinate system.

$$\mathbf{a}_1^H = \mathbf{a}_H = a_H \cdot \begin{pmatrix} \sqrt{3}/2 \\ 1/2 \\ 0 \end{pmatrix}, \quad \mathbf{a}_2^H = \mathbf{b}_H = a_H \cdot \begin{pmatrix} 0 \\ 1 \\ 0 \end{pmatrix}, \quad \mathbf{a}_3^H = \mathbf{c}_H = c_H \cdot \begin{pmatrix} 0 \\ 0 \\ 1 \end{pmatrix} \quad (1.11)$$

The trigonal and hexagonal systems can be related by the following base vector transformations:

$$\mathbf{a}_T = \frac{2}{3}\mathbf{a}_H + \frac{1}{3}\mathbf{b}_H + \frac{1}{3}\mathbf{c}_H \quad (1.12)$$

$$\mathbf{b}_T = -\frac{1}{3}\mathbf{a}_H + \frac{1}{3}\mathbf{b}_H + \frac{1}{3}\mathbf{c}_H \quad (1.13)$$

$$\mathbf{c}_T = -\frac{1}{3}\mathbf{a}_H - \frac{2}{3}\mathbf{b}_H + \frac{1}{3}\mathbf{c}_H \quad (1.14)$$

The retransformation from the trigonal to hexagonal coordinate system is given by:

$$\mathbf{a}_H = \mathbf{b}_T - \mathbf{a}_T; \quad \mathbf{b}_H = \mathbf{b}_T - \mathbf{c}_T; \quad \mathbf{c}_H = \mathbf{a}_T + \mathbf{b}_T + \mathbf{c}_T \quad (1.15)$$

For spherical touching particles, like colloids, the ratio between c and a is constant. Due to the inscription process this is not valid for phase lattices created by the umbrella-like beam configuration. If the inscription is done in a multi-beam setup, the apex-angle θ has a profound influence on the crystal structure.

---

[5]The trigonal crystal system can be explained by the rhombohedral lattice system (cf. [28])

Hexagonal description of the phase lattices

By using the earlier deduced retransformation one can get the hexagonal basis vectors which are then given by:

$$\mathbf{a}_1^H = \frac{\lambda}{3} \cdot \begin{pmatrix} \frac{3}{\sin\theta} \\ -\frac{\sqrt{3}}{\sin\theta} \\ 0 \end{pmatrix} \quad \mathbf{a}_2^H = \frac{\lambda}{3} \cdot \begin{pmatrix} 0 \\ -\frac{2\sqrt{3}}{\sin\theta} \\ 0 \end{pmatrix} \quad \mathbf{a}_3^H = \frac{\lambda}{3} \cdot \begin{pmatrix} 0 \\ 0 \\ \frac{3}{1-\cos\theta} \end{pmatrix} \quad (1.16)$$

It follows that the ratio of in-plane constant to out-of-plane constant is varying as a function of the apex angle and the wavelength.

$$\frac{c}{a} = \frac{\left|\mathbf{a}_3^H\right|}{\left|\mathbf{a}_2^H\right|} = \frac{\sqrt{3}}{2}\frac{\sin\theta}{1-\cos\theta} \quad (1.17)$$

One important fact here is that the polymer usually has a refractive index of $n = 1.5$, so the light undergoes a refraction that alters the apex angle for the non-central beams. This can be simply corrected by using Snell's law. In figure 1.6 the c/a ratio and the in-plane lattice constant a is plotted as a function of the apex angle θ. For angles inside the polymer smaller than $10°$ the ratio increases rapidly, while at larger angles the ratio changes only slowly. An important outcome of this real-space treatment is that for in-plane parameters
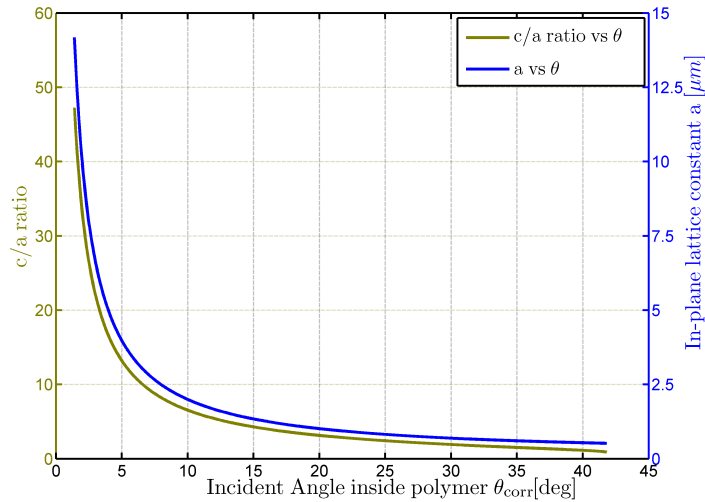
Fig. 1.6.: Ratio of out-of-plane (c) to in-plane (a) lattice constant vs apex angle and relation between in-plane (a) lattice constant and apex angle.

larger than 2μm the out-of-plane lattice constant increases rapidly for an increasing in-plane lattice constant. Since for our purposes bigger lattice constants are desirable there will be some problems because the thickness of the polymer to inscribe is limited to about 300μm

and so the number of possible layers decreases rapidly for an increasing lattice constant. This will eventually lead to a quasi-3D structure.

1.3. Woodpile-structured photonic crystals

Another type of crystals is given by the woodpile-structured photonic crystals (WP PC) [29]. The name has been chosen because the structure looks like one would have stacked a set of rods. In figure 1.7 one can see an SEM image of a woodpile PC. Compared to
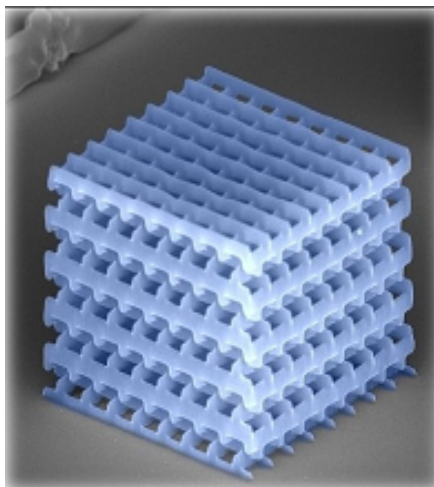
Fig. 1.7.: SEM image of a woodpile-structured photonic crystal.[6]

the holographic approach [30] there are other ways to produce PCs [31]. One group is the 'direct' fabrication of PCs, i.e. direct ink writing [32] or direct laser writing [33], [34] or e.g. the so-called ion-etching technique [35] and another one is the layer by layer e-beam lithography fabrication technique [36]. The latter one can be described as a stacking of 2D structures. All of these techniques have in common that the created structure type is of woodpile structure. The reason for this is that the crystallography of diamond-like PCs favours a photonic bandgap which is a general aim of PC creators. Thus, the technologically simplest diamond-like structure to create is given by the woodpile arrangement.

1.3.1. Fabrication process

In this thesis the technology of direct laser writing was used to create WP PCs. All the WP PCs have been produced in the group of Prof. Wegener at the KIT [7]. The base material of the PC is a polymer like the negative photo resist SU8 [8]. SU-8 is a commonly used

---

[6]source: http://www.cfn.uni-karlsruhe.de/summerschool06
[7]http://www.aph.kit.edu/wegener/
[8]http://www.microchem.com/products/su_eight.htm

epoxy-based negative photo resist which is well-known and applied widely. Recently, other polymer materials have been developed and successfully used [37].

The chemical property of the photo resist can be changed by focussing ultra-short laser pulses into the material. By that the likeliness of multi-photon absorption is strongly increased in the focal volume. That is why a chemical modification of this area occurs which in a subsequent baking process leads to a local polymerization. The non-polymerized part of the photo resist can be removed by chemical agents.

Due to the fact that we use PCs created from more than one photo resist it is necessary to give details about the differences in the fabrication process.

SU-8

For the SU-8 photo resist the photo resist is deposited onto a glass substrate by spin-coating. The glass substrate is fixed at a certain position. Then the laser is used to illuminate the sample at a specific position. With a single-shot exposure the polymerization takes place. By placing the substrate on a piezo-stage, allowing for nanometre-scale movement, one can inscribe nanometre-sized structures with any kind of symmetry. This is only limited by the mechanical stability of the polymer. After the laser inscription is finished the photo resist requires a chemical treatment as well as a bake-out process. The piezo-stage has a limited extension so the macroscopic size of the structure is limited to around 100μm in-plane. As an example an optical microscope image of a typical SU-8 WP crystals is shown in figure 1.8. Characteristic of the SU-8 samples is the circular arrangement and the barrier that is
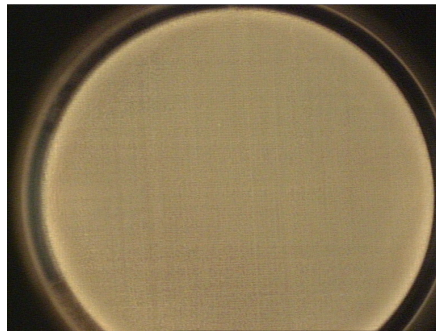

Fig. 1.8.: Optical microscope image of a woodpile-structured photonic crystal made of SU-8. Visible is the circular arrangement and parts of the barrier.

used to stabilize the structure.

IP-44

Aside from the aforementioned SU-8 WP crystals that were the first samples to be used there was a more advanced option available. These WP crystals were made of a new polymer called

IP44. The polymer has a refractive index that is smaller than the one of SU8 in order to match the index to the one of glass ($n_{\text{IP44}} = 1.52$) since the sample is located on a glass substrate. A bake-out is not necessary, only a ten-minute-bath inside a box of isopropyl alcohol. The macroscopic structure also differs a little bit from the SU-8 samples. It has a squared structure and lacks the barrier. In figure 1.9 you can see an optical microscope image of this crystal.
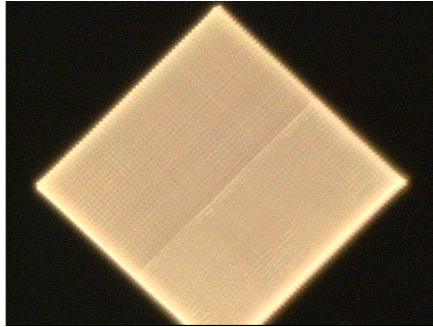
Fig. 1.9.: Optical microscope image of a woodpile-structured photonic crystal made of IP-44. Visible is the rectangular arrangement and parts of the rods that are free-standing and not covered by a barrier.

1.3.2. Crystallography of woodpile-structured PCs

One of the easiest to inscribe structures is the woodpile structure. As the name already indicates this can be thought of as a stacking of rods. In this case long rods are placed at equi-distant positions in the first plane. This first plane can be characterized by the rod spacing a the rod width w and height h as well as its length. The second plane is a set of rods that is placed with a 90° rotation with reference to the first plane. Rod spacing, width, height and length remain unchanged. In the third plane the rods are again rotated by 90° so it has the same orientation as the first one, however there is a translation of half a rod gap a. The fourth plane then is again rotated by 90°. The fifth plane has then again the same in-plane structure as the first one. In figure 1.10 a sketch of a woodpile structure is given.

To describe the crystallographic structure it is necessary to define lattice points and base vectors.

Again like in the previous section one can define the basis vectors of one coordinate system with the help of a cartesian one. The cartesian coordinate system is in this case defined in such a way that the x-axis is parallel to the direction of one set of logs, and the y-axis points in the direction of the logs perpendicular to the first set. The z-axis is therefore the direction of stacking. With this definition it is possible to define a set of base vectors. In literature (e.g. [38]) the cubic system is mostly used, although this is not the primitive unit
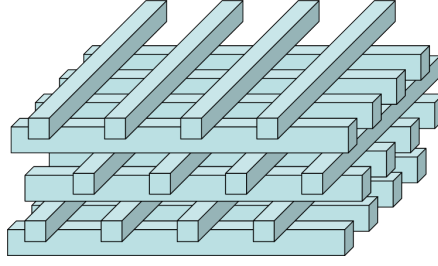
Fig. 1.10.: Sketch of a woodpile structure. Clearly visible the offset between second next layers of half a rod spacing.

cell. The Woodpile structure in our case is constructed in such a way that the aspect ratio is $c/a = \sqrt{2}$. This means that the resulting structure has a face-centred cubic (fcc) symmetry. Small deviations of this c/a-ratio cause a symmetry reduction to a face-centred tetragonal (fct) symmetry.

One can define the fcc base vectors as follows:

$$\mathbf{a}_{\text{Cub}} = a_{\text{Cub}} \cdot \begin{pmatrix} 1 \\ 1 \\ 0 \end{pmatrix}, \quad \mathbf{b}_{\text{Cub}} = a_{\text{Cub}} \cdot \begin{pmatrix} -1 \\ 1 \\ 0 \end{pmatrix}, \quad \mathbf{c}_{\text{Cub}} = c_{\text{Cub}} \cdot \begin{pmatrix} 0 \\ 0 \\ 1 \end{pmatrix} \tag{1.18}$$

Since the Bravais lattice is not unique (similar to the phase lattices), it is possible to define another set of base vectors. They have a body-centred tetragonal (bct) unit cell. For these vectors the unit cell is primitive. They are given by:

$$\mathbf{a}_{\text{Tetr}} = a_{\text{Tetr}} \cdot \begin{pmatrix} 1 \\ 0 \\ 0 \end{pmatrix}, \quad \mathbf{b}_{\text{Tetr}} = a_{\text{Tetr}} \cdot \begin{pmatrix} 0 \\ 1 \\ 0 \end{pmatrix}, \quad \mathbf{c}_{\text{Tetr}} = c_{\text{Tetr}} \cdot \begin{pmatrix} 0 \\ 0 \\ 1 \end{pmatrix} \tag{1.19}$$

Where in both cases the lattice constants are the same $a_{\text{Tetr}} = a_{\text{Cub}}$ and $c_{\text{Tetr}} = c_{\text{Cub}}$. The unit cell of the fcc system V_{Cub} is larger than the one of the bct V_{Tetr} system. Both values can be calculated to:

$$V_{\text{Cub}} = \mathbf{a}_{\text{Cub}} \cdot \mathbf{b}_{\text{Cub}} \times \mathbf{c}_{\text{Cub}} = 2a^2c = 2\sqrt{2}a^3 \tag{1.20}$$

$$V_{\text{Tetr}} = \mathbf{a}_{\text{Tetr}} \cdot \mathbf{b}_{\text{Tetr}} \times \mathbf{c}_{\text{Tetr}} = a^2c = \sqrt{2}a^3 \tag{1.21}$$

In order to demonstrate the differences of the tetragonal and the cubic system, the unit cells are depicted in figure 1.11.

(a) Tetragonal arrangement.   (b) Cubic arrangement.
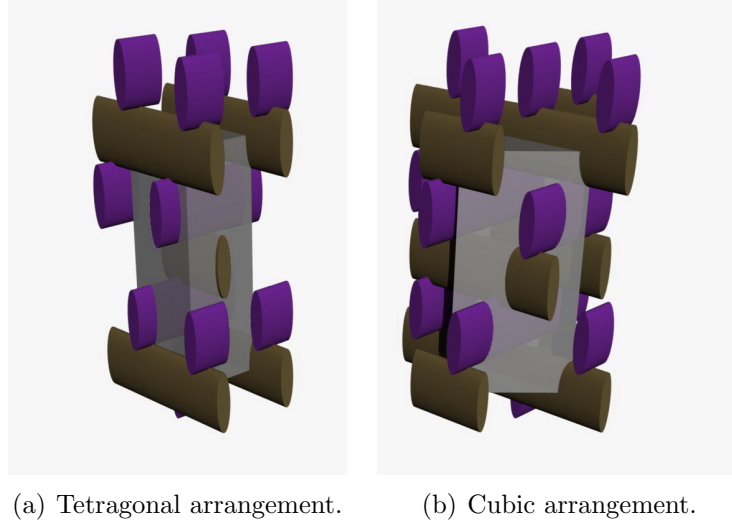
Fig. 1.11.: Depiction of two different unit cells of the same woodpile structure. The unit-cell itself is depicted as the grey-shaded rectangular box. The WP rods have been partially depicted. Two different rod colours have been used to emphasize the different layers.

The transformation from fcc to bct is given by the following equations:

$$\mathbf{a}_{\text{Tetr}} = \frac{1}{2}\left(\mathbf{a}_{\text{Cub}} - \mathbf{b}_{\text{Cub}}\right), \quad \mathbf{b}_{\text{Tetr}} = \frac{1}{2}\left(\mathbf{a}_{\text{Cub}} + \mathbf{b}_{\text{Cub}}\right), \quad \mathbf{c}_{\text{Tetr}} = \mathbf{c}_{\text{Cub}} \tag{1.22}$$

And the retransformation is given by:

$$\mathbf{a}_{\text{Cub}} = \mathbf{a}_{\text{Tetr}} + \mathbf{b}_{\text{Tetr}}, \quad \mathbf{b}_{\text{Cub}} = -\mathbf{a}_{\text{Tetr}} + \mathbf{b}_{\text{Tetr}}, \quad \mathbf{c}_{\text{Cub}} = \mathbf{c}_{\text{Tetr}} \tag{1.23}$$

The reciprocal lattice vectors in the bct system are given by:

$$\mathbf{a}^*_{\text{Tetr}} = \frac{2\pi}{a} \cdot \begin{pmatrix} 1 \\ 0 \\ 0 \end{pmatrix}, \quad \mathbf{b}^*_{\text{Tetr}} = \frac{2\pi}{a} \cdot \begin{pmatrix} 0 \\ 1 \\ 0 \end{pmatrix}, \quad \mathbf{c}^*_{\text{Tetr}} = \frac{2\pi}{c} \cdot \begin{pmatrix} 0 \\ 0 \\ 1 \end{pmatrix} \tag{1.24}$$

Furthermore, the reciprocal lattice vectors in the fcc system are given by:

$$\mathbf{a}^*_{\text{Cub}} = \frac{\pi}{a} \cdot \begin{pmatrix} 1 \\ 1 \\ 0 \end{pmatrix}, \quad \mathbf{b}^*_{\text{Cub}} = \frac{\pi}{a} \cdot \begin{pmatrix} -1 \\ 1 \\ 0 \end{pmatrix}, \quad \mathbf{c}^*_{\text{Cub}} = \frac{2\pi}{c} \cdot \begin{pmatrix} 0 \\ 0 \\ 1 \end{pmatrix} \tag{1.25}$$

The tetragonal system is used throughout this work. This is because the focus lies here on the investigation of the far-field diffraction pattern. For this investigation an important point is that due to the bigger unit cell several reflections in the cubic system would not

occur in the diffraction pattern. Moreover, the Miller indices for the tetragonal system depict the symmetry of the diffraction pattern very well.

2. Electromagnetic Waves in Periodic Media

In this chapter the interaction of electromagnetic waves with periodic media is discussed. In section 2.1 Maxwell's equations are decoupled and simplified for the case of infinitely large photonic crystals. Furthermore, solution methods for the resulting master equations are discussed. This section is mostly following [39] and [40]. In 2.2 influences on the light interaction stemming from the finite size of the photonic crystal are addressed which is on the basis of [40] and [41]. In the last section 2.3 approximations to the solutions of Maxwell's equations in photonic crystals are introduced.

2.1. Electrodynamics for infinitely large three-dimensional photonic crystals

Maxwell's equations are a set of partial differential equations that describe the interaction of light with media. They are given in (2.1).

$$
\begin{aligned}
\nabla \cdot \mathbf{D}(\mathbf{r}, t) &= \rho(\mathbf{r}, t) \\
\nabla \times \mathbf{E}(\mathbf{r}, t) &= -\frac{\partial}{\partial t} \mathbf{B}(\mathbf{r}, t) \\
\nabla \cdot \mathbf{B}(\mathbf{r}, t) &= 0 \\
\nabla \times \mathbf{H}(\mathbf{r}, t) &= \mathbf{j}(\mathbf{r}, t) + \frac{\partial}{\partial t} \mathbf{D}(\mathbf{r}, t)
\end{aligned}
\tag{2.1}
$$

In this case $\mathbf{E}$ is the electric field, $\mathbf{B}$ the magnetic induction, $\mathbf{D}$ the electric displacement field and $\mathbf{H}$ is called the magnetic field. ρ stands for the free charge density and $\mathbf{j}$ for the current density. For the problem at hand no free charges ($\rho = 0$) and electric currents ($\mathbf{j} = 0$) need to be considered so that Maxwell's equations can be simplified to

$$\nabla \cdot \mathbf{D}(\mathbf{r}, t) = 0$$
$$\nabla \times \mathbf{E}(\mathbf{r}, t) = -\frac{\partial}{\partial t} \mathbf{B}(\mathbf{r}, t)$$
$$\nabla \cdot \mathbf{B}(\mathbf{r}, t) = 0 \tag{2.2}$$
$$\nabla \times \mathbf{H}(\mathbf{r}, t) = \frac{\partial}{\partial t} \mathbf{D}(\mathbf{r}, t)$$

For homogeneous, linear media the following relations (2.3) between the electric field and the electric displacement field as well as between the magnetic field and the magnetic induction can be used.

$$\mathbf{D}(\mathbf{r}, t) = \epsilon_o \epsilon(\mathbf{r}) \mathbf{E}(\mathbf{r}, t)$$
$$\mathbf{B}(\mathbf{r}, t) = \mu_o \mu(\mathbf{r}) \mathbf{H}(\mathbf{r}, t) \tag{2.3}$$

For linear, isotropic and homogeneous materials the fields $\mathbf{D}$ and $\mathbf{B}$ can be eliminated by using (2.3). Then it is possible to decouple the remaining equations with fields $\mathbf{H}$ and $\mathbf{E}$. This is done by employing $\nabla \times$ on the second and fourth equation in (2.2). After interchanging time and space differentiation on the right hand side this yields the following equations:

$$\nabla \times \left[\frac{1}{\mu(\mathbf{r})} \nabla \times \mathbf{E}(\mathbf{r}, t) \right] = -\frac{\partial}{\partial t} \nabla \times \mu_o \mathbf{H}(\mathbf{r}, t)$$
$$\nabla \times \left[\frac{1}{\epsilon(\mathbf{r})} \nabla \times \mathbf{H}(\mathbf{r}, t) \right] = \frac{\partial}{\partial t} \nabla \times \epsilon_o \mathbf{E}(\mathbf{r}, t) \tag{2.4}$$

After substituting the right hand side in (2.4) with the fourth and second one from (2.2) the decoupled equations are then given by (2.5).

$$\frac{1}{\epsilon(\mathbf{r})} \nabla \times \left[\frac{1}{\mu(\mathbf{r})} \nabla \times \mathbf{E}(\mathbf{r}, t) \right] = -\frac{1}{c^2} \frac{\partial^2}{\partial t^2} \mathbf{E}(\mathbf{r}, t)$$
$$\frac{1}{\mu(\mathbf{r})} \nabla \times \left[\frac{1}{\epsilon(\mathbf{r})} \nabla \times \mathbf{H}(\mathbf{r}, t) \right] = -\frac{1}{c^2} \frac{\partial^2}{\partial t^2} \mathbf{H}(\mathbf{r}, t) \tag{2.5}$$

The relation $c = 1/\sqrt{\mu_o \epsilon_o}$ has been used. For all the considered materials the magnetic susceptibility χ is vanishing which implies $\mu(\mathbf{r}) = 1$. In addition to that a possible frequency dependence of the dielectic function is not considered. Neglecting inelastic scattering, the time dependence of the fields can be expressed by the eigen-angular frequency ω and the time-dependent parts of the fields can be decoupled and rewritten as $\mathbf{E}(\mathbf{r}, t) = \mathbf{E}(\mathbf{r}) \cdot e^{i\omega \cdot t}$ and respectively $\mathbf{H}(\mathbf{r}, t) = \mathbf{H}(\mathbf{r}) \cdot e^{i\omega \cdot t}$. So the wave equations are given by

$$\frac{1}{\epsilon(\mathbf{r})} \, \nabla \times \left[\nabla \times \mathbf{E}(\mathbf{r})\right] = \frac{\omega^2}{c^2} \cdot \mathbf{E}(\mathbf{r})$$

$$\nabla \times \left[\frac{1}{\epsilon(\mathbf{r})} \, \nabla \times \mathbf{H}(\mathbf{r})\right] = \frac{\omega^2}{c^2} \cdot \mathbf{H}(\mathbf{r})$$

(2.6)

It is sufficient to consider only one equation in (2.6) because by knowing one field the other one can be calculated by the corresponding relation from Maxwell's equations. In literature [18] mostly the **H**-field is considered because the differential operator $\nabla \times \frac{1}{\epsilon(\mathbf{r})} \nabla \times$ is Hermitian.

Another possibility of solving the first equation in (2.6) is to use the relation $\mathrm{rot}\,\mathrm{rot} = -\nabla^2 + \mathrm{grad}\,\mathrm{div}$. This yields

$$-\nabla^2 \mathbf{E}(\mathbf{r}) + \nabla \cdot \left[\nabla \mathbf{E}(\mathbf{r})\right] = \epsilon(\mathbf{r}) \frac{\omega^2}{c^2} \cdot \mathbf{E}(\mathbf{r}) \tag{2.7}$$

This can be further simplified by considering the first equation in (2.3). Thus, the following relations can be deduced:

$$0 = \nabla \mathbf{D} = \nabla \epsilon \epsilon_o \mathbf{E} = \epsilon_o \epsilon \nabla \mathbf{E} + \epsilon_o \mathbf{E} \nabla \epsilon \tag{2.8}$$

$$\rightarrow \nabla \mathbf{E} = -\mathbf{E} \, \frac{\nabla \epsilon}{\epsilon} \tag{2.9}$$

$$\rightarrow \nabla \mathbf{E} = -\mathbf{E} \, \nabla \ln \epsilon \tag{2.10}$$

$$\rightarrow \nabla \cdot \left[\nabla \mathbf{E}(\mathbf{r})\right] = -\nabla \, (\mathbf{E} \, \nabla \ln \epsilon) \tag{2.11}$$

The last equation can be used to simplify (2.7) which yields

$$-\nabla^2 \mathbf{E}(\mathbf{r}) - \nabla \, (\mathbf{E} \, \nabla \ln \epsilon) = \epsilon(\mathbf{r}) \frac{\omega^2}{c^2} \cdot \mathbf{E}(\mathbf{r}) \tag{2.12}$$

If the term $\left[\nabla \mathbf{E}(\mathbf{r})\right]$ vanishes, the resulting equation is given by:

$$\nabla^2 \mathbf{E} + \frac{\omega^2}{c^2} \cdot \epsilon(\mathbf{r}) \mathbf{E} = 0 \tag{2.13}$$

$$\rightarrow \left(\nabla^2 + k^2 \epsilon(\mathbf{r})\right) \mathbf{E}(\mathbf{r}) = 0 \tag{2.14}$$

The equation above can be solved for each component of the electric field separately and is well-known from optics and electrodynamics [42]. The validity of the assumption $\nabla \ln \epsilon \to 0$ determines the equation that has to be solved for the scattering problem. Thus, the validity depends on the properties of the dielectric function. In the following multiple cases will be discussed. Firstly, for homogeneous media ($\epsilon(\mathbf{r}) = \text{const}$) the assumption $\nabla \ln \epsilon \to 0$ is valid and the equation to solve even reduces to the well-known Helmholtz equation. Secondly, the dielectric function has a slow variation with position that it is effectively constant over distances of the order of the wavelength. Thirdly, the dielectric function varies with position in the order of the wavelength but the variation in the amplitude of the dielectric function is very small ($\epsilon(\mathbf{r}) = \epsilon(\text{const}) + \Delta\epsilon(\mathbf{r})$ with $\Delta\epsilon(\mathbf{r}) << \epsilon(\text{const})$). For the second and third case the simplified equation (2.14) can also be solved. For the fourth and last case the dielectric function is assumed to change in position in the order of the wavelength and the amplitude of the dielectric function should change considerably. This case does not allow the simplification $\nabla \ln \epsilon \to 0$. Therefore, the equations (2.6) have to be solved. For photonic crystals with a high dielectric contrast the fourth and last case have to be used. If the contrast becomes smaller the remaining question is in which regime a simplification of (2.6) is valid.

2.1.1. Plane-wave expansion method

Other techniques than discussing the limit of $\nabla \epsilon \to 0$ involve a numerical solution of (2.6) where the periodicity of the photonic crystals can be exploited. Since PCs are periodic media defined by the dielectic constant $\epsilon(\mathbf{r})$ it holds that $\epsilon(\mathbf{r}) = \epsilon(\mathbf{r} + \mathbf{T})$ where $\mathbf{T} = u\mathbf{a} + v\mathbf{b} + w\mathbf{c}$ is a translation vector that is composed of a linear combination of the lattice base vectors $\mathbf{a}, \mathbf{b}, \mathbf{c}$ of the PC. Therefore, it is possible to express the dielectric function in terms of a series of Fourier coefficients. With respect to (2.6) one chooses the inverse dielectric function to be developed in such a way.

$$\frac{1}{\epsilon(\mathbf{r})} = \sum_{\mathbf{G}} \kappa(\mathbf{G}) \cdot e^{i\,\mathbf{G}\cdot\mathbf{r}} \tag{2.15}$$

The second important step is to use the so-called Bloch theorem not only for the dielectric function but also for the electromagnetic fields in a similar way as it is used for electronic waves inside ordinary crystals with a periodic potential. So one can rewrite the fields with vector functions $\mathbf{u}_{\mathbf{k}n}$ and $\mathbf{v}_{\mathbf{k}n}$ that make use of the lattice periodicity.

$$\mathbf{E}(\mathbf{r}) = \mathbf{E}_{\mathbf{k}n}(\mathbf{r}) = \mathbf{u}_{\mathbf{k}n}(\mathbf{r}) \cdot e^{i\,\mathbf{k}\cdot r}$$

$$\mathbf{H}(\mathbf{r}) = \mathbf{H}_{\mathbf{k}n}(\mathbf{r}) = \mathbf{v}_{\mathbf{k}n}(\mathbf{r}) \cdot e^{i\,\mathbf{k}\cdot r}$$

(2.16)

The proof of the Bloch theorem can be found in [40]. The wave fields have been indexed by a wave vector $\mathbf{k}$ and a band number n. The resulting Fourier expansions take the following form:

$$\frac{1}{\epsilon(\mathbf{r})} = \sum_{\mathbf{G}} \kappa(\mathbf{G}) \cdot e^{i\,\mathbf{G}\cdot\mathbf{r}}$$

$$\mathbf{E}_{\mathbf{k}n}(\mathbf{r}) = \sum_{\mathbf{G}} \tilde{\mathbf{E}}_{\mathbf{k}n}(\mathbf{G}) \cdot e^{i\,(\mathbf{k}+\mathbf{G})\cdot\mathbf{r}}$$

$$\mathbf{H}_{\mathbf{k}n}(\mathbf{r}) = \sum_{\mathbf{G}} \tilde{\mathbf{H}}_{\mathbf{k}n}(\mathbf{G}) \cdot e^{i\,(\mathbf{k}+\mathbf{G})\cdot\mathbf{r}}$$

(2.17)

Inserting (2.17) into (2.6) the latter set of equations reduce to the following eigenvalue equations for the Fourier components $\tilde{\mathbf{E}}_{\mathbf{k}n}(\mathbf{G})$ and $\tilde{\mathbf{H}}_{\mathbf{k}n}(\mathbf{G})$ as well as for the eigenfrequencies $\omega_{\mathbf{k}n}$.

$$-\sum_{\mathbf{G}'} \kappa(\mathbf{G} - \mathbf{G}') \cdot (\mathbf{k} + \mathbf{G}') \times \left[(\mathbf{k} + \mathbf{G}') \times \tilde{\mathbf{E}}_{\mathbf{k}n}(\mathbf{G}') \right] = \frac{\omega_{\mathbf{k}n}^2}{c^2} \tilde{\mathbf{E}}_{\mathbf{k}n}(\mathbf{G})$$

$$-\sum_{\mathbf{G}'} \kappa(\mathbf{G} - \mathbf{G}') \cdot (\mathbf{k} + \mathbf{G}) \times \left[(\mathbf{k} + \mathbf{G}') \times \tilde{\mathbf{H}}_{\mathbf{k}n}(\mathbf{G}') \right] = \frac{\omega_{\mathbf{k}n}^2}{c^2} \tilde{\mathbf{H}}_{\mathbf{k}n}(\mathbf{G})$$

(2.18)

The original differential equations have now been transformed to a set of algebraic equations. As a solution one has to find the eigenfrequencies $\omega_{\mathbf{k}n}$ and eigenmodes $\tilde{\mathbf{H}}_{\mathbf{k}n}(\mathbf{G})$, $\tilde{\mathbf{E}}_{\mathbf{k}n}(\mathbf{G})$. The left-hand sides for both fields in (2.18) are infinite-sized matrices. Thus, the eigenvalues and eigenvectors can be found by a matrix diagonalization.

This has to be done numerically, whereas the infinite number of reciprocal lattice vectors $\mathbf{G}'$ has to be cut off at a certain number N. The accuracy is proportional to the number of reciprocal lattice vectors that are taken into account.

Important to notice is that the solution should be obtained for each possible vector $\mathbf{k}_n$. This means that for each possible vector one has to solve the eigenvalue equation.

It is sufficient to solve one of the two equations of (2.18). The other one is given by the fact that the electric field is perpendicular to the magnetic one. Generally speaking, the computation time necessary for the solution is quite high $\mathcal{O}(N^3)$. According to [40] it is

preferable to solve the H-field due to the fact that the degree of freedom for this matrix transformation ($f = 2$) is one less than for the E-field ($f = 3$).

On account of the high computational demand the number of reciprocal lattice vectors has to be limited which has a negative effect on the accuracy of the solution. Authors have also shown (cf. [43]) that the convergence of the algorithm is deteriorating for a higher variation of the refractive index contrast.

As a result the obtained solutions ω_n can be depicted in a graphical representation which is known as the band structure of photonic crystals.

Band structure of photonic crystals

The band structure is defined as the variation of the eigen-angular frequencies $\omega(\mathbf{k})$ vs. the wave propagation vectors $\mathbf{k}$, so it is another term for the dispersion relation. Due to the periodicity of the crystal the eigenfrequencies also inherit a periodical modulation $\omega_n(\mathbf{k}) = \omega_n(\mathbf{k} + \mathbf{G})$. So it is possible to limit the depiction of the band structure to the first Brillouin zone. This zone can be thought of as a primitive cell of the reciprocal lattice (Wigner-Seitz cell). The reason why this is possible is due to the fact that all Bloch waves can be characterized in one Brillouin zone. The rest of the fields can be obtained by symmetry operations.

A more detailed look at the composition of the band structure is necessary for the further understanding. As already mentioned there is a set of eigenfrequencies $\omega_n(\mathbf{k})$ for each $\mathbf{k}$ vector. The solutions are numbered by n. This depends on how many reciprocal lattice vectors have been accounted for in the numerics. Usually the numbering is from the lowest frequency ascending to the highest one. The index n is also called band number.

All solutions that have a common counting index n are called the n-th photonic band. This means that the lowest eigenfrequency obtained for each $\mathbf{k}$ within the first Brillouin zone is called the first band. A more general term would be the dispersion surface which is defined in k-space as the places where the dispersion function ω is constant. For periodic media this is reduced to the band structure. For 3D photonic crystals it is possible but impractical to visualize a dispersion surface in a graphical representation (k_x, k_y, k_z) because one has a surface for a single frequency and the point of interest is the change of the surface for different frequencies. This is why one uses the so-called *band diagrams*. In the band diagram one can plot bands for different frequencies. The peculiarity about this diagram is that the bands are given for specific $\mathbf{k}$ vectors. These vectors in k-space are given by the connecting lines of the boundary points of the irreducible Brillouin zone. The irreducible BZ is a reduction of the first BZ by all of the symmetries in the point group of the lattice.

Besides it can be shown that the maximum change in the dispersion relation will occur at

the borders of the irreducible BZ which is the basic reason for the use of the band diagrams.

Calculating a band structure for 3D photonic crystal

One important feature of the band structure is that there are regions of the frequency where no k-vector has access to. This is called a photonic bandgap which is the photonic counterpart of an electronic bandgap. Since most of the research focusses on finding a photonic bandgap, there are numerous tools to calculate such a bandgap. In this case the programme *Bandsolve*[9] can be used.

In order to have a deeper understanding of the light interaction inside the crystal one can take a look at the band diagram for woodpile photonic crystals. The general aim of photonics is to find a bandgap for a wavelength in the telecommunications range of approximately $\lambda = 1.5\mu$m. With a lattice constant of $a = 0.9\mu$m the a/λ-ratio differs a lot from the one used in the investigation of this thesis. Here, the wavelength is in the range of visible light which means a larger a/λ-ratio. In the following band diagrams, the normalized frequencies are given in values of a/λ. One can see that for a large ratio the number of Fourier components increase rapidly. This can be adjusted by tuning the refractive index contrast. So the essential part here is to observe the changes in the band structure and connect it to the diffraction in the far-field.

As you can see in figure 2.1(a) and figure 2.1(b) the influence of the refractive index on the band structure is considerable. As expected, the band structure for crystals with low dielectric contrast resembles the one of a homogeneous material. For each dielectric contrast 200 bands have been calculated. Comparing both of the calculated band structures two basic differences are observable. First the change from low contrast to high contrast results in a compression of the bands. This means that the mode density increases. Furthermore, a splitting of the bands is visible.

2.1.2. Alternative solution methods

In this part other techniques for solving Maxwell's equations inside photonic crystals will be shortly discussed.

FDTD

The previous ideas for solving Maxwell's equations are based on a transformation of the equations into k-space or in other words into the frequency domain. Another approach is the so-called finite-difference time domain (FDTD) method [45]. Here, Maxwell's equations

---

[9]http://www.rsoftdesign.com/
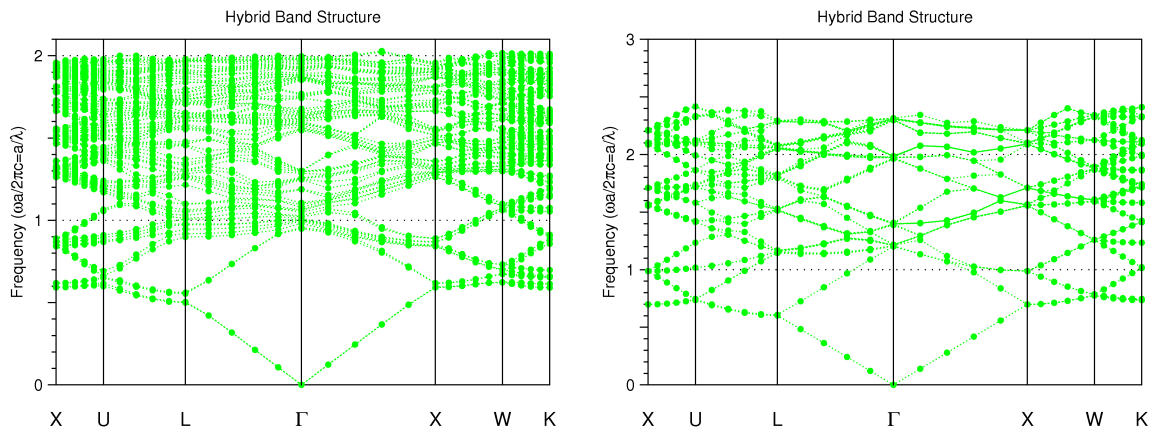
(a) Band structure of a high contrast photonic crystal $\Delta n = 0.6$

(b) Band structure of a low contrast crystal $\Delta n = 0.005$
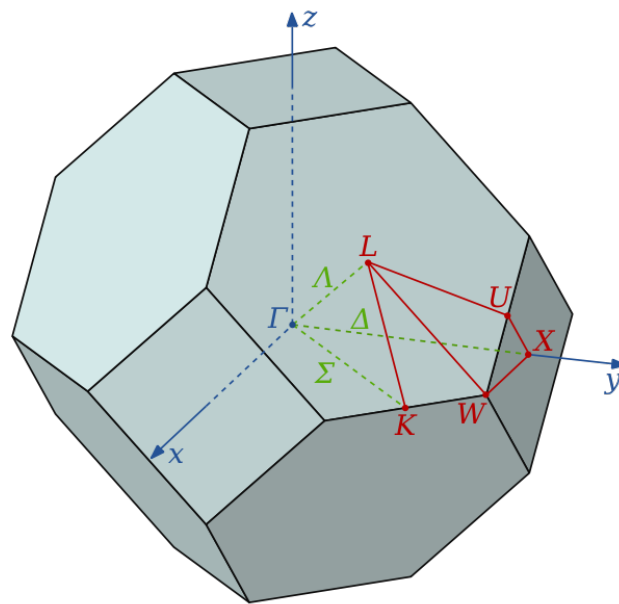
(c) First Brillouin zone of the woodpile-structured photonic crystal. The crystallographic symbols $\Gamma L U X W K$ indicate the irreducible Brillouin zone [44].

Fig. 2.1.: Shown are band structure calculations for woodpile-structured photonic crystals with low and high dielectric contrast. In addition the first Brillouin zone is plotted to identify the directions along which the dispersion relation is calculated.

are discretized in time and space into a finite difference form. The solutions are obtained by directly integrating Maxwell's equations in discretized points in space and time. Therefore, the photonic crystal is subdivided into a regular grid structure and the equations are solved separately in each grid point. The computational grid should be chosen smaller than the wavelengths under consideration. In the photonic crystal community the FDTD method is one of the most widely used techniques. This is because there are advantages compared to the frequency-domain methods. First of all the computational time is linearly connected to the size of the photonic crystal. Another advantage is the possibility to implement irregular structures like defects. The incident field is also not limited to monochromatic or continuous waves. However, in the problem at hand the structures are supposed to be perfectly periodic and the incoming waves are continuous, so these advantages of the FDTD method are not applicable. This is why in this work frequency domain methods are used.

FEM

Another way of solving Maxwell's equations is the method of finite elements (FEM). FEM is a numerical tool that is used to solve partial differential equations approximately. Therefore, it can also be used for solving Maxwell's equations. In order to find a solution the crystal is subdivided into a mesh which has to have a typical size that scales with $\lambda/10$ for numerical stability. Then an incident wave-field has to be parameterized, usually a monochromatic plane wave is assumed. Maxwell's equations are then approximately solved in each of the mesh elements. In this case there are different solution techniques (eigensolver) available and the one that best fits the problem has to be picked. Compared to other methods the FEM has the big advantage of an easy implementation. Complicated structures can also be modelled easily. The last point is not valid for periodic media like PCs since the structure at hand is rather simple.

2.2. Electrodynamic light interaction with 3D photonic crystals of finite size

In order to calculate the diffraction pattern and scattering curves one has to take into account the finite size of the crystal. The finite size implicates boundary conditions at the interface between the crystal and its ambience. One way of dealing with these boundary conditions is shown in [41]. First of all one has to consider a photon in free space with wave vector

$\mathbf{k} = (k_x, k_y, k_z)$. Naturally, the dispersion relation is given by:

$$\omega = c \cdot \sqrt{k_x^2 + k_y^2 + k_z^2} \tag{2.19}$$

For the photonic crystal considered in this thesis the finite size is related to one dimension (z) while in the other two dimensions (x, y) the crystal has a much higher expansion. Inside a photonic crystal that is considered to be finite in z-direction the modes are depending on the lateral wave vector $\mathbf{k}_\| \equiv (k_x, k_y)$ [41]. Due to the fact that $k_z^2 > 0$ the photons of lateral wave vector $\mathbf{k}_\|$ can fulfill the inequality $\omega > c \cdot \sqrt{k_x^2 + k_y^2}$. So one can couple an incident photon into the photonic crystal. This kind of mode is called leaky mode because of its finite lifetime due to the energy it leaks. The other possibility is the condition $k_z^2 < 0$. For this condition it means that one has to couple an evanescent wave into the crystal and the resulting modes cannot exit the crystal and are thus confined to it. The region of leaky modes and the one of non-leaky ones are separated by the boundary condition $\omega = c \cdot \sqrt{k_x^2 + k_y^2}$. The just described additional modes lead to a splitting of the band structure. It can be shown that the quantization is given by the following condition:

$$\omega_p = \frac{c}{\sqrt{\epsilon}} \cdot \sqrt{\mathbf{k}_\|^2 + \left(p\frac{\pi}{L}\right)^2} \tag{2.20}$$

L denotes here the finite size of the crystal and p is an integer quantization. The splitting of the photonic bands is in the framework of these PCs not the decisive part. This is because for all the PCs considered the density of the possible modes is rather large.

2.2.1. Refraction at photonic crystals

Except for the splitting of the photonic bands, there is a more pronounced feature to be considered for the finite PCs and this is the refraction at the interfaces. First a short reminder of the law of refraction for homogeneous materials is given. Then the refraction at photonic crystals is considered.

Homogeneous medium

A beam travelling in a homogeneous medium n_{ext} is incident on a medium with homogeneous refractive index n_{hom} under an incident angle θ_1 (cf. figure 2.2(a)). The angle of the reflected beam is equal to the incident one $\theta_{\text{ext}} = \theta_{\text{ext}}^{\text{refl}}$. Due to the translational symmetry the parallel component of the wave vector should be conserved in case of reflection or refraction $\mathbf{k}_{\text{ext},\|} = \mathbf{k}_{\text{int},\|}$. The absolute value of the wave vector is given by $|\mathbf{k}_{\text{ext}}| = \frac{n_{\text{ext}}\omega}{c}$. Assuming the external medium is air $n_{\text{ext}} = 1$, then the parallel wave vector conservation gives the

(a) Homogeneous material.
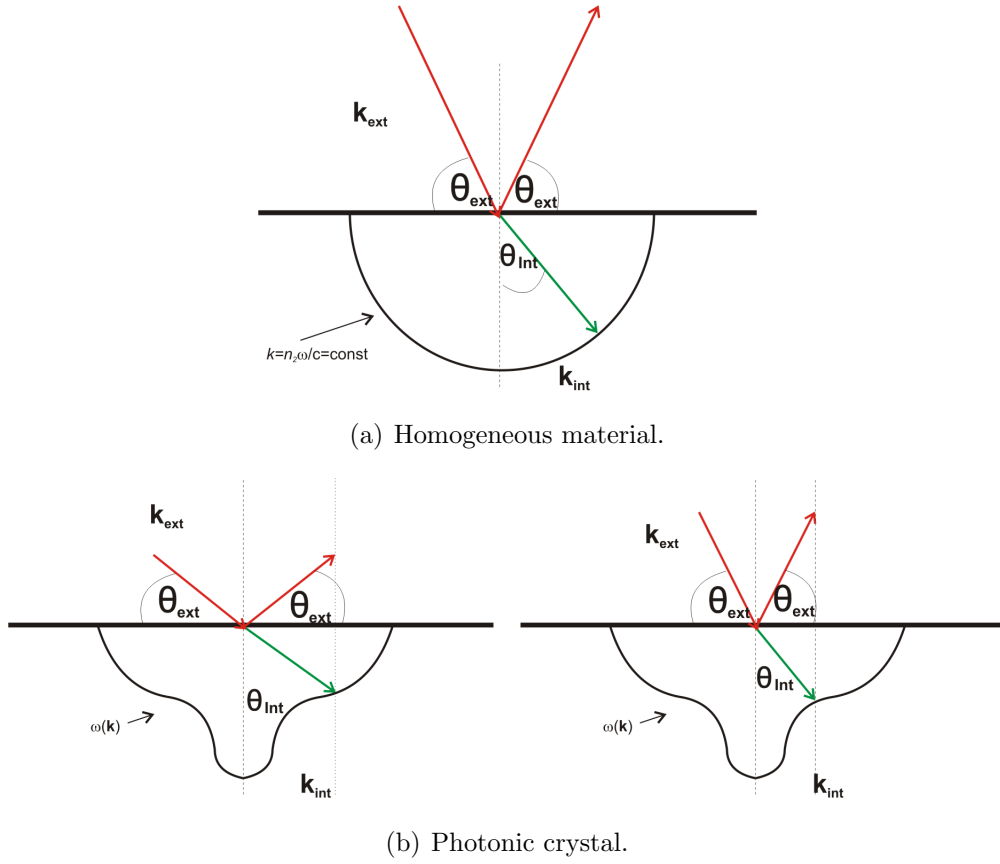
(b) Photonic crystal.

Fig. 2.2.: Refraction law for a homogeneous material and a photonic crystal

following equation:

$$\frac{\omega}{c} \sin\left(\theta_{\text{ext}}\right) = \frac{n_{\text{hom}}\omega}{c} \cdot \sin\left(\theta_{\text{int}}\right) \tag{2.21}$$

This directly leads to the description of refraction by Snell's law:

$$\sin\left(\theta_{\text{ext}}\right) = n_{\text{hom}} \cdot \sin\left(\theta_{\text{int}}\right) \tag{2.22}$$

In figure 2.2(a) the refraction for homogeneous material is sketched (2D case). The semi-circle (in 3D: semi-sphere) indicates the equi-frequency line (surface) for $k(\omega)$. Since ω is constant for homogeneous material the equi-frequency lines are just given by a circle with radius $|\mathbf{k}_{\text{int}}| = n_{\text{hom}}\omega/c = \text{const}$.

Photonic crystal

For a PC the frequency is not constant but wave vector dependent $\omega(\mathbf{k})$. The equi-frequency lines differ then from the semi-circle. This is depicted in figure 2.2(b). The end point of the

wave vector lies on the equi-frequency surface which is determined by the band structure $\omega(\mathbf{k})$. Comparable to the homogeneous case the parallel component of the wave vector has to be conserved $\mathbf{k}_{\text{int}\parallel} = \mathbf{k}_{\text{ext}\parallel}$. This follows from the previous discussion of the electromagnetic waves inside the PC which concluded that the waves inside the crystal are given by Bloch waves. In this case due to the finite size the Bloch theorem is only valid in the direction parallel to the surface of the crystal because the periodicity of the crystal perpendicular to the surface is broken. This means that the electric field can be decomposed as a Fourier series with components parallel to the surface:

$$\mathbf{E}(\mathbf{r}_\parallel) \propto \sum_{\mathbf{G}_\parallel} \tilde{\mathbf{E}}(\mathbf{G}_\parallel) \exp(i(\mathbf{G}_\parallel + \mathbf{k}_{\text{ext}\parallel})\mathbf{r}_\parallel) \tag{2.23}$$

The subscript $\parallel$ indicates vectors that are parallel to the crystal surface in real space and the subscript $\perp$ indicates the perpendicular ones while actually the reciprocal vector $\mathbf{G}_\parallel = h\mathbf{a}^* + k\mathbf{b}^*$ is perpendicular to the surface in real space. The components $\tilde{\mathbf{E}}(\mathbf{G}_\parallel)$ are the coupled Fourier expansion coefficients of the wave propagating through the crystal.

The importance of this discussion for the problem at hand will become clear in section 3.1 where the scattering geometry is discussed. Here, the problem of the equi-frequency curve $\omega(k)$ can be transformed into a refractive index that is depending on the incident angle of the beam $\mathbf{k}_{\text{ext}}$. It means that the relation $|\mathbf{k}| = n\omega(\mathbf{k})/c = 2\pi/\lambda \cdot n(\mathbf{k})$ implies in practice a refractive index that is angle-dependent.

For the PC considered in this thesis the angle-dependent refractive index has to be taken into account for considering the experimental scattering problem. It can be basically decomposed into two cases. The first case is the one of a low RI contrast PC. In this case the band structure does not differ much to the one of an 'empty lattice' so the equi-frequency surface will not differ much from a spherical shape. An approximation of the effective refractive index n_{eff} can be made. This approximation will have a direction-independent form. For the second case such kind of approximation is rather inaccurate. To get a theoretical description of the refractive index as a function of the incident beam direction would be desirable but is not accomplishable due to the fact that for the parameters under investigation the mode density is too high ($\omega \cong a/\lambda \approx 1.4$)

2.2.2. Rigorous coupled-wave theory

In order to predict scattering curves it is convenient to simulate the diffraction. The earlier introduced plane-wave expansion method (PWE) is a good method to obtain the eigenmodes of an infinite PC. However, it is limited to the modal depiction of the eigenproblem. This solution in the frequency-domain is based on an expansion of the fields as definite-frequency

states of a complete basis which is truncated at some point [46]. The limitations have already been discussed in section 2.1.1. There are more numerical tools available. Some of them are completely equivalent approaches that have been used by different communities and have been named differently.

One of the theories is based on the rigorous coupled-wave analysis (cf. [47]), the other one is referred to as the Fourier modal method. In the 'photonics community' the equivalent terms transfer matrix method and scattering matrix technique (sometimes eigenmode expansion method) are usually being employed.

The RCWA and the modal approach are both rigorous methods that solve Maxwell's equations without approximations. It can be shown that both approaches are equivalent [48], [49]. The difference between them is the choice of the electromagnetic field representation inside the structure. The starting point for the RCWA are Maxwell's equations. The RCW equations are then derived by expanding the field into space harmonics. For a physical understanding these space harmonics inside the crystal can be thought of as a representation of the diffracted beam orders outside the crystal. The partial fields inside the crystal are then considered to be diffracted waves that can interchange energy as they travel through the crystal [48]. Approaches of developing and analysing this rigorous theory were done by Gaylord and Moharam in various papers. The theory was mostly employed regarding 1D diffraction gratings that have a sinusoidal modulation. However, a 3D generalization was also recently developed [15].

In this thesis the RCWA algorithm is used for simulating the diffraction curves from the PCs. The first case concerns the woodpile-structured PC. For simulating the scattering from these PCs a commercial software called *DiffractMod* was used. The details on the use of the programme are described in chapter 5. The basic idea of using the RCWA algorithm is to subdivide the crystal into a set of computational layers in stacking direction. If the layers are chosen small enough, the permittivity does not vary in stacking z-direction. So in this case one just has to solve a 2D problem for each layer. Then one has to turn over the proper functions at the boundaries regarding the next layer. That is why this method is also known as transfer matrix method. The fields in one layer are parameterized according to Bloch's theorem, the field components in a this layer can be written as

$$
E_j(x,y,z) = e^{i\,(x \cdot k_{o\,x} + y \cdot k_{o\,y})} \sum_{p,q} e^{i\left(\frac{2\pi}{\Lambda_x}px + \frac{2\pi}{\Lambda_y}qy\right)} \sum_m a_{j\,p\,q\,m} \cdot \left(f_m \cdot e^{i\,\kappa_m \cdot z} + g_m \cdot e^{-i\,\kappa_m \cdot z}\right)
$$

$$
H_j(x,y,z) = e^{i\,(x \cdot k_{o\,x} + y \cdot k_{o\,y})} \sum_{p,q} e^{i\left(\frac{2\pi}{\Lambda_x}px + \frac{2\pi}{\Lambda_y}qy\right)} \sum_m b_{j\,p\,q\,m} \cdot \left(f_m \cdot e^{i\,\kappa_m \cdot z} - g_m \cdot e^{-i\,\kappa_m \cdot z}\right) \tag{2.24}
$$

where the z-component of the permittivity is assumed to be constant and $j = x$, y [50]. In chapter 5 the equations (2.24) are further discussed.

The second case is the one concerning the sinusoidal 3D phase lattices. In this case the subdivision into layers and their stepwise solution via the former approach is not feasible. However, the fact that the permittivity distribution is sinusoidal simplifies the problem to solve. The permittivity can be expressed as a finite sum of Fourier expansion coefficients, differing from (2.15) where the inverse permittivity is expanded to an infinite series.

$$\epsilon(\mathbf{r}) = \epsilon_0 + \epsilon_1 \cos(\mathbf{k}_1 \cdot \mathbf{r}) + \epsilon_2 \cos(\mathbf{k}_2 \cdot \mathbf{r}) + \epsilon_3 \cos(\mathbf{k}_3 \cdot \mathbf{r}) \tag{2.25}$$

From the previous equation it is clear that only the real parts of the Fourier expansion are considered. Moreover, the Fourier coefficients are limited to four non-zero ones as well as the number of eigenvalue problems.

$$\tilde{\epsilon}(\mathbf{G}) \cong \epsilon_1 \cdot \delta(\mathbf{G} - \mathbf{k}_1) + \epsilon_2 \cdot \delta(\mathbf{G} - \mathbf{k}_2) + \epsilon_3 \cdot \delta(\mathbf{G} - \mathbf{k}_3) + \epsilon_0 \cdot \delta(\mathbf{G}) \tag{2.26}$$

The numerical computation is then limited to a few reciprocal lattice vectors and so a good convergence is guaranteed in a reasonable time frame.

For the samples considered in this thesis it has to be mentioned that at a thickness of 300μm the assumption of an infinite lattice can be made while that is not the case for the WP structured PCs. Due to the aforementioned sinusoidal permittivity it is sufficient to decompose the wave fields into three spatial parts. That is before entering the crystal, inside the crystal and behind the crystal. A further decomposition inside the crystal is not necessary.

$$\mathbf{E}^{(1)}(\mathbf{r}) = \mathbf{A} \exp(-i\mathbf{k}_0\mathbf{r}) + \sum_{\mathbf{H}} \mathbf{R}_{\mathbf{H}} \exp(-i\mathbf{k}_{r,\mathbf{H}}\mathbf{r}) \tag{2.27}$$

$$\mathbf{E}^{(2)}(\mathbf{r}) = \sum_{\mathbf{H}} \mathbf{S}_{\mathbf{H}}(z) \exp(-i\mathbf{q}_{\mathbf{H}}\mathbf{r}) \tag{2.28}$$

$$\mathbf{E}^{(3)}(\mathbf{r}) = \sum_{\mathbf{H}} \mathbf{T}_{\mathbf{H}} \exp(-i\mathbf{k}_{t,\mathbf{H}}\mathbf{r}) \tag{2.29}$$

These approaches have been introduced in [15]. The wave vector k_0 describes the incident field while the vectors $\mathbf{k_r}$ and $\mathbf{k}_t$ describe the transmitted diffracted and reflected beams. The $\mathbf{q_H}$ vector is the difference vector of the incident and the different diffracted beams depending on the reciprocal lattice vectors $\mathbf{H}$. The difference compared with the modal methods is the explicit depth dependence of the Fourier coefficients $\mathbf{S_H}(z)$ that are known as the space harmonics. At the boundaries of the cyrstals (1), (2) and (2), (3) the tangential components of the wave vectors have to match as already discussed in the previous section.

A rigorous treatment for a solution of such kind of structures has been developed in reference [15]. The advantage of the model is its good convergence that is due to the permittivity profile.

2.3. Approximating approaches

Scattering from a high refractive index contrast PC can only be successfully modelled by numerical solution of Maxwell's equations. Nonetheless, the scattering potential becomes weaker for a reduced contrast and so the possibility to find solutions based on ab-initio approximations of Maxwell's equations arises.

One aim of this work is to apply such simplifying approximations for the scattering from three-dimensional photonic crystals. Although a fully numerical simulation will give the exact scattering curves, it lacks the phenomenological understanding like an analytical description.

2.3.1. X-ray approximation

Since 1912 when the diffraction of X-rays at atomic crystals was experimentally discovered by Laue and co-workers who first received a diffraction pattern from a crystal of copper sulfate, the investigation of matter by X-ray diffraction has been steadily improved. Structure determination with X-rays has become a valuable tool to investigate the properties of crystalline matter in a non-destructive way. Another point of the first interpretation was that X-rays are electromagnetic radiation of short wavelength.

In the following a short summary of X-ray diffraction is given because the techniques developed to investigate matter can prove useful for the further interpretation and investigation of light diffraction from PCs. In principle, this is due to the fact that the X-ray scattering can be modelled in a simpler way because the scattering potential is much weaker than for high contrast PCs. That is why approximative techniques have been very successful in this field. Few terms like kinematic and dynamic scattering or the concept of the Ewald sphere that have originated in the X-ray field of research will be introduced and used throughout this thesis. The kinematic approximation is based on what is shown in [51] while the dynamic approximation refers to [52] and [53].

Scattering from single electrons

At first the scattering of X-rays at electrons is discussed because the main mechanism of X-ray diffraction is due to the interaction with the electrons inside the material. The interaction with the nucleus is negligible. The classical understanding of scattering of X-rays (wave

vector $\mathbf{k}$) from a single electron is that the electron placed in the X-ray beam starts to vibrate and then emits electromagnetic radiation itself (wave vector $\mathbf{k}'$). In this process only elastic scattering is assumed so that the wavelength stays the same ($\mathbf{k}' = \mathbf{k}$). This assumption holds true for wavelengths of few Ångström ($1\text{Å}=10^{-10}$m). The classical formulation leads to the so-called Thomson scattering where the differential cross-section (the probability to observe a scattered particle per solid angle unit) is given by the square of the Thomson scattering length.

The next step is the description of scattering by multiple electrons. Here, the phase between the scattered waves becomes important. For two electrons it is given by $\phi = \mathbf{q} \cdot \mathbf{r} = (\mathbf{k} - \mathbf{k}') \cdot \mathbf{r}$. For an ensemble of N electrons the scattering can be expressed by the scattering amplitude that is given by: $A(\mathbf{q}) \propto \sum_{\mathbf{r}_n} \exp(i\mathbf{q}\mathbf{r}_n)$

Kinematic scattering of regular crystals

The electrons in an atom cannot be located exactly. Thus, they are considered to be a charge cloud orbiting the nucleus. The electrons can be described by a number density $\rho(\mathbf{r})$. The charge density is subsequently given by $-e\rho(\mathbf{r})$. In order to obtain the scattering amplitude for the whole atom one has to integrate the number density weighted with the corresponding phase factor $\exp(i\mathbf{q}\mathbf{r})$. This is also known as the atomic form factor.

$$f_{\text{Atom}}(\mathbf{q}) = \int_{\text{Atom}} \rho(\mathbf{r}) \exp(i\mathbf{q}\mathbf{r}) \, \mathrm{dV} \tag{2.30}$$

From (2.30) it becomes clear that the atomic form factor can be viewed as the Fourier transform of the electronic distribution.

For a crystalline material one assumes that the atoms are located in a regular lattice where the center of the atoms are given at certain positions defined by $\mathbf{R_n} = n_1\mathbf{a}_1 + n_2\mathbf{a}_2 + n_3\mathbf{a}_3$, where the $\mathbf{a}_i$ are the base vectors and n_i integer numbers. The unit cell is spanned by the vectors $\mathbf{a}_i$. It is the smallest building block of the crystal. If one considers the scattering from such a structure one has to consider the scattering from the electrons of the atoms located at the lattice points. There is then of course a special phase relation between the scattering electrons throughout the crystal. Due to the periodicity one can factorize the scattering amplitude into two terms, one is the unit cell structure factor (first sum in (2.31)) and the other one is the lattice sum over the whole crystal (second sum in (2.31)).

$$f_{\text{Crystal}}(\mathbf{q}) = \sum_{\mathbf{r}_j} f_{j,\,\text{Atom}}(\mathbf{q}) \exp(i\mathbf{q}\mathbf{r}_j) \sum_{\mathbf{R_n}} \exp(i\mathbf{q}\mathbf{R_n}) \tag{2.31}$$

Since one has to sum up all the lattice points it is clear that for atomic crystals the lattice

sum has an exceptionally large number of terms. Generally, that sum will have a small value if the complex phase components are equally distributed on the unit circle. This is not the case only if the the product of the lattice point positions and the wave vector transfer is a multiple of 2π. It can be shown that this condition is satisfied if the transfer wave vector $\mathbf{q}$ is equal to a reciprocal lattice vector $\mathbf{G}_{hkl} = h\mathbf{a}_1^* + k\mathbf{a}_2^* + l\mathbf{a}_3^*$ with Miller indices (hkl) .

$$\mathbf{G}_{hkl} = \mathbf{q} \tag{2.32}$$

This is the so-called Laue condition for diffraction. It is equivalent to Bragg's law for diffraction [51].

In order to calculate the intensity it is necessary to evaluate the lattice sum for finite crystals.

$$S(\mathbf{q}) = \sum_{\mathbf{R_n}} \exp(i\mathbf{q}\mathbf{R_n}) \tag{2.33}$$

With (2.32) the equation yields:

$$S(hkl) = \sum_{n_1 n_2 n_3} \exp(i\mathbf{G}_{hkl}\mathbf{R_n}) \tag{2.34}$$

where the vector $\mathbf{n}$ is given by the triplet (n_1, n_2, n_3). Further calculations yield:

$$S(hkl) = \sum_{n_1=1}^{N_1} \exp(i2\pi h n_1) \sum_{n_2=1}^{N_2} \exp(i2\pi k n_2) \sum_{n_3=1}^{N_3} \exp(i2\pi l n_3)$$
$$\Rightarrow S(hkl) = \frac{\sin(N_1\pi h)}{\sin(\pi h)} \frac{\sin(N_2\pi k)}{\sin(\pi k)} \frac{\sin(N_3\pi l)}{\sin(\pi l)} \tag{2.35}$$

This means that the lattice sum strongly depends on the number of unit cells $N = N_1 \cdot N_2 \cdot N_3$. For an infinitely large crystal (i.e. large number of unit cells) the lattice sum will degenerate into a product of delta functions.

Another important step is the simplification of the unit cell structure factor itself. For constituents of the same kind (atoms) the structure factor can be decomposed into a form factor and a phase summation factor.

$$f_{\text{UC}} = \sum_{\mathbf{r}_j} f_{j,\,\text{Atom}}(\mathbf{q}) \exp(i\mathbf{q}\mathbf{r}_j) = f_{\text{Atom}}(\mathbf{q}) \cdot \underbrace{\sum_{\mathbf{r}_j} \exp(i\mathbf{q}\mathbf{r}_j)}_{f_{\text{Struct}}(hkl)} \tag{2.36}$$

The transfer wave vector in the structure sum can be replaced by a reciprocal lattice vector,

so that just the positions in the unit cell have to be summed up. The 'atomic' form factor is the only element in this consideration that remains explicitly wave-vector-dependent. The scattering amplitude can then be decomposed into the three aforementioned parts, the structure factor, the atomic form factor and the lattice sum.

$$f_{\text{Crystal}} = f_{\text{Struct}}(hkl) \cdot S(hkl) \cdot f_{\text{Atom}}(\mathbf{q}) \tag{2.37}$$

The measured intensity of a diffracted beam due to the plane (hkl) which is the experimentally accessible quantity, is given by the absolute squared value of the sattering amplitude, so it follows:

$$I_{hkl}(\mathbf{q}) = |f_{\text{Struct}}(hkl)|^2 \cdot |S(hkl)|^2 \cdot |f_{\text{Atom}}(\mathbf{q})|^2 \tag{2.38}$$

This kinematic scattering is a geometric description of the scattering process. As one can see it has not been deduced straight from Maxwell's equations but some ab-initio simplifications were made. One is that due to the weak scattering potential and the large number of unit cells the Laue equation (2.32) was assumed to be the only condition for constructive interference of the scattered waves. The kinematic scattering has proved to be a useful and easy to understand tool to describe diffraction. One example is the Ewald sphere construction. This is a graphical representation of the Laue condition. For simplification one can consider the two-dimensional case. First an incident beam with monochromatic radiation will be assumed. The beam $\mathbf{k}$ is drawn from the origin of the reciprocal lattice to a point A in reciprocal space. The point A is then taken as the center of a circle (sphere) with radius $|\mathbf{k}| = 2\pi/\lambda$. If other reciprocal lattice points except the origin lie on the circle, the condition for diffraction is fulfilled because the transfer wave vector $\mathbf{q}$ equals a reciprocal lattice vector. Via rotation of the crystal one can also access other diffraction spots. Alternatively, the angle of incidence can be altered. If there is more than one spot on the circle, then this means simultaneous diffraction from different lattice planes. In the second case of polychromatic radiation the available wave vectors vary in their length ($|\mathbf{k}_{\min}| \leq |\mathbf{k}| \leq |\mathbf{k}_{\max}|$). They are limited by a minimum wavelength and a maximum one. In this case the accessible reciprocal lattice points are much larger because the points allowing for diffraction are given by the reciprocal space that results from the subtraction of the two Ewald circles (spheres) for $\lambda_{\max}$ and $\lambda_{\min}$. The red-coloured semi-transparent area in figure 2.3(b) indicates the reciprocal lattice points that will allow for simultaneous diffraction.

The kinematic theory as an approximating approach has some limitations [52]. First of all it violates the conservation of energy [54]. The second limitation is that it is assumed that each scattering object contributes the same amount to the diffraction. This does neither
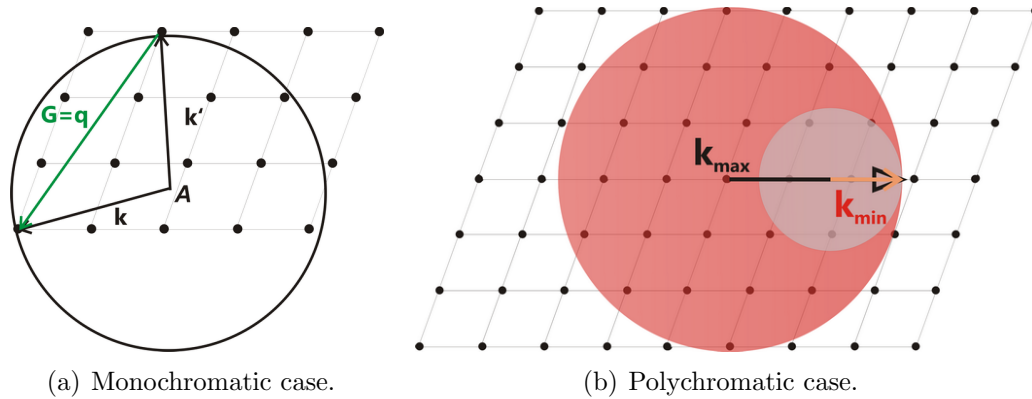
(a) Monochromatic case.   (b) Polychromatic case.

Fig. 2.3.: Ewald sphere construction.

include any interaction with matter nor does it include the fact that some energy may have already been reflected. In the next section the dynamic theory is shortly described that will overcome some of the limitations of the kinematic approach but it is still an approach to Maxwell's equations.

Dynamic scattering

The dynamic scattering of X-rays from crystals is in principle no approximate theory but also a rigorous one. By comparison with the kinematic theory it takes into account multiple scattering effects (in its rigorous form) and it also takes into account refraction at the interface of the crystal as well as interference and extinction effects.

However, mostly not the rigorous theory is employed but some approximations are made depending on the problem in order to simplify it sufficiently to make it solveable.

There are numerous descriptions of dynamical scattering in its different facets [52], [53]. In [53] the diffraction is explained as taking place as a single entity. Furthermore, the wave field cannot be completely distinguished in an independent incident field and diffracted wave fields but has to be considered as a single one in which an incident field and the diffracted fields are coupled and interchange energy as they traverse through the crystal.

From this point of view the RCW theory and the dynamical diffraction have been developed by different communities but have the same physical background, they just differ from their field of application.

In the dynamic theory of X-ray scattering one has to solve Maxwell's equations for a complex periodic permittivity. This can be expressed by the electron density which due to its periodicity can be depicted by a Fourier sum (series) similar to the expansion in (2.15). The complex permittivity is furthermore dependent on the frequency of the electronic motion.

Following [53] one can write the permittivity as

$$\epsilon(\mathbf{r}) = 1 - \Gamma \sum_{\mathbf{H}} F(\mathbf{H}) \exp(-i\mathbf{H} \cdot \mathbf{r}) \tag{2.39}$$

where the $F(\mathbf{H})$ are generally complex quantities where the imaginary parts are taking absorption and resonance into account. Having received an expression for the permittivity, Maxwell's equations are used to obtain a solution for the wave field inside the crystal. For this one can use a plane wave expansion same as the Fourier expansion in (2.17). The resulting Bloch waves satisfy Maxwell's equations. Further calculations lead then to a fundamental set of equations (cf. equation A12 in [53]).

In practice, these fundamental equations could be solved numerically but at this point an approximation usually valid for X-rays in crystals is made. This is known as the *two-beam approximation*. This means that for all the reciprocal lattice vectors in the Fourier expansion only one is used due to the assumption that only one reciprocal lattice point is so close to the Ewald sphere that it is the only one that will contribute considerably to the diffraction.

2.3.2. Two-wave approximation to rigorous coupled-wave theory

The two-wave approximation is applicable for crystals that have a small permittivity modulation. In the framework of this thesis the sinusoidally modulated three-dimensional phase lattices are the crystals for which such an approximation is useful. First the 1D latices are considered and later on a generalization to 3D lattices is shown.

1D - case

The two-wave approximation to the RCW theory was discussed by Kogelnik [14] for thick hologram gratings. It has been shown that this approximation is applicable for 1-D gratings that have a sinusoidal permittivity modulation with an amplitude that is adequately small. For the 1D-case only two waves from the rigorous coupled-wave equations are considered. Furthermore, the second derivatives of the field amplitudes are neglected. This leaves only two differential equations that couple two space harmonics. In [48] these equations are depicted as:

$$\frac{\mathrm{d}S_0(z)}{\mathrm{d}z} + ic_1 S_1(z) = 0 \tag{2.40}$$

$$\frac{\mathrm{d}S_1(z)}{\mathrm{d}z} + ic_2 S_1(z) + ic_3 S_0(z) = 0 \tag{2.41}$$

The coefficients c_1, c_2, c_3 are depending on wavelength, refractive index modulation and grating thickness. Whereby the S_0, S_1 are the depth dependent expansion coefficients of the electric field similar to the RCWA approach given in (2.28). For the so-called Kogelnik theory analytical expressions can be derived from (2.40) and (2.41) that allow calculations of the difffraction efficiencies.

3D - case

The 3D-case for the two beam approximation of the RCW theory is comparable to what has already been introduced in the previous section and what is called the dynamic X-ray scattering from atomic crystals in its two beam approximation. In its 3D form the scattering problem can be described by the Takagi-Taupin equations [52].

$$\frac{\partial \mathbf{D_0}}{\partial \mathbf{s_0}} + i c_1 \mathbf{D_h} = 0 \tag{2.42}$$

$$\frac{\partial \mathbf{D_h}}{\partial \mathbf{s_h}} + i c_2 \mathbf{D_0} + i c_3 \mathbf{D_h} = 0 \tag{2.43}$$

In the above equations the electric displacement field $\mathbf{D}$ was used. The field was assumed to be decomposable into a Fourier series $\mathbf{D} = \sum_{\mathbf{h}} \mathbf{D_h}(\mathbf{r}) \exp(i(\mathbf{k}+\mathbf{h})\mathbf{r})$, where the $\mathbf{D_h}(\mathbf{r})$ are the position-dependent Fourier expansion coefficients. One approximation in this case is that the variations of the $\mathbf{D_h}(\mathbf{r})$ are small so one can drop second order derivates. The second approximation is that only one reflection is close enough to the Ewald sphere to give considerable diffraction. So that only two beams are considered. In this case they are given in (2.42) and (2.43) by $\mathbf{D_h}$ and $\mathbf{D_0}$. The coefficients c_1, c_2, c_3 include wavelength, polarization and the susceptibility. The usage of the dielectric displacement was chosen in order to show in (2.42) and (2.43) the similarity of the 3D - case to the 1D - case.

3. Scattering Geometry

The aim of the experimental as well as the theoretical investigation of the light diffraction from three-dimensional photonic crystals is to get a deeper understanding of the scattering mechanism. The focus of the investigation is especially directed towards the understanding of the diffraction of the different scattering orders.

In practice, a light beam is incident upon a photonic crystal. After the interaction of the beam with the PC the primary beam, also called zero order diffracted beam, leaves the crystal without deviation. In the far field the diffracted light beams are spatially separated and can be visualized on a screen. For a weakly diffracting lattice this can be explained by the so-called Laue diffraction. Moreover, an indexing of the diffraction orders is possible this way.

The scattering efficiencies of single diffraction orders are then recorded as a function of the incident angle of the wave vector. This angle is changed by rotation of the PC. Furthermore, the position and scattering efficiency of the observed diffracted beam change while changing the incident wave vector, so a proper experimental geometry has to be defined.

In section 3.1 of this chapter the concept of the effective refractive index and the influence of the high mode density is discussed. Whereas in 3.2 the Laue equations are introduced. In 3.3 the used coordinate systems are described, whereas in section 3.4 the physical background of the scanning methods in reciprocal space is explained.

3.1. Effective refractive index and conservation of the parallel wave vector component

The difference in the law of refraction for PCs compared to homogeneous media has already been introduced in section 2.2.1. One important outcome is that the refractive index of the PC is a function of the incident vector beam $n_{\mathrm{PC}}(\mathbf{k}_{\mathrm{ext}})$. For PCs the term effective refractive index n_{eff} is also often used to distinguish it from homogeneous material and also because it is mode-dependent. In most cases a determination of the effective RI is possible by calculation

of the dispersion relation. It is defined by

$$n_{\text{eff}}(\mathbf{k}) = \frac{c}{\left|\frac{\partial \omega(\mathbf{k})}{\partial \mathbf{k}}\right|} \tag{3.1}$$

Due to the fact that for a ratio of $a/\lambda \approx 1.4$ the mode density gets higher the more refractive contrast the PC exhibits, the refractive index itself cannot be determined accurately. For a high contrast one has therefore no choice but to approximate the effective RI by a weighted average.

Outside the PC the incident beam is named $\mathbf{k}_{\text{ext}}$ and after being refracted at the interface and traversing inside the PC the beam is given by $\mathbf{k}_{\text{int}}$. The important point in this consideration is that the wave vector can be decomposed into a parallel and perpendicular component $\mathbf{k} = k_\perp \mathbf{e}_\perp + k_\parallel \mathbf{e}_\parallel$ where the parallel component has to be conserved upon refraction at the interface $\mathbf{k}_{\text{int},\parallel} = \mathbf{k}_{\text{ext},\parallel}$. Another refraction takes place when the beam exits the PC. Then the parallel wave vector component is conserved as well.

3.2. Laue equations

In the previous chapter details about the electromagnetic field interaction have been discussed. One main focus of the investigations in this thesis lies on determining scattering curves and efficiencies of certain Laue reflections. For 3D crystals there is usually more than one diffracted beam. The diffracted beams can be visualized on a screen behind the crystal and are called Laue reflections or simply Laue spots. They are distinguished by Miller indices which indicate the lattice planes that are mainly contributing to the diffraction, although this is mostly true for low scattering potentials. In this case one can predict the diffraction spots by the so-called Laue equations.

The Laue equations are named after Max von Laue and they describe the geometric conditions under which incident waves are diffracted by a crystal. The direction of the incident wave $\mathbf{k}_{\text{ext}}^0$ is given by $\mathbf{n}_o = \frac{\mathbf{k}_{\text{ext}}^0}{\left|\mathbf{k}_{\text{ext}}^0\right|}$ and the i diffracted waves have directions $\mathbf{n}_i = \frac{\mathbf{k}_{\text{ext}}^i}{\left|\mathbf{k}_{\text{ext}}^i\right|}$. Furthermore, the crystal lattice is spanned by the vector set $\{\mathbf{a}_j\}_{j=1,2,3}$. So the Laue equations can be expressed as

$$\begin{aligned}
(\mathbf{n}_i - \mathbf{n}_0) \cdot \mathbf{a}_1 &= \lambda \cdot h \\
(\mathbf{n}_i - \mathbf{n}_0) \cdot \mathbf{a}_2 &= \lambda \cdot k \\
(\mathbf{n}_i - \mathbf{n}_0) \cdot \mathbf{a}_3 &= \lambda \cdot l
\end{aligned} \tag{3.2}$$

with Miller indices hkl. Equivalent to the Laue equations is Bragg's law. It can be shown

that the Laue equations correspond to the kinematical condition for diffraction:

$$\mathbf{G} \;=\; \frac{2\pi(\mathbf{n} - \mathbf{n_0})}{\lambda} \;=\; \mathbf{q} \tag{3.3}$$

The derivation can be done by multiplying the reciprocal lattice vector $\mathbf{G}$ with one of the real space lattice vectors $\{\mathbf{a}_j\}_{j=1,2,3}$. The three resulting equations correspond to the Laue equations. With this geometrical description, no statement about the real scattering processes are made, it just serves as a tool to identify reflections and to predict their positions. However, for low contrast PCs as well as for holographic lattices this should be a valid geometric approach. In order to visualize the expected diffraction patterns several examples are shown in figure 3.1.

3.2.1. 2D Miller indices

For three-dimensional crystals the diffracted beams can be indexed with Miller indices hkl. A beam incident parallel to the surface normal will cause a diffraction pattern depending on the crystal structure like depicted in figure 3.1. Firstly, it is visible that only two Miller indices have been used (hk). Secondly, every diffraction experiment in this thesis is done in transmission geometry which means that sometimes a letter T is added to the Miller indices. The use of two-dimensional indices is sufficient because the third index can be obtained experimentally by the scattering curves. This will be described in detail in the next section. However, regarding the special crystallography of the photonic phase lattices it is sometimes intelligible to mention the third index.

Regarding the nomenclature of the reflection, negative values for (hkl) are described by adding a minus-sign in front of the integer value which is in contrast to the standard procedure in crystallography where an overbar is required for negative values (e.g. $(-10)T$ corresponds to $(\bar{1}0)T$).

3.3. Definition of the scattering coordinate system

For a proper description of the scattering geometry a definition of the coordinate systems (CS) has to be made. Two coordinate systems are of importance in this consideration. The laboratory CS is the one that describes the incoming beam, the diffracted beams and sample rotation as well as translation. The crystal CS describes the inherent structure of the crystal by real space and reciprocal space lattice vectors. The crystal CS is of special importance when indexing the diffraction spots by Miller indices.

The laboratory CS is defined in figure 3.2. When all angles are set to zero the incoming

(a) LD pattern for a simple hexagonal crystal.

(b) LD pattern for a trigonal structure, indexed with hexagonal Miller indices.

(c) LD pattern for a tetragonal structure.

Fig. 3.1.: Schematic figure of the Laue diffraction pattern for different crystal structures **in transmission geometry** (*T*). 2D Miller indices have been used. The incident beam direction is parallel to the **c** vector. For reasons of clarity and comprehensibility some reflections are coloured slightly different. The primary non-diffracted beam is given by (00).

beam is perpendicular to the $x - y$-plane. In this case the crystal CS and laboratory CS match.

Experimentally, the angles and the translation of the crystal can be changed with the help of a diffractometer.
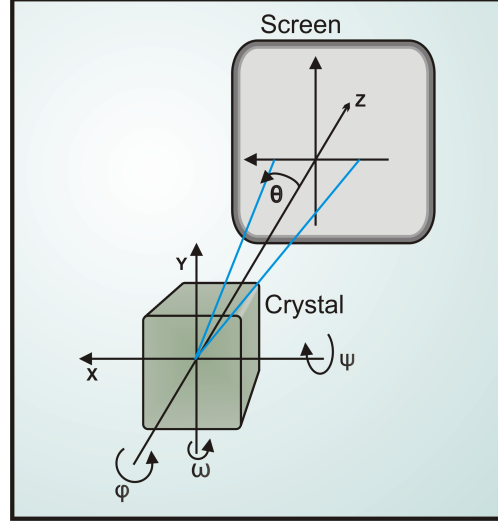

Fig. 3.2.: Laboratory CS and definition of angles

The measurement of the scattering curves is experimentally restricted to reflections located in the $x - z$-plane. In order to access different reflections the angles ψ and ϕ can be used to rotate the PC which subsequently causes a rotation of the diffraction pattern. The scattering curves for different reflections are recorded by rotation of the sample around the ω-axis and a simultaneous detection of the diffracted beam at the scattered angle θ. Since the position of the reflection depends on the incident angle ω_{inc} it is necessary to find an expression that relates the incident angle with the scattering angle θ. When considering the CS it is clear that the incident angle ω_{inc} is connected with the sample rotation angle ω via $\omega_{\mathrm{inc}} = -\omega$.

The incident beam is given by $\mathbf{k}_{\mathrm{ext}}^0$, while the considered diffracted beam outside the crystal is named $\mathbf{k}_{\mathrm{ext}}^{\mathrm{diff}}$. Inside the crystal the corresponding subscript **int** is used. The parallel wave vector is conserved which means that $\mathbf{k}_{\mathrm{ext},\parallel}^0 = \mathbf{k}_{\mathrm{ext},\parallel}^{\mathrm{diff}}$. From the last equation the following relation is deduced $k_{\mathrm{ext},\parallel}^{\mathrm{diff}} = k_{\mathrm{ext}}^0 \sin(\theta - \omega_{\mathrm{inc}})$. Therefore, the $\theta - \omega$ dependence can be expressed as:

$$\theta(\omega, \mathbf{G}_\parallel) = \arcsin\left(\frac{k_{\mathrm{ext},\parallel}^{\mathrm{diff}}}{k_{\mathrm{ext}}^0}\right) + \omega_{\mathrm{inc}} = \arcsin\left(-\sin(\omega) + \frac{\lambda}{d(\mathbf{G}_\parallel)}\right) - \omega \tag{3.4}$$

A more detailed derivation of the second step in (3.4) is given in the appendix A. The parameters in (3.4) are the wavelength of the incident beam λ and the in-plane lattice

spacing $d(\mathbf{G}_\parallel)$ that is dependent upon the in-plane reciprocal lattice vector $\mathbf{G}_\parallel$ by

$$d(\mathbf{G}_\parallel) = \frac{2\pi}{\left|\mathbf{G}_\parallel\right|}.$$

Where the in-plane reciprocal lattice vector is given by $\mathbf{G}_\parallel = h\mathbf{a}^* + k\mathbf{b}^*$. Each one of the lattice vectors is given in the crystal CS, therefore they do not depend on the rotation angles. The WP PC has lattice spacings that depend on the lattice constant and the Miller indices as follows:

$$d_{\mathrm{WP}}(\mathbf{G}_\parallel) = \frac{2\pi}{\left|\mathbf{G}_\parallel\right|} = \frac{a}{\sqrt{h^2 + k^2}}$$

For the holographic phase lattices the decomposition is more difficult if one assumes the trigonal unit cell because there is no out-of-plane vector as there is for the WP structured PCs. Because of this one can use the hexagonal unit cell with ABC stacking. For the hexagonal unit cell the in-plane distances are thus given by:

$$d_{\mathrm{Hex}}(\mathbf{G}_\parallel) = \frac{2\pi}{\left|\mathbf{G}_\parallel\right|} = \frac{\sqrt{3}a}{2\sqrt{h^2 + k^2 + hk}}$$

3.4. Scanning methods

In the previous section the $\omega - \theta$ dependence in the laboratory CS was derived. This relation makes it possible to scan the efficiency of the diffracted beam in angular space with a knowledge of the wavelength and in-plane lattice constant. The scanning method works for the monochromatic case in such a way that a change of the sample rotation angle ω in certain steps $\Delta\omega$ is done and for each value of ω the scattering efficiency at the position $\theta(\omega, \mathbf{G}_\parallel)$ is recorded. For a more detailed analysis of the scattering mechanism it will be shown how the measured intensity and the rotation angle ω can be transferred into the reciprocal space.

3.4.1. Transfer to reciprocal space

Similar to the scanning methods known from X-ray diffractometry the transfer wave vector $\mathbf{q} = \mathbf{k}_{\mathrm{int}}^{\mathrm{diff}} - \mathbf{k}_{\mathrm{int}}^0$ plays a central role in the description of the scattering process. This vector is also decomposable into a perpendicular and parallel part $\mathbf{q} = \mathbf{q}_\perp + \mathbf{q}_\parallel$. The parallel wave

vector component is conserved and is therefore given by a reciprocal in-plane lattice vector.

$$\mathbf{q}_{\parallel} = \mathbf{G}_{\parallel} \tag{3.5}$$

$$\mathbf{q}_{\perp} = \frac{2\pi n_{\mathrm{eff}}}{\lambda} \left(\sqrt{1 - \left(-\frac{\sin(\omega)}{n_{\mathrm{eff}}} + \frac{\lambda}{d(\mathbf{G}_{\parallel}) n_{\mathrm{eff}}} \right)^2} - \cos\left(\arcsin\left(\frac{-\sin(\omega)}{n_{\mathrm{eff}}} \right) \right) \right) \cdot \widehat{\mathbf{c}^*} \tag{3.6}$$

The perpendicular wave vector transfer is given as a function of the effective refractive index n_{eff}, the wavelength λ and incident angle of the incoming beam $-\omega$, as well as the in-plane lattice parameter $d(\mathbf{G}_{\parallel})$. An extensive derivation of this equation is given in the appendix A.

By taking a look at the Ewald sphere construction for monochromatic light in figure 3.3 one can see that the perpendicular transfer wave vector can move along the $\mathbf{c}^*$-direction in reciprocal space. One unknown parameter in (3.6) is the angle-dependent effective refractive index which has to be approximated by a volume averaged refractive index.

$$n_{\mathrm{eff}} \approx \sqrt{n_1^2 \cdot \Omega + n_2^2 \cdot (1 - \Omega)} \tag{3.7}$$

For WP PCs with low RI contrast this is usually a valid approximation but for larger contrasts considerable deviations will occur. In this approximation Ω corresponds to the filling factor of the unit cell. For an SU-8 WP crystal the filling factor is given by $\Omega = 0.28$ [55]. For PCs like photonic lattices the RI variation is even smaller and therefore the inherent RI value of the polymer can be taken. The depiction of the perpendicular transfer wave vector $\mathbf{q}_{\perp}$ versus the scattering efficiency is a common and well-established tool in X-ray diffraction. A better understanding is even given by plotting the transfer wave vector $\mathbf{q}_{\perp}$ in terms of Miller indices versus the diffraction efficiency. This is done by dividing $|\mathbf{q}_{\perp}|$ by a reciprocal lattice vector $|\mathbf{c}^*|$:

$$l(\omega, \lambda, \mathbf{G}_{\parallel}) = \frac{|\mathbf{q}_{\perp}|}{|\mathbf{c}^*|} = \frac{c \cdot n_{\mathrm{eff}}}{\lambda} \left(\sqrt{1 - \left(-\frac{\sin(\omega)}{n_{\mathrm{eff}}} + \frac{\lambda}{d(\mathbf{G}_{\parallel}) n_{\mathrm{eff}}} \right)^2} - \cos\left(\arcsin\left(\frac{-\sin(\omega)}{n_{\mathrm{eff}}} \right) \right) \right) \tag{3.8}$$

The relation of the detector angle θ and the sample rotation angle ω which corresponds to the location of the Bragg peak is graphically plotted in figure 3.4. Two cases have been considered. Firstly, the case of the WP PCs (cf. figure 3.4(a)). Here, the relation is plotted for two reflections which are indexed by 2D Miller indices (cf. figure 3.1(c)) and a wavelength of 488nm that corresponds to one of the experimentally used wavelengths. The $\omega - \theta$ relation is valid for all symmetric reflections, i.e. $(01)T$, $(0-1)T$, $(10)T$ and $(-10)T$, when aligning
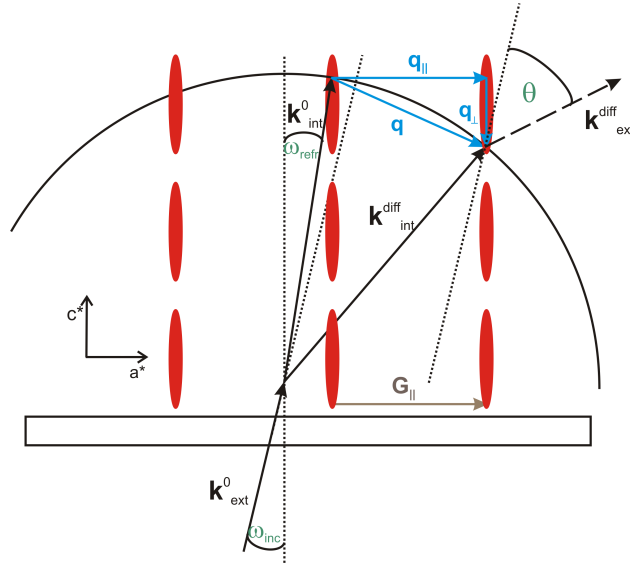
Fig. 3.3.: Ewald sphere construction in the monochromatic case for thin WP PCs. The reciprocal lattice points are degenerated to ellipses (coloured red) in the stacking direction. The incoming beam k_{ext}^0 is first refracted then diffracted. The difference between the diffracted and non-diffracted beam is q. Directly visible is the decomposition into a parallel and perpendicular transfer wave vector. When exiting the crystal, the beam is once more refracted.

the PC with the proper ψ value. In figure 3.4(b) the second case is considered which deals with the holographic PCs. In this case the same holds true as for the previous one except the point that the symmetry depicted in figure 3.1(b) should be reflected by the corresponding ψ values.

For a subsequent transfer to reciprocal space the relation (3.4) connects the sample rotation angle ω with the reciprocal lattice coordinate l. This transfer from angular space to reciprocal space is graphically shown in figure 3.5. From the corresponding formula it is already evident that the length of the out-of-plane vector $\mathbf{c}$ is influencing the transfer to reciprocal space. For the WP structured PCs this value is much smaller than for the holographic PCs, that is why in principle a larger region in reciprocal space can be covered for the holographic PCs. Furthermore, it is obious that next to the out-of-plane lattice vector the in-plane lattice constant is playing an important role in the transfer which is implicitly included in the d-value.

Finally, it should be mentioned that the $\omega - \theta$-dependence is a pure geometrical description and gives no information about the scattering efficiency, so, in practice, not the full range of the sample rotation $\omega \in [-30°; 70°]$ which is depicted in the corresponding figures might be used.
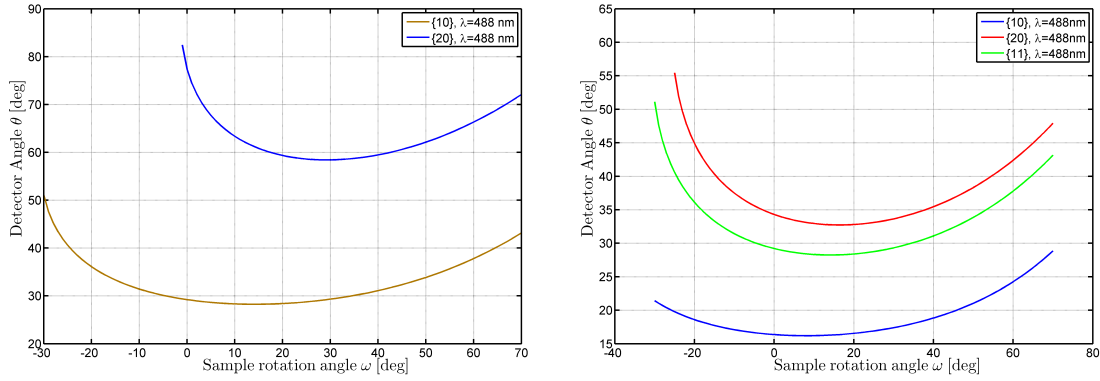
(a) WP structured PCs with an in-plane lattice
constant of 1μm. The black line indicates a re-
gion where no relation is possible.

(b) Holographic lattices with an in-plane lattice
constant of 1.97μm.

Fig. 3.4.: Relation between detector angle θ and sample rotation angle ω for the monochromatic
case $\lambda = 488$ nm. In order to measure the different reflecions $\{hk\}$ an adjustment of the angle
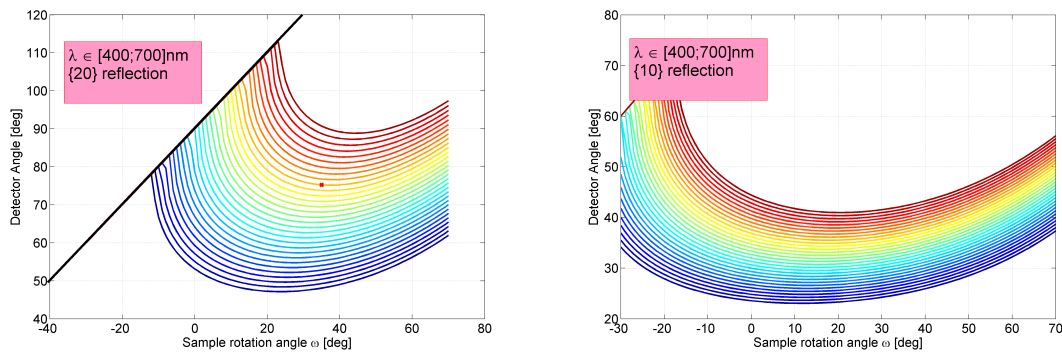ϕ is necessary.
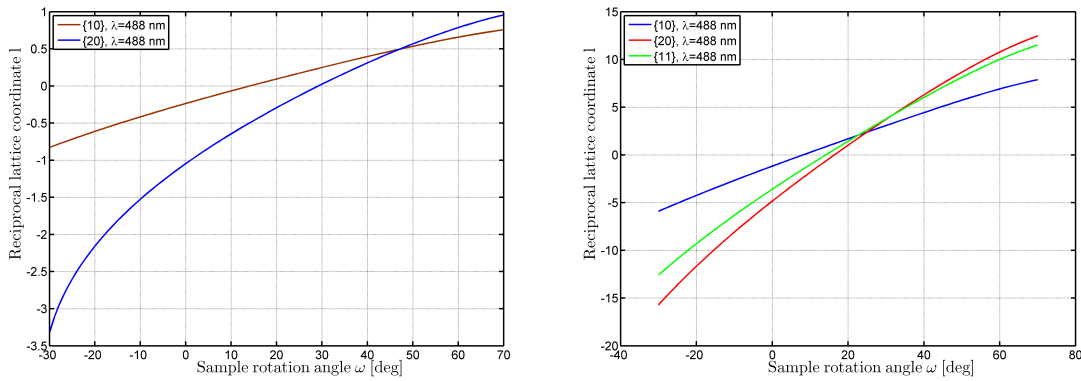
(a) WP structured PCs with an in-plane lattice
constant of 1μm and an out-of-plane constant of
1.4μm.

(b) Holographic lattices with an in-plane lattice
constant of 1.97μm and an out-of-plane constant
of 21.5μm.

**Fig. 3.5.:** Transformation from angular to reciprocal space.

3.4.2. Polychromatic case

The previous considerations included the assumption of a single wavelength $\lambda = 488$ nm. Next to the monochromatic investigation of light scattering at certain wavelengths a complete polychromatic investigation is also desirable. For this reason plots similar to figure 3.4 and figure 3.5 have been created for different wavelengths in the visible light ($\lambda \in [400; 700]nm$) regime.

The wavelength dependence of the $\theta - \omega$ relation for selected reflections and PCs can be found in figure 3.6. These curves exhibit a well-known and predictable behaviour which is that larger wavelengths have a larger diffraction angle.
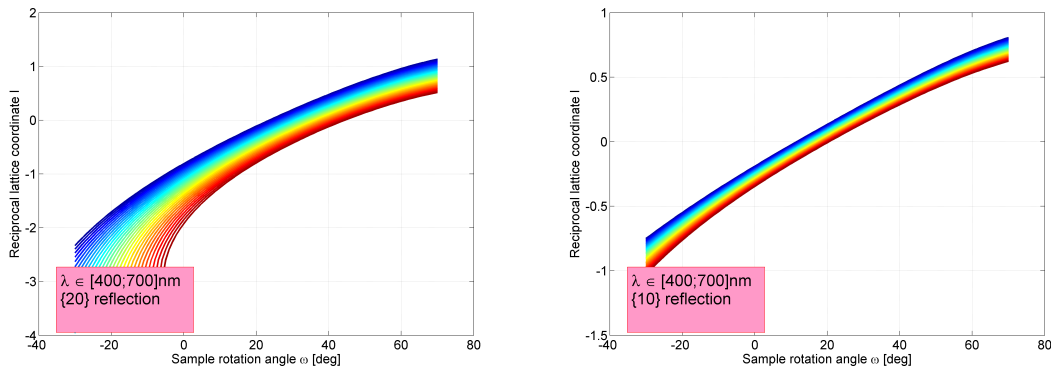

(a) {20} reflections for the WP structured PCs with an in-plane lattice constant of 1μm and an out-of-plane constant of 1.4μm.

(b) {10} reflections for the WP structured PCs with an in-plane lattice constant of 1μm and an out-of-plane constant of 1.4μm.
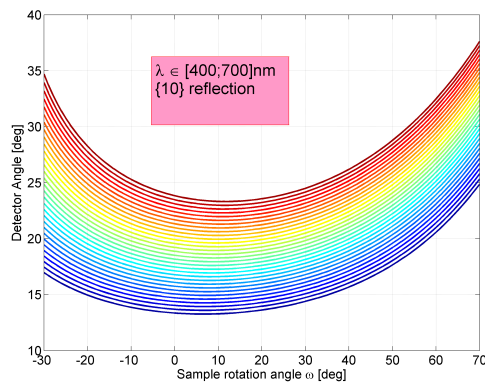
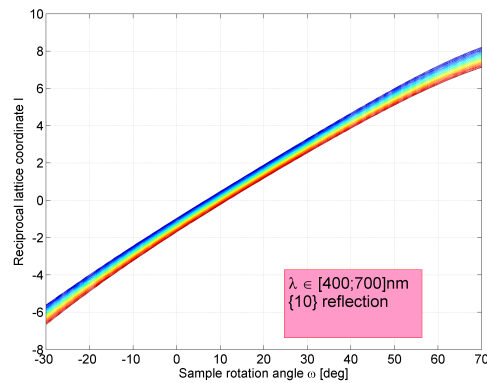
(c) {10} reflections for the holographic lattices with an in-plane lattice constant of 1.97μm and an out-of-plane constant of 21.5μm.

Fig. 3.6.: Relation of the sample rotation angle ω with the detector angle for the polychromatic case in the wavelength range $\lambda \in [400; 700]nm$. The curves for the corresponding wavelengths are colour-coded which means that the 400 nm curve is the blue one and the 700 nm curve is the red one.

The transfer from angular to reciprocal space for polychromatic radiation is shown in figure 3.7. In these three subfigures two different sets of reflection for the WP structured crystal with lattice constant $a = 1\mu m$ are plotted and one set of reflection for the holographic phase lattice.

(a) {20} reflections for the WP structured PCs. (b) {20} reflections for the WP structured PCs.

(c) {10} reflections for the holographic lattices

Fig. 3.7.: Transformation into reciprocal space for the polychromatic case. The curves for the corresponding wavelengths are colour coded which means that the 400 nm curve is the blue one and the 700 nm curve is the red one.

4. Experimental Setup

In this chapter the experimental setup is described. A general overview of the setup is shown in figure 4.1. In the framework of a Master's thesis this setup was developed [11]. Thus, a very detailed description of the experimental setup is given there. Moreover, the setup was tested in order to demonstrate its capability for reproducible measurements. That is why in this thesis this chapter will recapture in short the basic components of the experimental setup and for further details the reader may consult reference [11]. The setup can be decomposed
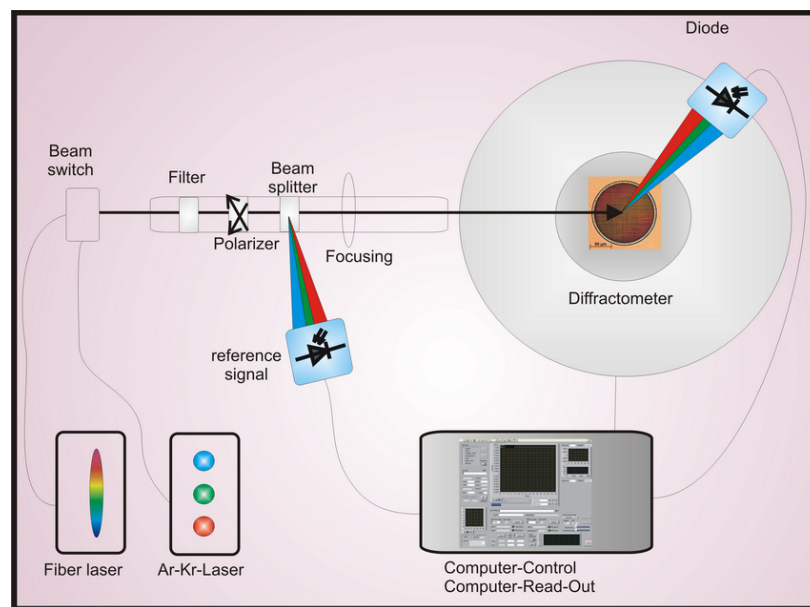

Fig. 4.1.: Scheme of the experimental setup.

into three basic parts. The diffractometer (described in 4.1), the light sources and optical components (described in 4.2) and the control unit (described in 4.3).

4.1. Diffractometer

The diffractometer is one of the central parts of the setup. This diffractometer (Stadi MP-STOE & Cie) is a commercially available one [10]. However, its original field of application was

---

[10]`http://www.stoe.com/pages/products/stadimp.html`

for the use in an X-ray scattering setup. It consists of two goniometers. The first goniometer is responsible for the precise rotation of the sample ω and detector θ rotation. The second goniometer is attached on top of the ω-circle, which means that the second goniometer is rotated around that angle (ω). This goniometer allows the rotation of two additional angles ϕ and ψ (cf. figure 3.2). Additionally, it has a sample stage where the PC can be fixed. This stage can be moved with μm precision in x- and z-direction. An alignment in y-direction has to be done manually.

For the measurements the PC is attached to the sample stage of the goniometer. Assuming that the diffractometer and the beam are aligned in such a way that the beam passes through the center of rotation, the PC has to be moved directly into the beam.

For the experimental analysis it is then crucial to know the magnitude of the errors that can occur. There are the errors that originate from the precision of the goniometer rotation/translation and the errors that stem from the alignment process. In table 4.1 which is taken from [11] the alignable ranges of the diffractometer as well as the errors are tabulated.

Parameter	Range	Equipment Precision	Alignment Precision
ω	$[-140\,°;\,140\,°]$	$0.001\,°$	$0.8\,°$
θ	$[-140\,°;\,140\,°]$	$0.001\,°$	$0.05\,°$
φ	$[-65\,°;\,25\,°]$	$0.05\,°$	$0.1\,°$
ψ	$[0\,°;\,360\,°]$	$0.05\,°$	$0.5\,°$
x'	$[0\,;\,20]$mm	$50\,\mu$m	$0.1\,$mm
y'	$[0\,;\,2]$cm	$0.1\,$mm	$0.1\,$mm
z'	$[0\,;\,10]$mm	$50\,\mu$m	$0.2\,$mm

Tab. 4.1.: Adjustable parameter range and precision. The primed coordinate system $(x'\,y'\,z')$ corresponds to the crystal CS.

4.2. Light sources and optical elements

For the experiments two light sources have been used, since the experimental interest is on the one hand concerning diffraction of a monochromatic beam and the subsequent determination of the diffraction efficiencies and on the other hand the investigation of polychromatic diffraction. To cover both cases an Ar-Kr ion laser as well as a fibre laser have been used.

4.2.1. Ar-Kr ion laser

The first laser to be described is a gas laser that uses ionized gas as a lasing medium, in this case a mixture of Argon and Krypton. The mixture of these two noble gases means that

emission lines from both gases occur. The high number of emission lines ranging from blue to red light create the impression of a white light laser. The employed laser is a commercial product[11]. Due to the age of this model[12] not all emission lines are available anymore. An experimental analysis of the emission lines has shown the strength of each emission line [11].

Despite its white light capabilities this laser will be used in the experimental setup as a monochromatic laser. By employing special filters monochromatic measurements for different wavelengths can be done without changing the setup or the alignment. Due to the lack of intensity of some emission lines, only the more intense lines have been used. These were

- the blue emission line with $\lambda = 488$nm,

- the green emission line with $\lambda = 568.2$nm and

- the red emission line with $\lambda = 647.1$nm.

4.2.2. Fibre laser

A fibre laser was used[13] for experiments with polychromatic radiation. This fibre laser emits a continuous spectrum of white light. According to the data sheet, the emitted wavelengths range from 500nm to 1750nm. The angular divergence of the beam is less than $0.045°$ and the beam has a spectral power density of up to 50μW/nm. Moreover, the laser exhibits good spatial coherence and a pulse width that is smaller than 2ns at a repetition rate of 24kHz and a total output power of 124mW.

In contrast to the Ar-Kr-laser the fibre laser is a pulsed laser and it uses a fibre as a gain medium which is doped by rare elements. By the optical term known as 'supercontinuum generation' the working principle can be described. For that short pulses in the ps- or fs-regime can be coupled into an optical fibre. Due to spectral broadening of the pulses a white light spectrum can be obtained. The usage of a photonic crystal fibre can enhance the effect because it has superior dispersion properties. Further details on the working principle of a fibre laser can be found in [56].

4.2.3. Optical elements

The laser beam created by one of the light sources is altered by several optical elements before it reaches the sample. For the Ar-Kr laser a wavelength filter is applied in order to obtain a monochromatic beam. For the fibre laser an infrared filter is used to suppress wavelengths

---

[11]Omnichrome
[12]date of construction: Nov. 1994
[13]SuperK[TM] Compact, Koheras

above 780nm to avoid heating of the sample. After this the beam passes a polarizer and a beam splitter to create a reference beam for temperature and power monitoring. Finally, the beam passes a lens and is focussed at the rotation center of the diffractometer.

For the WP structured PCs it is essential to focus the beam very tightly because of the limited size of the crystal. This boundary condition is not that important for the holographic lattices due to their sufficiently large size. There are two lenses with different focal lengths available ($f_1 = 100$mm, $f_2 = 200$mm). The lenses are positive achromatic lenses to avoid chromatic aberration in case of the polychromatic beam. For the Ar-Kr laser beam the second lens f_2 was used, while the fibre laser required a stronger focussing and thus the first lens f_1 was used.

The beams can be interpreted by Gaussian beam optics and so the beam width at the focus is reduced the smaller the focus of the lens. Moreover, the smaller the focus is the larger the divergence of the beam. In the focus the beam front can be approximated by plane waves. The latter point corresponds very well with the situation in the experimental setup.

4.3. Control software and electronic parts of the setup

The experiment is mostly computer-controlled. The sample itself has to be aligned manually using the translation stages. The rotational alignment is done via a commercially available software that was distributed with the diffractometer.

The remaining parts of the diffractometer can be controlled using a *LabView* interface (cf. figure 4.2). Furthermore, a remote control can be used to manually rotate the ω and θ circles.

Several different scan methods have been implemented by the software. The θ-scan can be used for alignment which means that at a fixed sample position ω_0 the detector angle θ is rotated in certain step sizes $\Delta\theta$. The respective ω-scan is implemented with a constant value of θ. For the measurements of the diffraction efficiencies the so-called reflection scan was implemented. This reflection scan follows a relation of θ and ω that is given by (3.4). The scan parameters that are necessary for the scan are thus the

- range of the sample rotation angle $[\omega_{\mathrm{min}}; \omega_{\mathrm{max}}]$ and the number of steps,

- distance of the lattice planes of the measured reflection $d(\mathbf{G}_{\parallel})$,

- and the wavelength of the incident beam λ.

The control software receives an input signal from two detectors. These detectors are basically avalanche photo diodes that are operated in reverse-bias. The signal from the photodi-

odes is then electronically converted and further processed via an USB-6009 data acquisition (DAQ) device from National Instruments[14] so that one has a measure of the diffraction efficiency. The control interface was implemented with the possibility to normalize the measured intensity. The detector measuring the diffracted beam is mounted on the θ-circle of the goniometer, while the second detector measures a reference beam and is located stationary next to the experimental table.
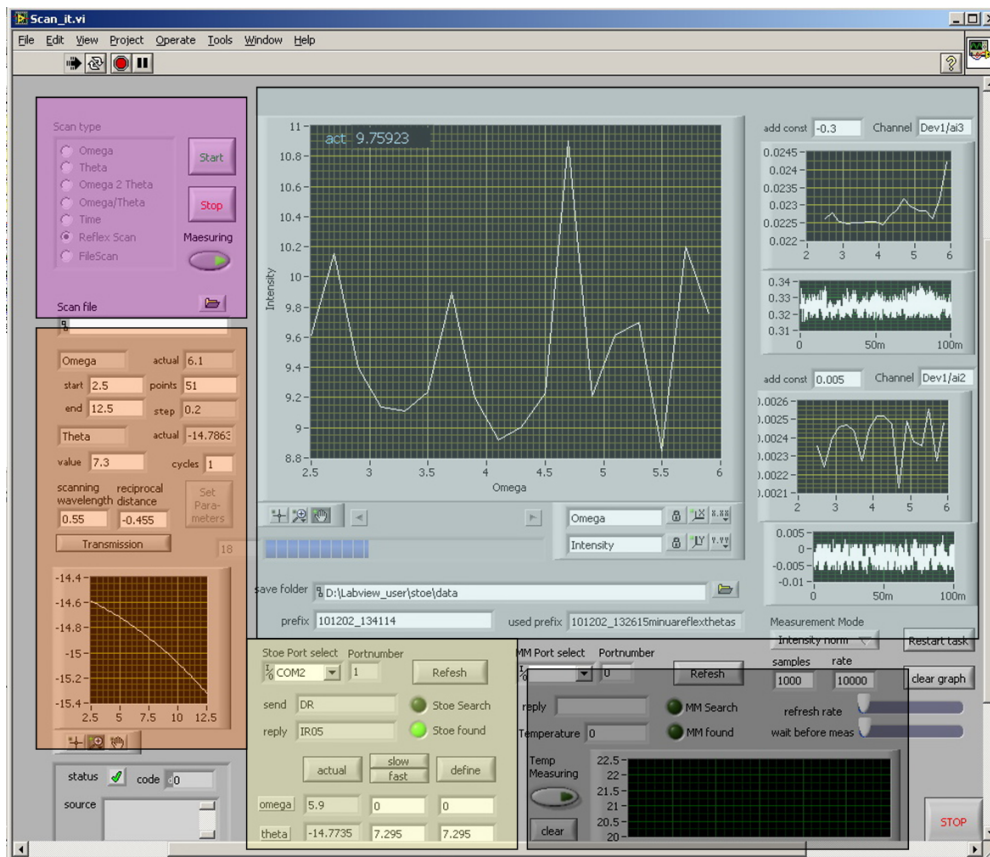

Fig. 4.2.: Screenshot of the experimental control interface. In the purple highlighted region the scan type can be chosen and the scans themselves can be started and stopped. In the orange region the scan parameters can be set. The yellow region shows the diffractometer control while the blue region shows the signals from the photodiode, the two smaller windows show diode 1 and diode 2 and the big window shows the normalized signal. Finally, the black highlighted frame shows the influence of the temperature.

5. Simulated Scattering Curves from Woodpile PCs

In order to verify the experimental diffraction curves it is either necessary to compare them with theoretical models and/or to simulate the scattering curves numerically. Thus, theoretical simulations are introduced in this chapter. The simulations of the scattering curves of the photonic crystals are based on the solution of Maxwell's equations since this will give an exact solution. However, a solution is only possible by using numerical algorithms and the precision of the solution depends on the properties of the algorithm (cf. section 2.2). There are multiple solution methods of Maxwell's equations available. Each one of them has advantages and disadvantages that depend on the specific problem at hand. In the case of the light diffraction from PCs the following boundary conditions need to be fulfilled:

- The incoming beam is not time-dependent, so the problem can be considered a stationary problem.

- The incoming beam direction should be adjustable.

- Diffraction efficiencies of specific diffraction orders should be precisely calculable.

For the interpretation of the scattering from the WP structured PCs a commercial programme was employed called *DiffractMod*[15] that relies on the solution of Maxwell's equations in the frequency domain. The programme is based on a solution method that will be described in detail in 5.1. In 5.2 the simulation parameters will be formulated and in 5.3 the simulated scattering curves will be analysed basing on the modelled parameters like e.g. refractive index dependence. Finally, conclusions will be drawn in 5.4.

The photonic phase lattices will not be addressed in this chapter. The solution method for this case differs from the WP PCs. An algorithm for simulating the scattering curves of the phase lattices was developed in [15].

---

[15]http://www.rsoftdesign.com/

5.1. Simulation method

The commercially available programme *DiffractMod* has been used for simulating light diffraction from WP structured PCs. The algorithm used by this programme is based on the rigorous coupled-wave analysis (RCWA) method in combination with modal transmission line theory which is used for a numerically more stable implementation of the boundary-value problem [50], [57], [58], [59].

The RCWA and the modal approach are both rigorous methods that solve Maxwell's equations without approximations. It can be shown that both approaches are equivalent. The difference between them is the choice of electromagnetic field representation inside the structure.

The RCW equations are derived by expanding the field into space harmonics. These space harmonics inside the crystal represent the diffracted beam orders outside the crystal.

When calculating a numerical solution one has to terminate the infinite series of space harmonics at a certain point, so the accuracy of the solution is proportional to the number of harmonics one uses [60]. A higher number also means higher calculation time. The WP PCs can be subdivided into a set of so-called layers. These layers are defined by a region where the later defined z-component of the refractive index distribution is constant. So these layers then only have a 2D modulation of the refractive index in the $x - y$-plane. The idea of this approach is that one can solve Maxwell's equations for the electric and magnetic field for each layer, where one just has to take into account the fact that the fields have to behave continuously at the interfaces of the layers.

In order to get good numerical results the layers should not be thicker than $c/4$ because the height of the layer has to be smaller than half the height of the smallest resolvable unit. Furthermore, due to the limited size in z-direction Bloch's theorem cannot be employed for this direction, but just for the $x - y$-plane. That is why the field components in a periodic layer can be written as

$$E_j(x,y,z) = e^{i\,(x\cdot k_{o\,x} + y\cdot k_{o\,y})} \sum_{p,q} e^{i\left(\frac{2\pi}{\Lambda_x}px + \frac{2\pi}{\Lambda_y}qy\right)} \sum_m a_{j\,p\,q\,m} \cdot \left(f_m \cdot e^{i\,\kappa_m\cdot z} + g_m \cdot e^{-i\,\kappa_m\cdot z}\right)$$

$$H_j(x,y,z) = e^{i\,(x\cdot k_{o\,x} + y\cdot k_{o\,y})} \sum_{p,q} e^{i\left(\frac{2\pi}{\Lambda_x}px + \frac{2\pi}{\Lambda_y}qy\right)} \sum_m b_{j\,p\,q\,m} \cdot \left(f_m \cdot e^{i\,\kappa_m\cdot z} - g_m \cdot e^{-i\,\kappa_m\cdot z}\right) \qquad (5.1)$$

with $j = x,\ y$ [50].

In the approach from (5.1) the exponent of the first e-function is the result of Bloch's theorem. For the physical understanding in terms of the reciprocal lattice it can also be written as $\mathbf{G}_{\parallel} \cdot \mathbf{r} = \frac{2\pi}{\Lambda_x}px + \frac{2\pi}{\Lambda_y}qy$. The second part is the expansion in terms of space

harmonics.

The algorithm works in such a way that the equations (5.1) are inserted into Maxwell's equations. In the case of a 2D reduction the field components E_z and H_z are already determined by the x, y-components. So one has for each layer four resulting equations. The process of solving the equations is then reduced to an eigenvalue problem with a matrix composed of differential operators (5.2), in contrast to the algebraic eigenvalue problem described in 2.1.1.

$$\underline{\underline{A}}\mathbf{x} = \lambda\mathbf{x} \tag{5.2}$$

The eigenvalues of interest λ are the square of the propagation parameters κ_m and the eigenvectors $\mathbf{x}$ are related to the a_{jpqm} and b_{jpqm}. The matrix $\underline{\underline{A}}$ is set together from the differential operators resulting from Maxwell's equations.

After having received the eigenvectors and eigenvalues, a solution of the fields in one layer has been obtained, the next step is to solve the boundary problem at the interfaces of the layers of the simulation grid. For this purpose the programme uses the so-called modal transmission-line treatment [61]. This treatment relates the coefficients $f_m^{(j)}$, $g_m^{(j)}$ of the (j)-th layer with the coefficients $f_m^{(j+1)}$, $g_m^{(j+1)}$ from the $(j+1)$-th layer. In the final step the external fields have to be matched with the fields inside the crystal.

The advantage of this representation is that the $f_m^{(j)}$, $g_m^{(j)}$ completely describe the field propagation inside the crystal and by using the modal transmission-line theory one gets the scattering efficiency of each diffraction order separately by just taking the absolute square of the corresponding Fourier coefficients.

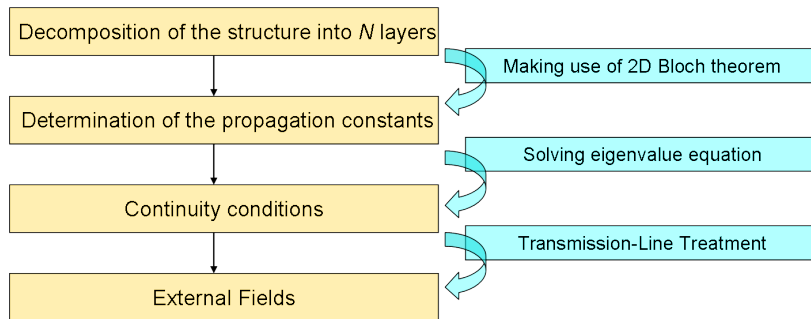In short the whole algorithm is depicted in a flow chart in figure 5.1.

Fig. 5.1.: Flow chart of the algorithm of the simulation.

5.2. Simulation parameters

Apart from the algorithm described above, the simulation requires the implementation of the crystal structure. This can be done using a CAD interface. A screenshot of the CAD interface with a model of the implemented WP PC is visible in figure 5.2.

There are numerous parameters that can be adjusted. In the following there is a short summary of the parameters that are specifically varied. Some of these parameters are dependent on crystal structure others on the simulation algorithm.

- The *refractive index* of the voids between the WP PC rods. This is one of the central problems to solve.

- The maximum number of *space harmonics* (N_x, N_y) used for calculating the scattering efficiency.

- The investigated *diffraction order* in 2D Miller indices (h, k).

Other parameters like the change in width or height of the WP rods as well as the lattice constant are not specifically investigated, the model tries to match the experimentally available structure as good as possible. Furthermore, the direction of the incident wave vector is freely adjustable with the restriction of using only plane waves.
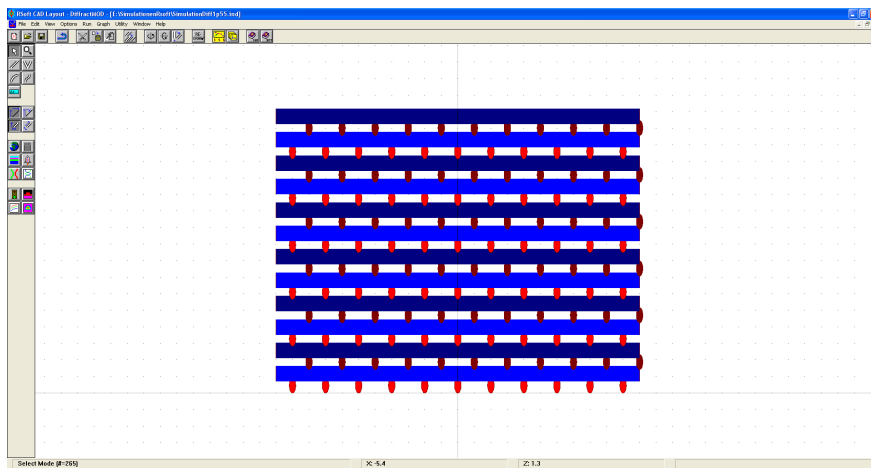

Fig. 5.2.: Screenshot of the CAD interface of the simulation programme. Visible is the $x - z$-plane and a model of the implemented WP structured PC.

5.3. Results

From the theoretical point of view a PC with low dielectric contrast should give a diffraction curve that corresponds well with a Laue diffraction curve known from the kinematic

scattering theory with a pronounced Bragg peak. For comparison with the experiment all parameters have been chosen in such a way that they match the experimental conditions. Nonetheless, some parts cannot be modelled exactly like in the experiment, e.g. the incident wave has to be modelled as a plane wave. As long as not mentioned otherwise, the wavelength was chosen to be 488nm corresponding to the experimental wavelength which was mostly used. Two different lattice constants which were given by $a = 1\mu m$ and $a = 0.9\mu m$ were chosen. The out-of-plane component is given by $c = \sqrt{2}a$.

After implementing the structure in the CAD interface, the numerical stability of the programme should be tested. For this several parameters can be varied like size of the simulation grid, number of steps and the number of Fourier components to be taken into account. After the optimum parameters were found they were used throughout the simulations, except for the number of Fourier components. The required number strongly depends on the refractive index contrast and was therefore adjusted in each case separately. An example of the simulated scattering curves of a WP PC with low RI contrast ($\Delta n = 0.02$) is shown in figure 5.3 where scattering curves of the $(02)T$ reflection are depicted calculated for three different wavelengths. From the three scattering curves it is evident that the Bragg peak moves for higher wavelengths to larger diffraction angles following Bragg's law.
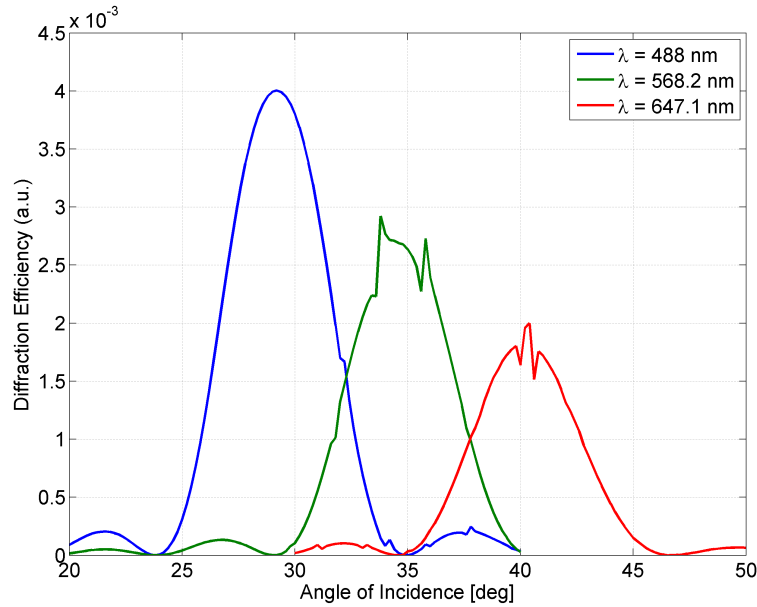

Fig. 5.3.: Scattering curves for different wavelengths. The scattering curves simulated for 'green' and 'red' light show a functional behaviour which is in some points not continuously differentiable. Those points represent numerical artifacts and can be omitted if they are few in number.

For the WP PCs the investigation was limited to the four first-order (i.e. (01) and symmetric) and four second-order (i.e. (02) and symmetric) diffracted beams in transmission (T)

geometry. Higher order reflections are not available at the used wavelength-lattice constant ratio. The mixed-order reflections, e.g. $(11)T$, have been omitted as well. An indexing of the reflections in the scattering pattern has already been depicted in figure 3.1(c). In the following sections the $(01)T$ and $(02)T$ reflections are investigated as a function of changing refractive index contrast via simulations. Moreover, they are compared to and classified with the earlier introduced kinematic approximation (cf. section 2.3). Unlike the $(02)T$ reflection there is no distinct Bragg peak for the scattering curves of the $(01)T$ reflection (cf. figure 5.4).

5.3.1. Comparison of low contrast simulations with kinematic approximation curves

In order to cross-check the numerical simulations, they are compared to the analytical kinematic theory that is valid for very low RI contrast. In figure 5.4 such a comparison of a simulation of low RI contrast ($\Delta n = 0.02$) with a kinematic scattering curve of the $(01)T$ reflection is shown. The analytic formula describing the kinematic curve is given by (5.3) with parameters $N_c = 6$ (number of repetitive elements in z-direction) and $I_0 \propto 1/30$ where the reciprocal lattice coordinate $l(\omega)$ can be expressed by the incident angle ω with the help of (3.6).

$$
I^{(0,1)T}(l) = I_0 \left(\frac{\sin\left(N_c \, \pi \cdot l\right)}{N_c \, \sin\left(\pi \cdot l\right)} \cdot \cos\left(\frac{\pi}{2} \cdot (l+1)\right) \right)^2
\tag{5.3}
$$

A detailed explanation of the used parameters will be given in the section after next. The two curves plotted in figure 5.4 indicate a good agreement between the simulation and the kinematic approximation. Several points in the simulation seem to be affected by instabilities in the numerical implementation, they can be identified in the scattering curve at the position where the curve is not continuously differentiable. As long as these points are few in number they can be easily omitted. A technical aspect is the maximum order of Fourier components. If not explicitly stated otherwise the standard order is three in each dimension, i.e. $3x3$ means $N_x = 3$ and $N_y = 3$. The number of used space harmonics can be calculated by $M_{x/y} = 2N_{x/y} + 1$ respectively.

Since the simulation and the kinematic curve coincide still very well for an RI contrast of $\Delta n = 0.02$ the question arises about the validity of this agreement for higher contrasts. This investigation is done in the next section.
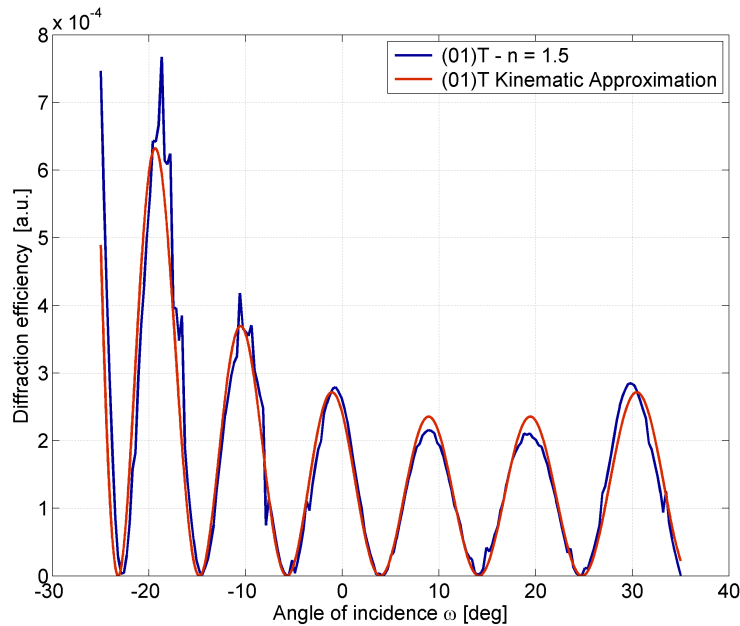
Fig. 5.4.: Comparison of kinematic approximation with a simulation of low RI contrast ($\Delta n =$ 0.02).

5.3.2. Refractive index dependent scattering curves

Selected scattering curves for the $(01)T$ reflection have been compiled in figure 5.5. As already discussed in the previous section the low contrast curve for $n = 1.5$ shows a typical kinematic scattering curve. In contrast to diffraction curves of a higher RI contrast, it is qualitatively directly visible that the diffraction efficiency increases up to a certain point with increasing contrast. At this point the diffraction curves do not increase in intensity anymore, but change their 'kinematic' structure.

For a better overview several scattering curves have been combined into three groups of scattering regimes. Since the transition in steps of $\Delta n = 0.01$ is rather smooth there have been some basic features of the curves that make a distinction into certain categories possible. The main feature is the correspondence of the scattering curves with the kinematic approximation, this means, especially for the $(01)T$ reflection, the location of maxima and minima. The curves have been compiled in figure 5.6. In figure 5.6(a) simulations of the $(01)T$ reflections in the 'weak' scattering regime are shown while in figure 5.6(b) the curves exhibit for a lower RI contrast at $n = 1.39$ still a quasi-kinematic structure, but for increasing contrast the peak shape deforms and additional peaks are appearing, that is why this regime is named a regime of transition. In figure 5.6(c) the scattering curves with a contrast larger than $\Delta n = 0.25$ are depicted. They exhibit a structure that has a more complex form.

A similar decomposition into scattering regimes can be made for the $(02)T$ reflection as
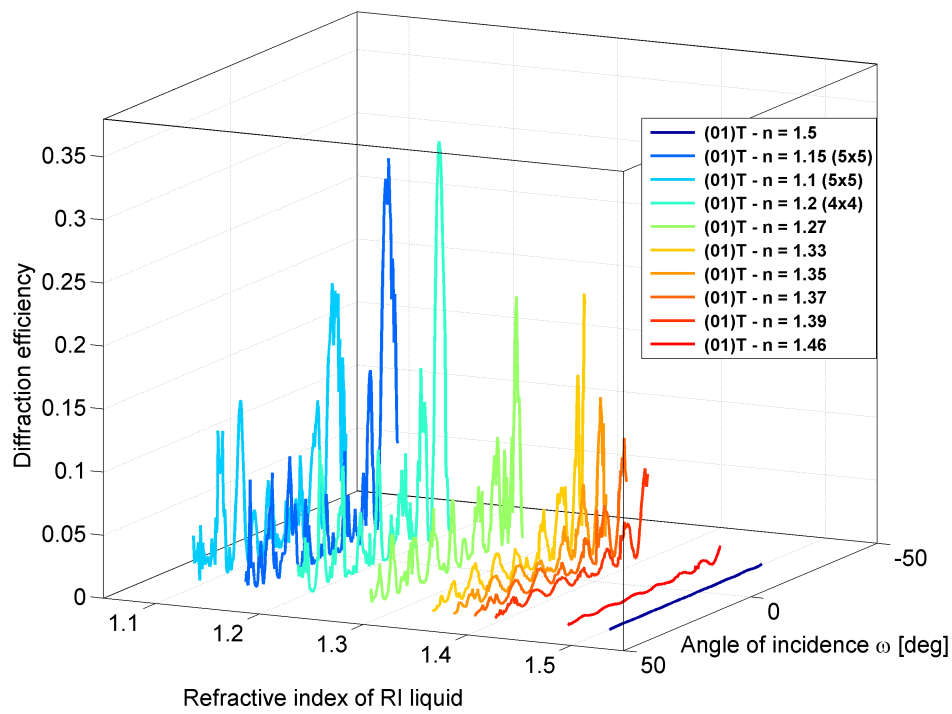
Fig. 5.5.: Compilation of scattering curves of the $(01)T$ reflection with different RI contrast ($\Delta n = 0.02...0.42$). In several cases the number of the maximum space harmonics for each dimension is given in brackets. If this is not the case it is given by $3x3$.
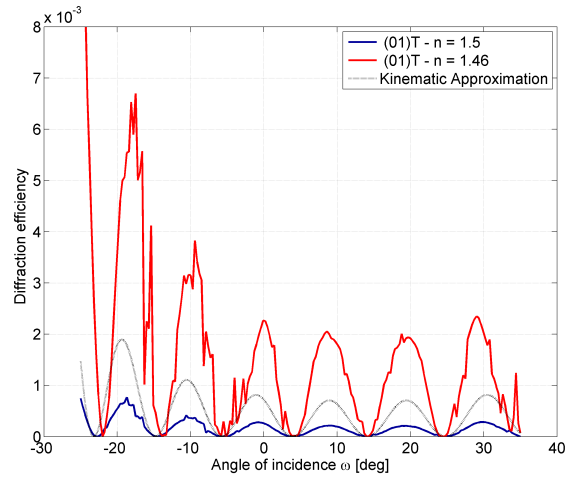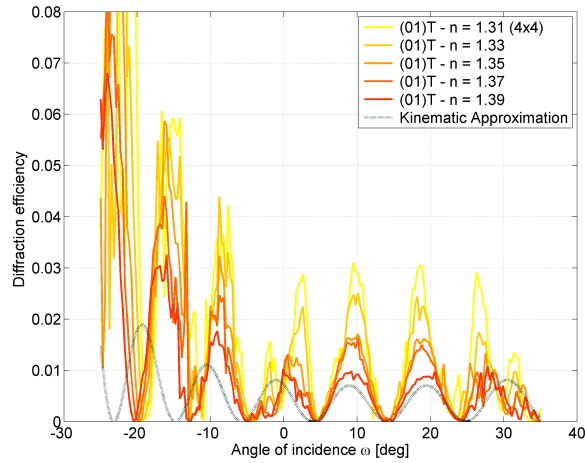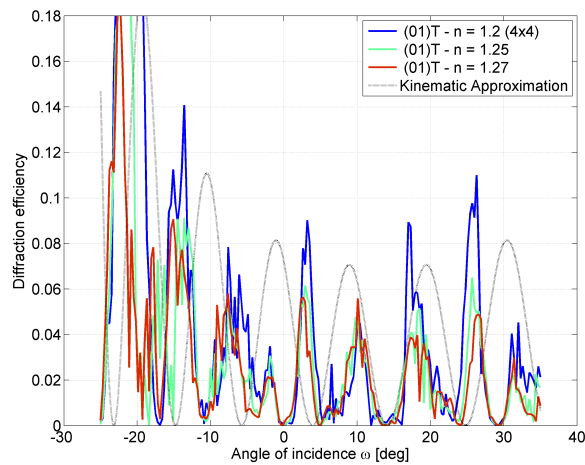
(a) RI regime $\Delta n = 0.02...0.06$

(b) RI regime $\Delta n = 0.13...0.21$

(c) RI regime $\Delta n = 0.25...0.32$

Fig. 5.6.: Selected scattering curves of the $(01)T$ reflection in different RI contrast regimes. In several cases the number of the maximum space harmonics for each dimension is given in brackets. If this is not the case it is given by $3x3$.

well. At first sight the scattering regimes do not match for both reflections. In figure 5.7 a compilation from selected scattering curves of the $(02)T$ reflection is shown. Here, the scattering curves for low contrast correspond again to the kinematic approximation which is characterized by the typical Bragg peak with side fringes for this reflection.
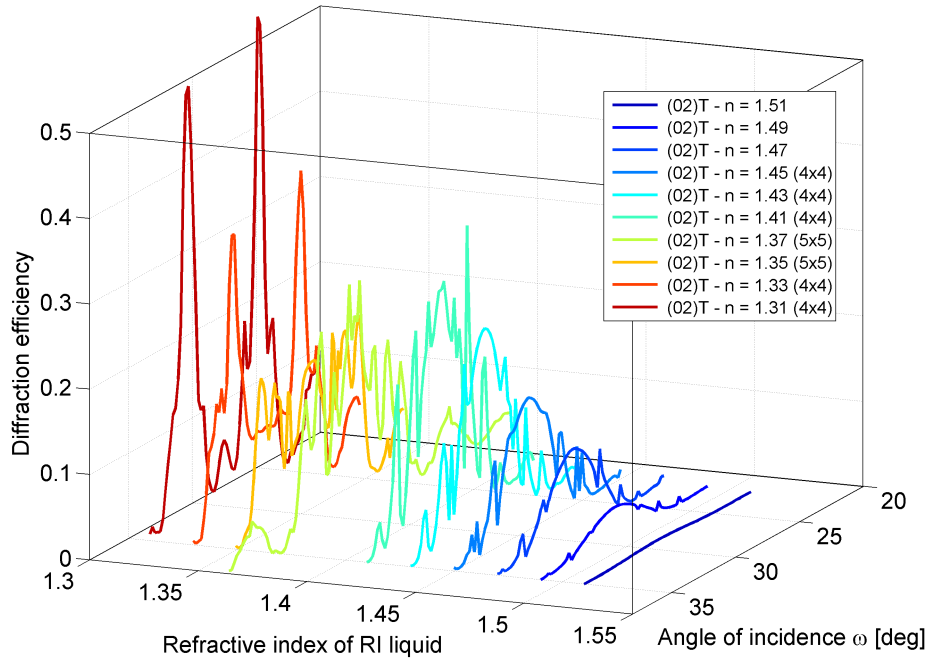

Fig. 5.7.: Compilation of scattering curves of the $(02)T$ reflection with different RI contrast ($\Delta n = 0.01...0.21$). In several cases the number of the maximum Fourier order for each dimension is given in brackets. If this is not the case it is given by $3x3$.

5.3.3. Classification of RI dependent scattering curves

Introduction of the fitted kinematic model

The numerical simulations can be quantitatively compared to the kinematic approximation. This is done by fitting a kinematic model to the simulated data. Equation (5.4) is used as a model.

$$I^{(h,k)T}(l) = I_0 \left(\frac{\sin\left(N_c\, B\, \pi \cdot (l - l_0)\right)}{N_c \sin\left(B\, \pi \cdot (l - l_0)\right)} \cdot \cos\left(\frac{\pi}{2}(h + k) + \frac{\pi}{2} \cdot B\, (l - l_0)\right) \right)^2 \qquad (5.4)$$

This model is based on three parts which are

1. the structure factor,

2. the form factor of a single scattering element and

3. the lattice sum.

The first one considers the phase-correct summation of the elements located in the unit cell and is in the model accounted for by

$$\left(\cos\left(\frac{\pi}{2}(h+k) + \frac{\pi}{2} \cdot B\left(l - l_0\right)\right)\right)^2.$$

The structure factor is the only difference between the considered reflections ($(01)T$ and $(02)T$) and it is also the reason for the different functional behaviour of the scattering curves, i.e. the $(02)T$ reflection has a Bragg peak because the theoretical value of the structure factor $\left(\cos\left(\pi + \frac{\pi}{2} \cdot l\right)\right)^2$ is one for $l \to 0$ while in contrast to the $hkl = 020$ reflection the $(01)T$ or (010) reflection has no Bragg peak for $l \to 0$. The form factor of the single scattering element is approximated by unity. The third term is considered by the well-known Laue function:

$$\left(\frac{\sin\left(N_c \, B \, \pi \cdot \left(l - l_0\right)\right)}{N_c \, \sin\left(B \, \pi \cdot \left(l - l_0\right)\right)}\right)^2$$

Before fitting the model, the simulated data is transferred to reciprocal space by the transfer function derived in (3.8). The fitted parameters correspond to the following physical values. I_0 accounts for the diffraction efficiency while B is a measure of the c-value of the PC. This parameter should be negligible for the simulations, especially in the low-contrast regime. The reason for the introduction of this parameter lies in the comparibility to the experimental part of the work. There, it will become clear that the c-value of the PC can be influenced by the mechanical stability of the photo resist. The l_0 parameter's introduction is also due to the experiment. It accounts for the validity of the Bragg condition. Experimentally, deviations of this parameter might explain a misalignment of the PC. In order to make a statement about the goodness of the fit, the adjusted R^2 value is calculated and given for each fit. The R^2 statistic measures how successful the fit is in explaining the variation of the data [62]. In other words, R^2 is the square of the correlation between the response values and the predicted response values. It is defined as:

$$R^2 = 1 - \frac{\text{sum of squares due to error}}{\text{total sum of squares}} \tag{5.5}$$

R^2 can have any value between 0 and 1. For a value of $R^2 = 1$ the fit accounts for all the variations in the data. For a value of 0.5 the fit explains 50 per cent of the variation of the data by the model. The degrees of freedom adjusted R^2 value takes also into account the

number of parameters used for the model. That is why it is used in this case.

Comparison of the simulated data with the kinematic model

A preliminary basic distinction into the three different regimes has been made in the last section due to an eyeball comparison of the scattering curves. In this section a mathematical approach is used by fitting the curves with a kinematic model. The fit parameters are determined and given for two different reflections in table 5.1 and table 5.2. The used analytical model to fit the simulations is given by:

$$I^{(0,k)T}(l) = I_0 \left(\frac{\sin\left(N_c\, B\, \pi \cdot (l - l_0) \right)}{N_c \sin\left(B\, \pi \cdot (l - l_0) \right)} \cdot \cos\left(\frac{\pi}{2} \cdot k + \frac{\pi}{2} \cdot B\,(l - l_0) \right) \right)^2 \qquad (5.6)$$

with $N_c = 6$ (number of repetitive elements in z-direction) and $k \in \{1, 2\}$ while the fit parameters are given by I_0, B and l_0. For each fit the adjusted R^2 value (cf. [63]) was evaluated as a measure for the goodness of the fit. In this context one can use the adjusted R^2 value as a feature to distinguish different scattering regimes. Based on the values given in table 5.1 the following distinction is made:

- **Kinematic approximation regime** $\Delta n = 0 - 0.12$

- **Regime of transition** $\Delta n = 0.13 - 0.21$

- **Strong scattering potential regime** $\Delta n = 0.22 - 0.52$

The distinction above is based on the analysis of the $(01)T$ reflection. Several selected fits have been plotted in figure 5.8 in order to visualize the transition. While for the $(01)T$ reflection the results indicated a transition that takes place at a RI difference in the region of $\Delta n = 0.13 - 0.21$ the results of the $(02)T$ reflection show an earlier transition to a non-kinematic scattering behaviour according to the fits. This can be seen by comparing the adjusted R^2 values. It even becomes clearer by taking a look at the plots of the corresponding fits in figure 5.9. The main Bragg peak changes its structure when the RI contrast is increased from a smooth Gaussian-like function to a fragmented-looking function.

There are several facts that need to be kept in mind while taking a look at the simulation of the $(02)T$ reflection. Firstly, for low contrast the intensity of the reflection curve is at a maximum if the Bragg condition is fulfilled. This means that in this case the constructive interference of the scattered beams is at a maximum. Previous numerical calculations of scattering from WP PCs [11] have already revealed that for an increasing RI contrast the simulation grid in out-of-plane (z) direction has to be chosen at a minimum of one tenth

(a) $n = 1.46$

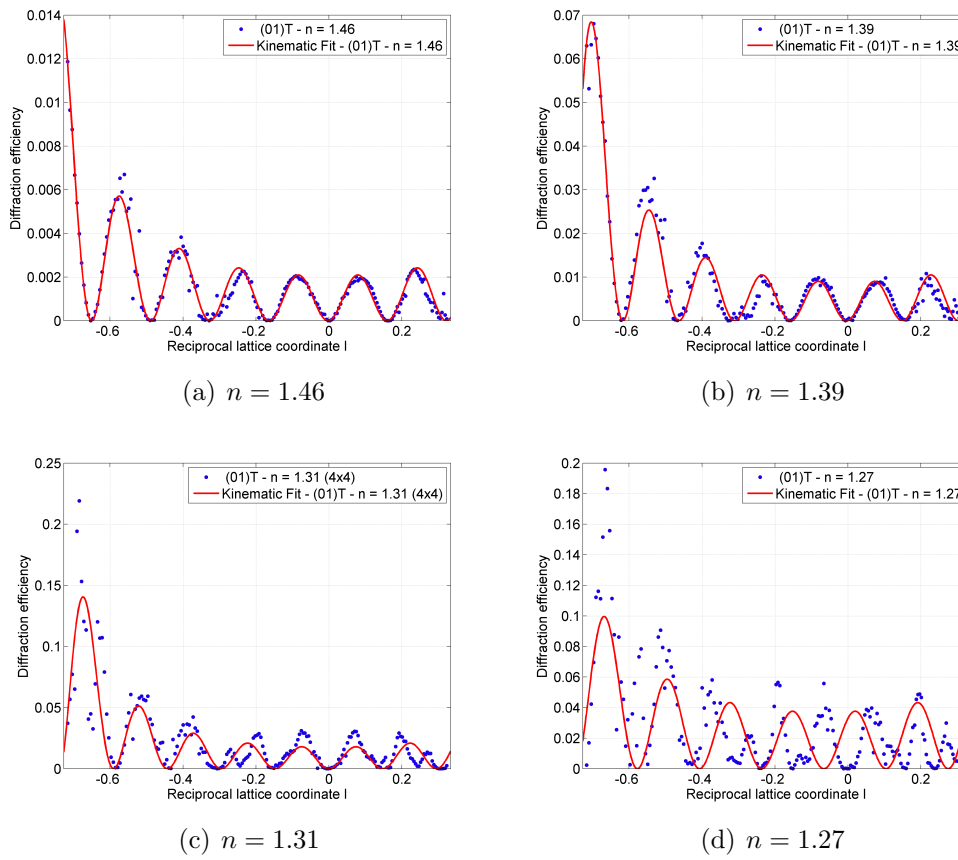(b) $n = 1.39$

(c) $n = 1.31$

(d) $n = 1.27$

Fig. 5.8.: Selected fits of the kinematic approximation to the simulations. Blue dots indicate simulated data while the red curve stands for the fitted values. The reflection $(01)T$ was considered.

RI Liq. (N_x x N_y)	B	ΔB	I_0	ΔI_0	l_0	Δl_0	R^2
n = 1.1 (5x5)	1.04	0.01	9.64	0.83	-0.057	0.005	0.46
n = 1.15	0.83	0.02	8.42	1.43	-0.123	0.009	0.16
n = 1.15 (4x4)	1.01	0.01	11.01	1.11	-0.053	0.006	0.5
n = 1.15 (5x5)	1.01	0.02	10.71	1.1	-0.055	0.006	0.5
n = 1.17	0.68	0.02	5.79	0.9	-0.002	0.012	0.22
n = 1.2	0.67	0.02	5.22	0.83	-0.002	0.012	0.2
n = 1.2 (4x4)	0.67	0.02	5.18	0.86	-0.006	0.013	0.17
n = 1.25	0.99	0.01	6.64	0.66	-0.061	0.006	0.49
n = 1.27	0.98	0.02	5.09	0.55	-0.066	0.006	0.37
n = 1.31	1.13	0.02	3.3	0.27	-0.001	0.009	0.66
n = 1.31 (4x4)	1.13	0.02	3.24	0.25	0	0.009	0.68
n = 1.33	1.09	0.02	2.78	0.26	0.008	0.012	0.58
n = 1.35	1.14	0.01	2.38	0.11	-0.007	0.005	0.87
n = 1.37	1.11	0.01	1.86	0.07	-0.004	0.005	0.89
n = 1.39	1.09	0.01	1.51	0.04	-0.004	0.003	0.95
n = 1.46	1.03	0.01	0.31	0.01	-0.002	0.002	0.94
n = 1.5	1	0	0.03	0	-0.001	0.001	0.98

Tab. 5.1.: Fit parameters of the kinematic model for the respective RI contrast simulations of the $(01)T$ reflection. The last column shows the adjusted R^2 value indicating the validity of the model.

of a rod thickness. Additionally, the in-plane parametrization requires a higher number of Fourier coefficients for modelling the electromagnetic field. This necessity is due to the fact that a convergence of the solution of the scattering matrices needs to be achieved. However, a higher number of Fourier coefficients means that the number of transmitted $f_m^{(j)}$ and reflected waves $g_m^{(j)}$ at each layer (j) will increase considerably. This results in a higher calculation time.

Aside from the mentioned increased numerical effort, the implemented algorithm of the simulation programme has some obstacles that cannot be overcome. These obstacles result in divergences in the simulated scattering signal at arbitrary scattering angles which seem to get more numerous at a higher RI contrast. While for lower contrast those inconsistencies can be easily identified and omitted this is not possible for a higher contrast. Obviously, these divergences are directly correlated to the degree of strength of coupling of the different Fourier coefficients in the RCWA approach that

1. depend on the RI contrast,

2. depend on the angle of incidence of the incoming beam.

Both points in the upper enumeration can be summarized in the photonic band structure that directly shows the influence of both parameters. In figure 2.1(c) the effect of the splitting
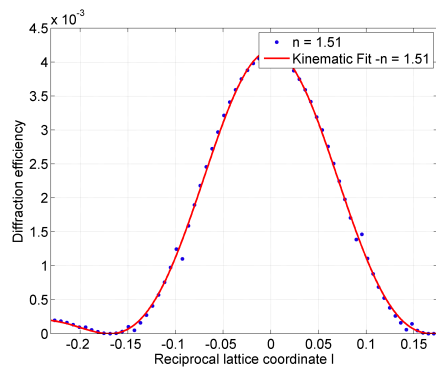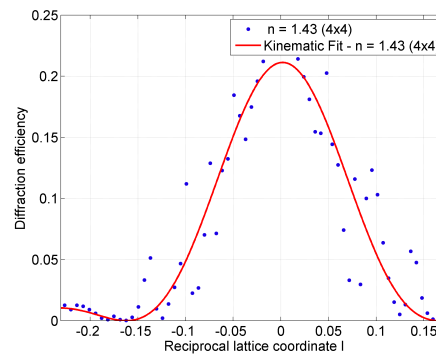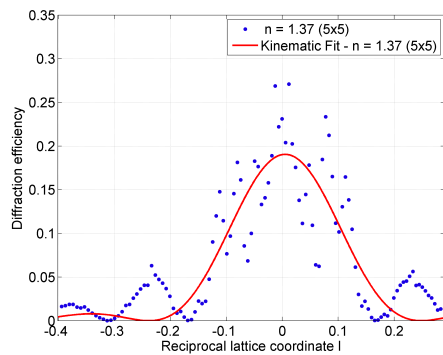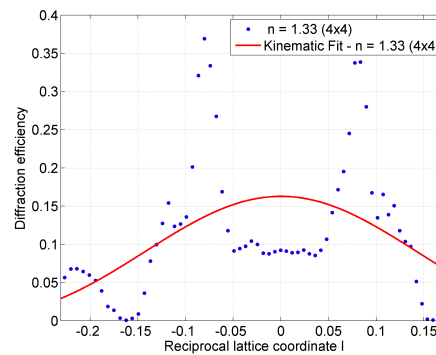
(a) $n = 1.51$

(b) $n = 1.43$

(c) $n = 1.37$

(d) $n = 1.33$

Fig. 5.9.: Selected fits of the kinematic approximation to the simulations. Blue dots indicate simulated data while the red curve stands for the fitted values. The reflection $(02)T$ was considered.

of a photonic band structure by increasing contrast was already demonstrated, as well as the dependence of the splitting in k-space.

RI Liq. (N_x x N_y)	B	ΔB	I_0	ΔI_0	l_0	Δl_0	R^2
n = 1.51	0.98	0	0	0	0	0.001	1
n = 1.49	1.02	0.03	0.04	0	0	0.002	0.97
n = 1.47	1.05	0.05	0.1	0.01	-0.003	0.003	0.96
n = 1.45 (4x4)	0.99	0.07	0.15	0.01	-0.002	0.004	0.91
n = 1.45	0.97	0.07	0.15	0.01	-0.003	0.004	0.9
n = 1.43 (4x4)	1.02	0.08	0.21	0.01	0.002	0.005	0.89
n = 1.41 (4x4)	0.91	0.1	0.25	0.03	-0.001	0.008	0.77
n = 1.39 (4x4)	0.84	0.1	0.24	0.02	0.001	0.009	0.74
n = 1.37 (5x5)	0.68	0.06	0.19	0.02	0.005	0.009	0.72
n = 1.37 (4x4)	0.69	0.09	0.19	0.02	0.004	0.011	0.66
n = 1.35 (5x5)	0.55	0.08	0.16	0.02	-0.006	0.014	0.48
n = 1.35 (4x4)	0.55	0.1	0.16	0.02	-0.007	0.016	0.47
n = 1.33 (4x4)	-0.47	0.15	0.16	0.03	0	0.033	0.19
n = 1.33	-0.46	0.17	0.16	0.03	0	0.036	0.16
n = 1.31 (4x4)	0.42	0.26	0.18	0.06	0	0.06	0.05
n = 1.01 (4x4)	-0.27	0.2	0.07	0.01	0.077	0.114	0.14

Tab. 5.2.: Fit parameters of the kinematic model for the respective RI contrast simulations of the $(02)T$ reflection. The last column shows the adjusted R^2 value indicating the validity of the model.

5.4. Conclusions

In this section the pure numerical solutions of the scattering from WP structured PCs were investigated. From these investigations several conclusions can be drawn:

- For low RI contrast ($\Delta n < 0.05$) the numerical simulations can be approximated very well by kinematic theory.

- A stepwise increase of the RI contrast leads to an increase in the scattering efficiency while the form of the scattering curves do not change.

- A regime of transition has been found where a raise of the RI contrast does not increase the scattering efficiency anymore but instead the form of the scattering curves is affected.

- The used numerical algorithm is strongly affected by the degree of coupling of the Fourier coefficients, e.g. the scattering curves of reflections with a larger coupling like the $(02)T$ reflection are more influenced by divergences.

In the next chapter the numerical simulations will be used for a comparison with the experimental findings.

6. Woodpile Photonic Crystals

The influence of the change of the refractive index (RI) difference in the RI distribution of woodpile-structured photonic crystals (WP PCs) is analysed in this section. The RI difference varies from $\Delta n \approx 0.52$ to $\Delta n \approx 0.005$. A change of the RI difference can be achieved by infiltrating optical liquids into the voids of the crystal. The influence of this change will affect the diffraction curves.

The investigation of light scattering from WP PCs in a form comparable to the one presented in this thesis has been initiated by [11]. This work featured colloidal PCs and WP PCs inscribed into SU-8 polymer. The light scattering was investigated under the aspect of figuring out the influence of the refractive index contrast. However, only three cases have been investigated. These three cases led to a subclassification of the scattering.

First a dynamical scattering regime was defined which concerns the case where the crystals have no liquid filling and therefore a high contrast of $\Delta n \approx 0.6$. This regime is characterized by scattering curves with no distinct Bragg peak. Then a so-called kinematic scattering regime was defined. This concerns crystals with a low refractive contrast of $\Delta n \approx 0.005$. The small RI variation was achieved by leaving out the chemical post-processing which is usually done for removing the non-illuminated parts of the photo resist.

The terms 'dynamical' and 'kinematical' have been chosen due to their usage in scattering theory known from X-ray diffraction. In the latter case it has been shown that the obtained scattering curves can be modelled by a simple kinematical diffraction model which assumes a weak scattering potential and subsequently results in the assumption of single scattering, so the term kinematic is a rather good choice. In the dynamical regime weak scattering can no longer be assumed because of the high RI contrast $\Delta n \approx 0.6$. In this case one has to take into account multiple-scattering of the photons. However, the choice of the term dynamical in this context does not correspond well to the X-ray case and should not be confused with it.

The third case dealt with a PC that has been infiltrated with glycerol as an optical liquid. The refractive index of glycerol is given by $n = 1.4735$ (cf. figure 6.1). The resulting diffraction curves for this Δn showed a clear Bragg peak but also some deviations, e.g. peak broadening, from the kinematic approximation. So the scattering regime of crystals with such kind of refractive index difference was called intermediate regime and located in between

the kinematic and dynamic regime.

In this work a subdivision into different scattering regimes was already made in the previous chapter. This was based on numerical calculations. In this chapter the question is therefore discussed in how far this can be achieved experimentally. Thus, it depends on the experimental results, whether the previously found distinction of the scattering regimes can or cannot be confirmed.

Another important issue of the work is also to find out the conditions for a transition from curves that show a clearly visible Bragg peak to curves that show diffraction for non-Bragg geometry. This is accomplished by infiltrating special optical RI liquids into the crystal.

The investigation does not rely on a single WP PC but on several ones to exclude sample-dependent results. Since it cannot be expected that all PCs that were available, have the same quality the following discussion of the measurements is divided in such a way that for *each sample* the experimental results are presented and discussed separately. Subsequently, the experimental analysis is done exemplary for a PC that showed the most promising result. Based on this result, a comparison with simulated data will be made. In appendix B the different RI liquid infiltration methods are discussed on the basis of a set of WP PCs made of SU8 photo resist.

6.1. Wavelength-dependent refractive index

The effect called dispersion means that the refractive index n of a material depends on the wavelength of the waves travelling inside the material. One example of dispersion is the splitting of a white beam inside a prism. In order to define the refractive index for a material a single value is not sufficient. For visible light one experimentally finds the so-called Sellmeier- or Cauchy-equation.

$$n(\lambda) = n_0 + \frac{n_1}{\lambda^2} + \frac{n_2}{\lambda^4} \tag{6.1}$$

This equation depends on the wavelength and on the three coefficients n_i. For each material one has to consider the dispersion relation. For the materials used in this thesis the corresponding dispersion curves have been plotted in figure 6.1. In this figure you can see the wavelength dependence of the refractive index in a range from 400 to 700 nm. The values for the refractive indices are often tabulated for a certain wavelength. Most refractive indices are given at the Fraunhofer 'D' line at $\lambda = 589.3 nm$. The refractive index values of the Cargille[16] liquids are given at this 'D' line. For the SU8 polymer, from which the woodpile-structured photonic crystals are made of, one has to distinguish between the crosslinked and
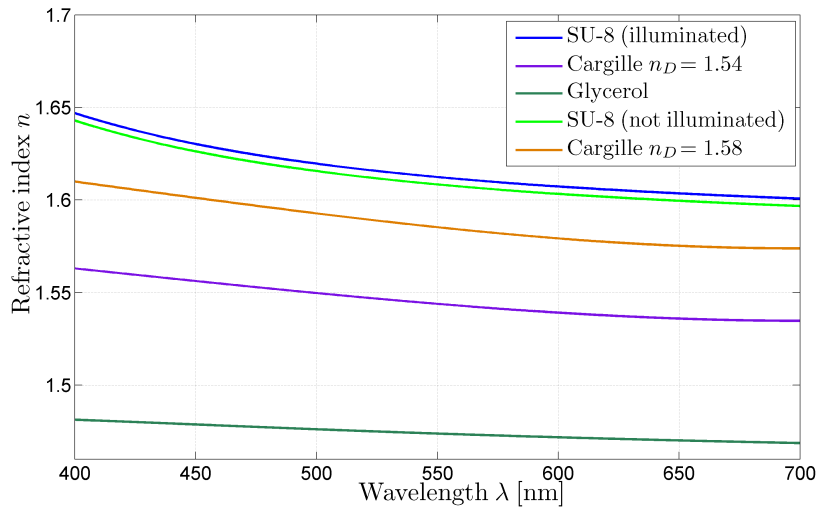
---

[16]http://www.cargille.com/opticalintro.shtml

Fig. 6.1.: Refractive index as a function of the wavelength of selected Cargille RI liquids and SU8. All values have been extracted from literature.

non-crosslinked material, although the difference is rather small. All of the plotted data in figure 6.1 have been extracted from the corresponding data sheets of the manufacturers. Unfortunately, such kind of data is not available for the IP44 photo resist.

6.2. Woodpile photonic crystals - IP44 photo resist

A set of samples of WP PCs has been investigated with lattice constants of an in-plane value of $a = 0.9\mu$m and an out-of-plane value of $c = \sqrt{2}a$. More importantly the photo resist, which the crystal is inscribed in, is a newly developed one labelled IP44. This material was developed for commercial use and therefore no information about the composition of this material has been published yet. One confirmed piece of information is that the refractive index has a value of $n_{\mathrm{IP44}} = 1.52$ at visible light.

Multiple sets of samples were investigated (cf. table 6.1). Although efforts were made to keep the lattice parameters at the same values, PBG measurements [64] already revealed that a variety of structures are of slightly different quality, e.g. sample A exhibited no PBG. Thus, it was concluded that this set of PCs was not perfectly developed.

Sample set	Purpose	Bandgap
A	Test of infiltration technique	No
B	Investigation of RI dependent scattering	Yes
C	Confirmation of scattering classification	Yes

Tab. 6.1.: Three different sample sets of the IP44 WP structured PCs.

6.2.1. Test of infiltration technique - sample set A

As previously mentioned this first set of samples was of lower quality and therefore used for testing purposes. Even with a not fully 'developed' structure, experiments have been performed in order to study the effect of infiltration and if a subsequent change in the scattering pattern can be observed.

The first impressions based on microscopic investigation as well as the visual inspection of the scattering pattern indicated that the infiltration has been performed quite successfully. In this case the infiltration was done without the use of a desiccator (cf. appendix B).

Time dependence of the infiltration

Since the PC has no cover and is mounted vertically, the RI liquid could flow out of the WP structure. Therefore, the time-dependent behaviour of the infiltration was investigated. This was done by comparing scattering curves recorded at different times. One can see in figure 6.2 that the intensity increases at first and then drops down again. Throughout this time the general shape with a distinct Bragg peak does not change. These results are quite comprehensible considering the following facts. When the sample is mounted on the goniometer a thick drop of RI liquid is still on top of the PC. Once in vertical position the drop slowly moves down along the glass substrate towards the ground. The influence on the scattering efficiency can be explained by the absorption of the light by the RI liquid. A larger drop absorbs more light than a small film. On a larger time scale the liquid distribution can be affected inside the PC. The result of small deviations of the liquid distribution can result in a partly incoherent scattering which reduces the scattering efficiency slightly.

Refractive index dependence

Although this sample set was not intended for analysing the RI dependence, this investigation was anyway done in order to check if a re-infiltration with other RI liquids is possible. Therefore, the glass substrate was cleaned after measuring the scattering curve at a certain RI contrast with Isopropyl alcohol (IPA). This was supposed to leave the polymer structure unharmed and to remove the RI liquid.

The results of the experiment show that the scattering curves change their shape after inducing a low RI contrast, so that a Bragg peak is visible. In figure 6.3 these curves are shown. A slight asymmetry in the Bragg peaks is noteable. Besides, the typical side fringes of the Bragg peak are suppressed which means they have a lower intensity than expected. These two facts are possibly due to the already mentioned lower quality of the structure. Nevertheless, the infiltration procedure seems to be working. In the same figure, for com-
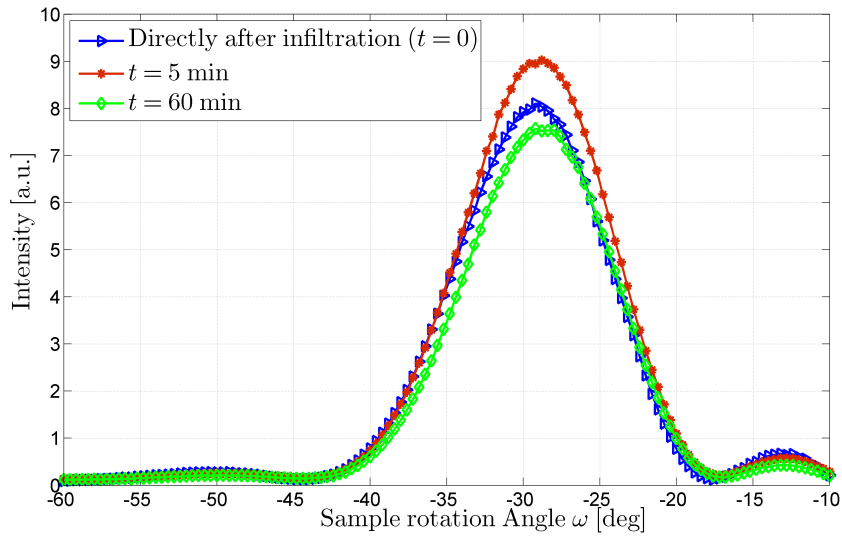
Fig. 6.2.: Effect of the time dependence of the infiltration on the scattering curve. Exemplary shown is the (02) reflection in transmission geometry.

parison, the blue curve represents the behaviour of the scattering for the non-infiltrated PC.

In the range set by the refractive index liquids from $\Delta n \in [0.01; 0.13]$ a dependence of the scattering efficiency of the Bragg peak and the RI contrast Δn is clearly visible. This can be seen in figure 6.4. The lowest contrast given for an RI liquid of $n = 1.53$ shows the smallest scattering efficiency while the highest contrast of $\Delta n = 0.13$ for a RI liquid of refractive index $n = 1.65$ shows the highest scattering efficiency. The two contrasts in between show a similar diffraction efficiency. In both cases the relative contrast is almost the same, but in one case the RI liquid has a higher RI value as the IP44 polymer while in the other case it is vice versa. Therefore, it is noteworthy that the absolute sign of the contrast has neither an influence on peak shape nor on the diffraction efficiency. The connection between maximum diffraction efficiency and the RI contrast is graphically presented in figure 6.5. Taking just the absolute value of the RI difference and plotting it versus the maximum scattering efficiency it would indicate that a linear behaviour exists. However, for this PC one has to beware of such conclusions due to the quality of the sample. The fact should be shortly mentioned that from a theoretical point of view the dependence should be quadratic. A detailed discussion including a comparison with theory and experiment made for sample set C.

Peak shape In a previous work [11] a considerable broadening of the main Bragg peak was reported for an increase in RI contrast, though only two different RI values were compared
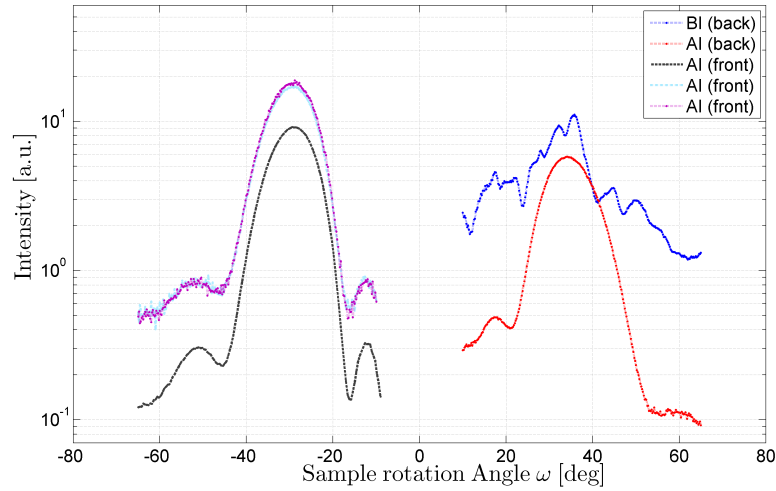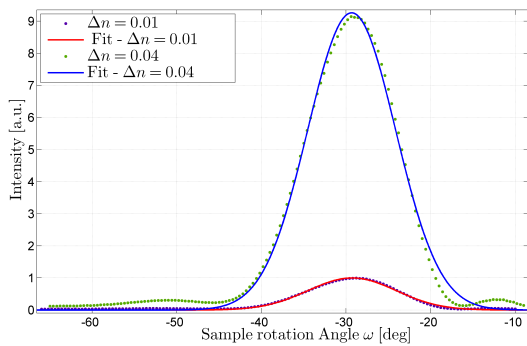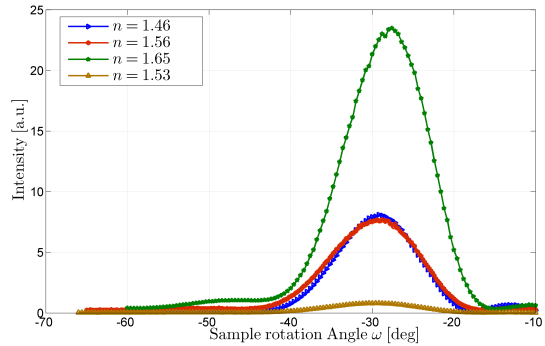
Fig. 6.3.: Comparison of different reflections. The (02) reflection is shown for different incident beam intensities as well as the $(0-2)$ reflection (red curve). For comparison the $(0-2)$ reflection without any infiltration is plotted (blue curve).
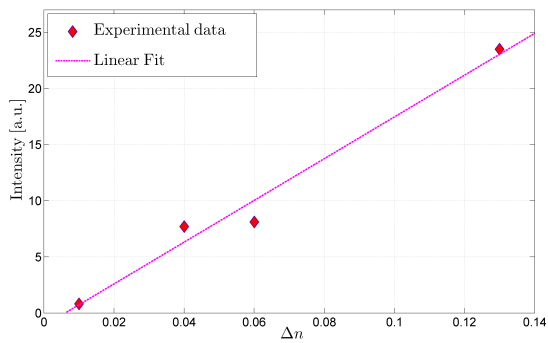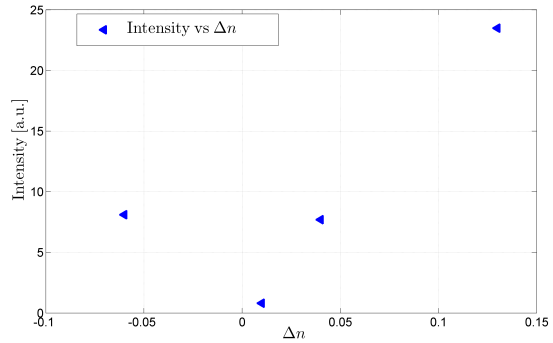

(a) $n = 1.53$ and $n = 1.56$

(b) $n \in \{1.53; 1.56; 1.65; 1.46\}$

Fig. 6.4.: Diffraction efficiency dependence on the refractive index difference.

(a) Absolute RI difference.

(b) Signed RI difference.

Fig. 6.5.: Maximum diffraction efficiency plotted versus the refractive index difference.

of which one was not due to infiltration. Thus, a systematic analysis of the width of the Bragg peaks as a function of refractive index difference was done.

The values for the standard deviations at different RI contrasts have been determined by fitting a Gaussian distribution to the scattering curve, neglecting possible side fringes. In figure 6.6 you can see the variation of the standard deviation σ or better the lack thereof. The variations can be considered to be within the experimental accuracy. Therefore, no RI dependence on peak shape in the given RI range can be concluded.
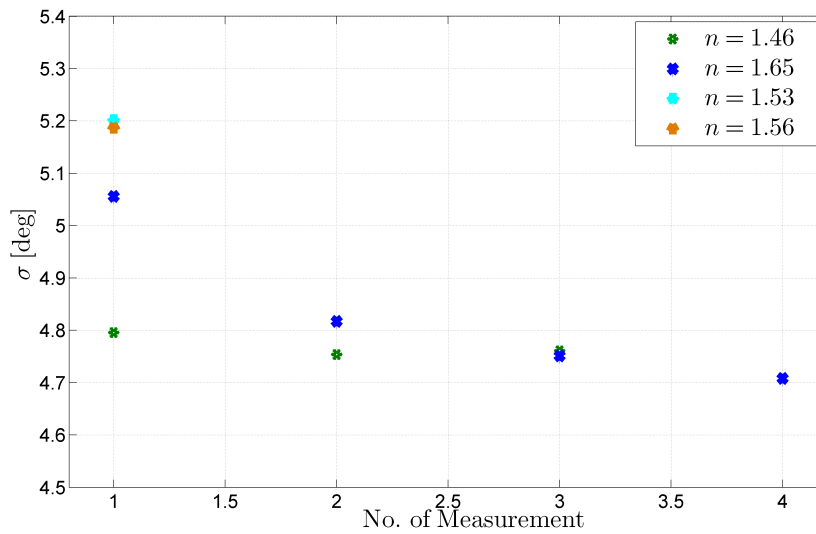
Fig. 6.6.: Peak width as a function of refractive index.

6.2.2. Investigation of RI dependent scattering - sample set B

Sample set B consists of a glass substrate where three different WP PCs made of IP 44 were inscribed. The lattice parameters were kept at the same values as in sample set A ($a = 0.9\mu$m, $c = a\sqrt{2}$). Unlike sample set A the quality of the PCs in this sample set can be considered high. An indication for this structural quality is the measurement of the transmittance spectra and the subsequent comparison with the theoretical predictions. This was done by collaborating group and according to whom this set of samples is supposed to have a high quality. Practically, this could mean that the inscribed structure resembles more the perfect woodpile crystal one would imagine from the sketch. This includes for example rods that are parallel and match a straight line. Furthermore, the rod size (width, thickness) should not vary inside the crystal as reported earlier [64]. Other optimized properties are the filling factor and polymer stability.

Reproducible measurements and infiltration technique

In order to ensure the reproducibility of the measurements and the infiltration/cleaning procedure the sample is mounted onto the goniometer stage and the infiltration/cleaning was done for this set of samples on the goniometer stage itself so that the incident conditions were always the same. This is opposite to previous investigations (cf. appendix B) were the glass substrate was removed for cleaning and infiltrating. After RI liquid infiltration the scattering curves of the two major reflections $(01)T$ and $(02)T$ were recorded. Afterwards it was cleaned with a stream of isopropyl alcohol for removing the RI liquid. The respective scattering curves were measured again after cleaning. Later on the next liquid was infiltrated and subsequently the next measurement was performed. This procedure should enhance the reproducibility and comparability of the different scattering curves at a different RI contrast and minimize the influence of irregularities like misalignment. Another advantage is that any deviation in the curves measured after removing the RI liquids can give a hint of a problem with the infiltration technique. This means that all curves should exhibit the same scattering behaviour, once the liquid is removed. In figure 6.7 the respective uninfiltrated
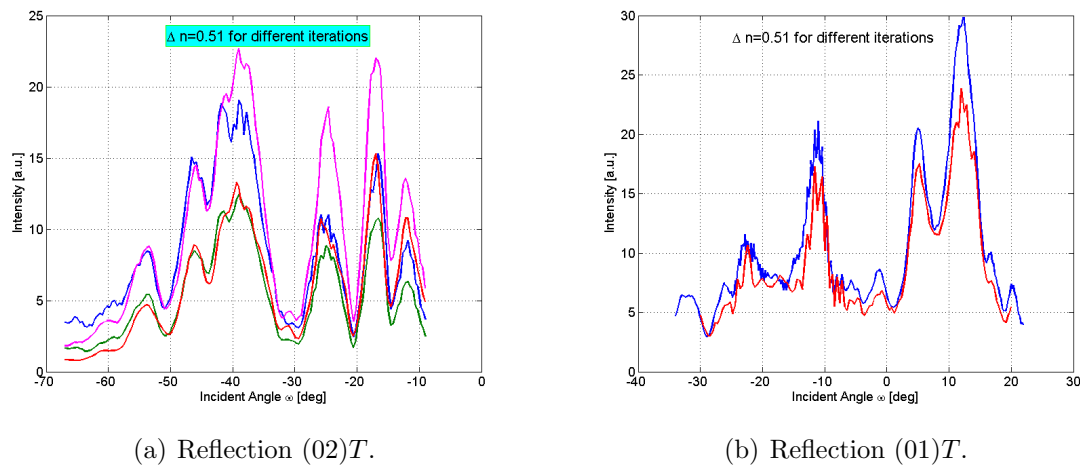

(a) Reflection $(02)T$.   (b) Reflection $(01)T$.

Fig. 6.7.: Sample $B-1$ - Prior to infiltration and after removing of the liquids.

scattering curves for the $(01)T$ and $(02)T$ reflections are shown. There are three statements that can be made after reviewing the scattering curves:

- The scattering curves do not change their angular scattering pattern.

- Shifts in the intensity can be observed.

- All scattering curves show no distinct Bragg peak as expected for a PC with a high RI contrast.

From these statements the following conclusions can be drawn. Firstly, one can conclude that the liquids can be removed completely and the initial state can be obtained. However, no statement can be made in how far this liquid is really completely filling out all spacings in between the logs of the PC. Secondly, the small changes in intensity can occur due to a possible shift of the sample in the goniometer stage when cleaning it with a weak jet of isopropyl alcohol. Although the sample is very well fixed, a small shift of a few μm can cause this kind of intensity drop, due to the limited macrosopic extension of the sample. This kind of effect has to be considered within the experimental error estimation. Nevertheless, it can be concluded that the curves indicate a good degree of reproducibility for each iteration.

Refractive index dependence

Analysing the scattering curves of the cleaned sample resulted in the proof that the sample can be fully restored into its initial state before any infiltration was done. Thus, the focus can be directed towards the RI dependent measurements. For the first sample of this set ($B-1$) the employed RI liquids had a range of approximately $\Delta n = [0.01; 0.05]$. For the PC labelled $B-1$ the considered RI range was at this point limited to the given values because for this specific sample problems arose for an infiltration where the RI liquid exceeded the inherent RI of the polymer ($n > 1.53$) and lower RI ranges were not available at that time. For the remaining samples these ranges have been covered and are presented later on.

The measurements of the scattering curves with refractive index-matched liquids are compiled in figure 6.8. Here, one can directly see the influence of the change in the RI contrast. The scattering curves for both reflections do not change their angular pattern but the change occurs in a decrease of intensity with diminuishing contrast. A noteworthy deviation from expectation is the mismatch of the Bragg peak position in the scattering curve of the $(02)T$ reflection compared to the theoretically predicted position at about $\omega = -30°$. This might indicate a problem with the infiltration. For the $(01)T$ reflection a considerable deviation from the kinematic prediction is visible which expresses itself by a smaller number of oscillations in the scattering curve.

6.2.3. RI contrast dependent measurements - sample $B-2$

For this sample the same procedures have been followed as for sample $B-1$. The scattering curves for the uninfiltrated case have been measured and plotted in figure 6.9(a). The $(01)T$ (figure 6.9(a)) and $(02)T$ (figure 6.9(b)) reflections for the uninfiltrated measurements confirm once more the reproducibility. Deviations in the scattering curve of sample $B-2$ compared to sample $B-1$ arise from the fact that for high RIC the scattering curves strongly depend on the alignment conditions, i.e. if the beam will not hit the PC at the exact spot,
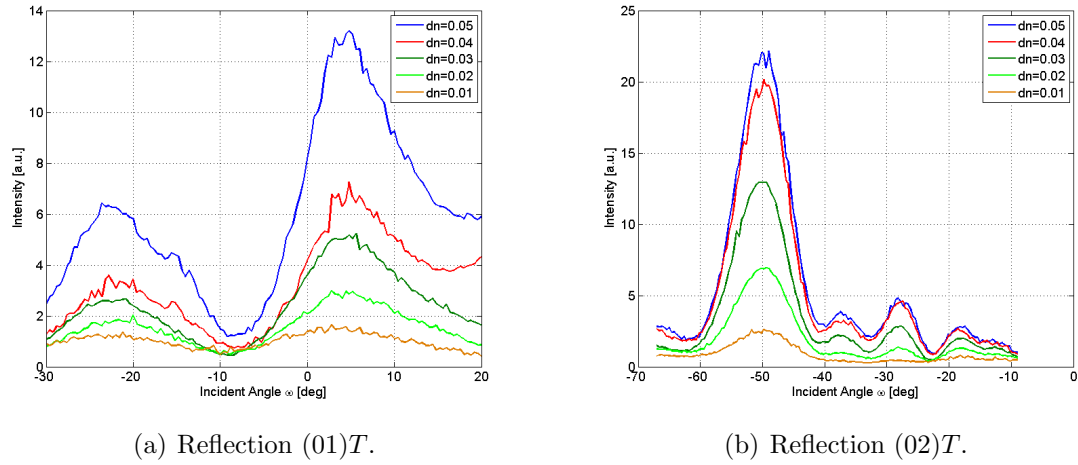
(a) Reflection $(01)T$.

(b) Reflection $(02)T$.

Fig. 6.8.: Sample $B-1$ - Scattering curves of two different reflections as function of different refractive index contrasts.

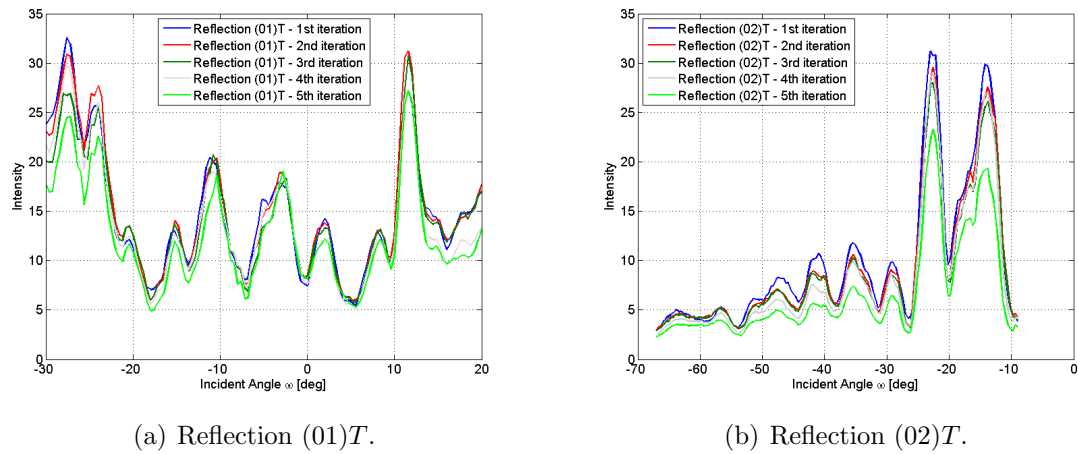then the measured curves can change their shape due to the effect of multiple scattering inside the sample.

(a) Reflection $(01)T$.

(b) Reflection $(02)T$.

Fig. 6.9.: Sample $B-2$ - High RI difference - Multiple measurements in between the cleaning and re-infiltrating processes.

RI dependence in the low contrast regime

The scattering curves corresponding to the infiltrated states are plotted in figure 6.10. The RI difference for the $(01)T$ and $(02)T$ reflections of sample $B-2$ is given by $\Delta n = [0.01; 0.11]$ which corresponds to whole range of available Cargille liquids of set AA, $n = [1.46; 1.63]$. For this sample an infiltration with a liquid having a RI higher than $n > 1.53$ was possible. In this RI range the infiltrated sample has more kinematic-like scattering curves with a pronounced

Bragg peak for the $(02)T$ reflection (cf. figure 6.10(b)). If one compares these results with the curves from PC $B-1$ one finds that the Bragg peak has shifted considerably to a value of $\omega_B = -30°$. This comes much closer to the expected value of $\omega_{B,\text{theo}} = -32.8°$. Both reflections in this regime show a strong dependence on the change of the RI contrast. This is visible in an increase of the scattered intensity for an increasing RI difference. However, a significant change of the curve structure to a more dynamical form could not be observed. If the liquid is above or below the one of the compound polymer seems to have no significant effect on the scattering curves as well.

(a) Reflection $(01)T$.　　　　　(b) Reflection $(02)T$.
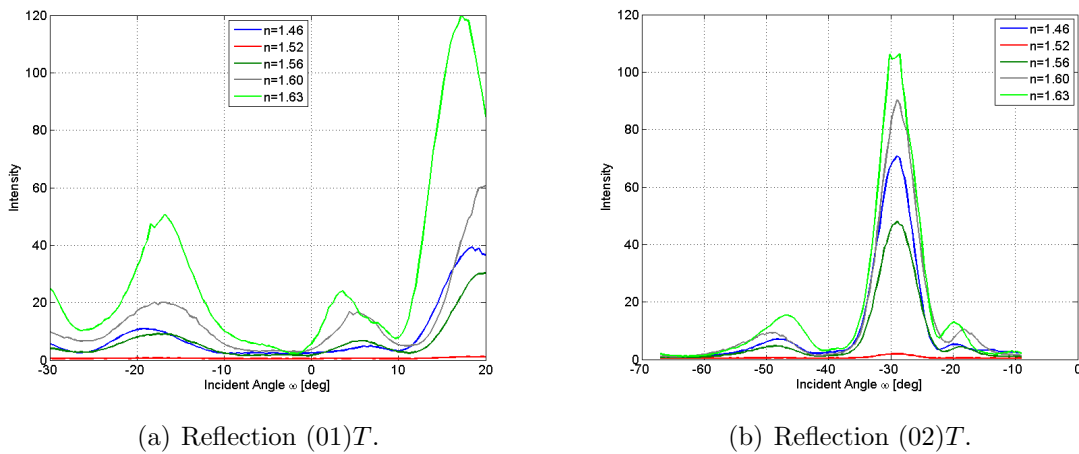
Fig. 6.10.: Sample $B-2$- Measurements for different low RI differences.

Further experimental confirmation of the scattering curves

Due to the slight deviations of the scattering curves from the kinematic expectation which are e.g. the asymmetries in the side fringes of the Bragg peak in the $(02)T$ reflection, additional investigations have been performed. These investigations, which were focussed on the $(02)T$ reflection, included a different setup in which the detector was covered with a narrow slit. For a range of equi-distant ω values detector (θ) scans have been performed. The center of each scan was chosen as the theoretical Bragg peak position θ_B. The detector scan was then performed in the range $\theta \in [\theta_B - 0.8°; \theta_B + 0.8°]$ with a step size of $0.2°$. The scans have been performed for ω in the range of $\omega \in [-9°; -67°]$ in steps of one degree. The results have been summarized in figure 6.11 and in figure 6.12.

The reason for this investigation was to get a confirmation of the intensity distribution measured from the scattering curves. The RI liquid chosen for this had a value of $n_{\text{Liq}} = 1.46$ because the scattered intensity was high enough to be detectable despite the used slit. The slit was used to get a precise information about the location of the Bragg peak in the $\omega - \theta$

space. The measured curves for the PC infiltrated with this liquid are depicted in figure 6.11(a) in an isometric view. The peak maximum of the θ-scan is marked by a pink asterisk. In the adjacent figure 6.11(b) a comparison of the previously determined experimental peak
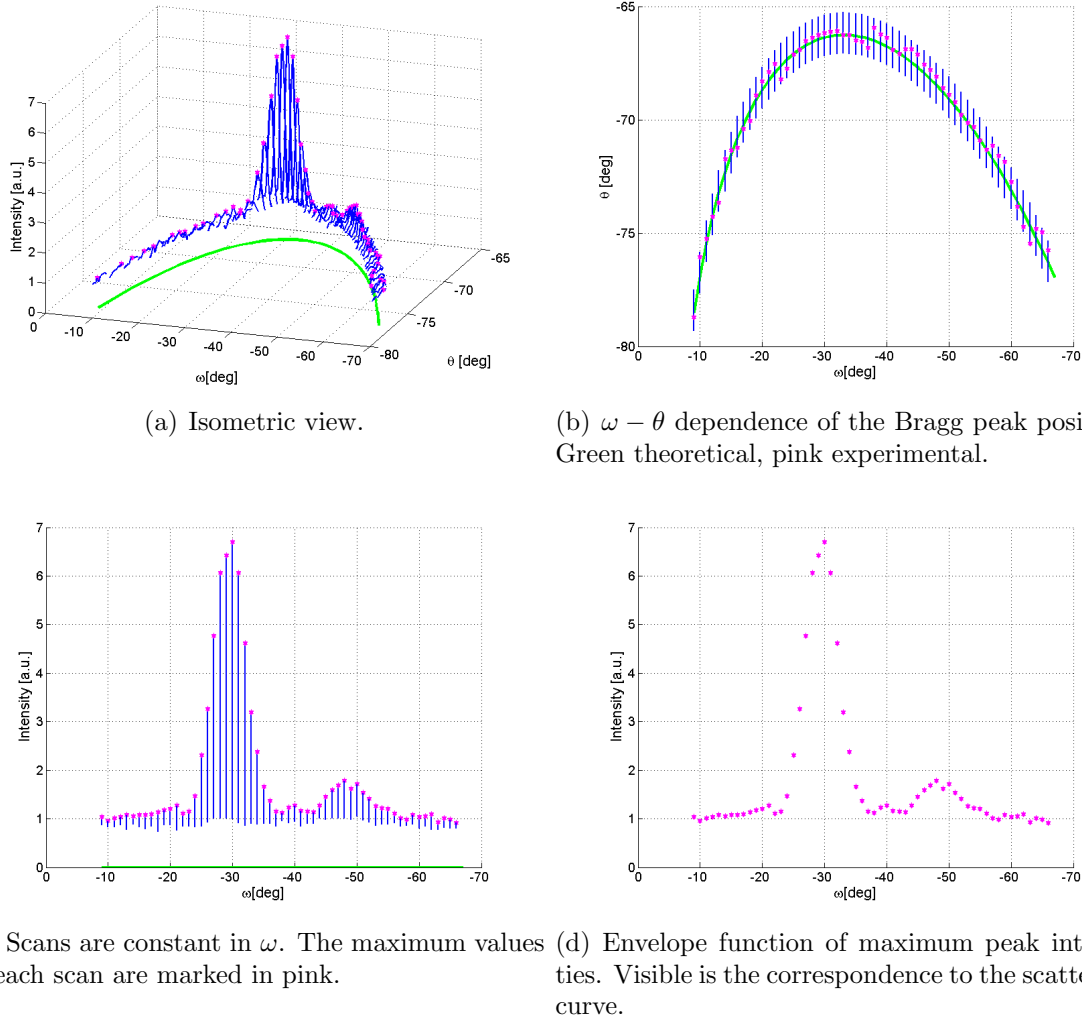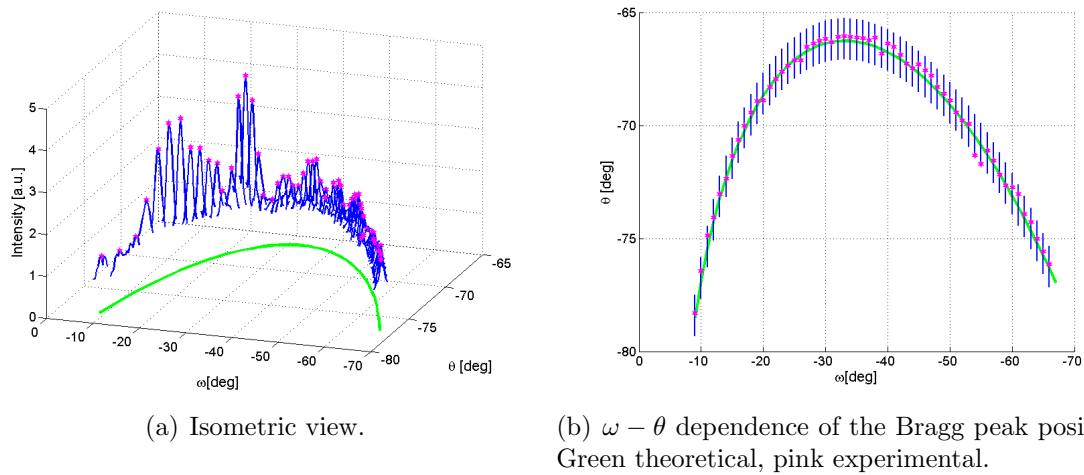

(a) Isometric view.

(b) $\omega - \theta$ dependence of the Bragg peak position. Green theoretical, pink experimental.

(c) Scans are constant in ω. The maximum values of each scan are marked in pink.

(d) Envelope function of maximum peak intensities. Visible is the correspondence to the scattering curve.

Fig. 6.11.: Measurements for $n_{\text{Liq}} = 1.46$ of reflection $(02)T$. The green curve shows the theoretical peak progression as a function of ω and θ. The blue curves show detector (θ) scans at a fixed ω value. The pink dots indicate the peak maximum at each scan.

positions is compared to the theoretically predicted peak maximum represented by the green-coloured line. This comparison shows that there are deviations between the experimental values and the theoretical curve. Since the deviations are scattered on both sides of the curve the conclusion is that they are caused by experimental uncertainties and do not represent a systematical error. However, deviations in the scattering curve can be explained by this comparison, especially by considering the jump in the peak position close to the Bragg peak at $\omega = -38°$. This jump could be one explanation for the asymmetry in the $(02)T$ reflection.

Furthermore, it definitely indicates a lack of quality in the infiltration which can be explained by a bad functional interaction between liquid and PC.

Out of the maximum intensities of each θ - scan a scattering curve can be reconstructed (cf. figure 6.11(c) and figure 6.11(d)). The envelope function connecting the maximum intensities corresponds to a scattering curve. The reconstructed curve is visualized as the pink dots in figure 6.11(d) and it fits very well the scattering curve that has been recorded with a reflection scan (cf. figure 6.10(b)). From the curves the advantage of the reflection scan is also directly clear which is the possibility to measure without any slit. This means a decrease in the time necessary for a measurement and a higher resolution.

(a) Isometric view.

(b) $\omega - \theta$ dependence of the Bragg peak position. Green theoretical, pink experimental.
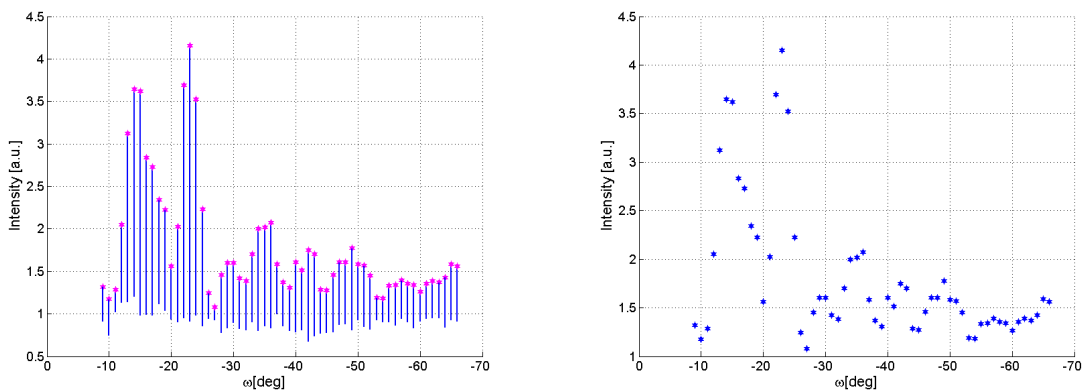
(c) Scans are constant in ω. The maximum values of each scan are marked in pink.

(d) Envelope function of maximum peak intensities. Visible is the correspondence to the scattering curve.

Fig. 6.12.: Measurements of reflection $(02)T$ without liquid infiltration. The green curve shows the theoretical peak progression as a function of ω and θ. The blue curves show detector (θ) scans at a fixed ω value. The pink dots indicate the peak maximum at each scan.

For the uninfiltrated state a similar analysis has been made and is illustrated in figure

6.12. Although a clear Bragg peak in this case is missing, a noteworthy result is that the observed peak follows the $\omega - \theta$ dependence quite well.

6.2.4. RI dependence in the medium contrast regime

Since the measurements in the previously investigated low contrast regime did not show any considerable effects, additional measurements with an infiltration with liquids of a RI range of $n_{\text{Liq}} \in [1.3; 1.39]$ were made. Thus, the $(10)T$ and $(20)T$ reflections were measured as a function of the refractive index. These reflections were also chosen to check if they were symmetric to the $(01)T$ and $(02)T$ reflections. In order to have a full data set the low contrast regime was measured for these reflections again. The results for these measurements (low contrast, $n \in [1.46; 1.64]$) have been compiled in figure 6.13 as well as the scattering curves measured after removing the liquid, in order to check for misalignments. The infiltrated
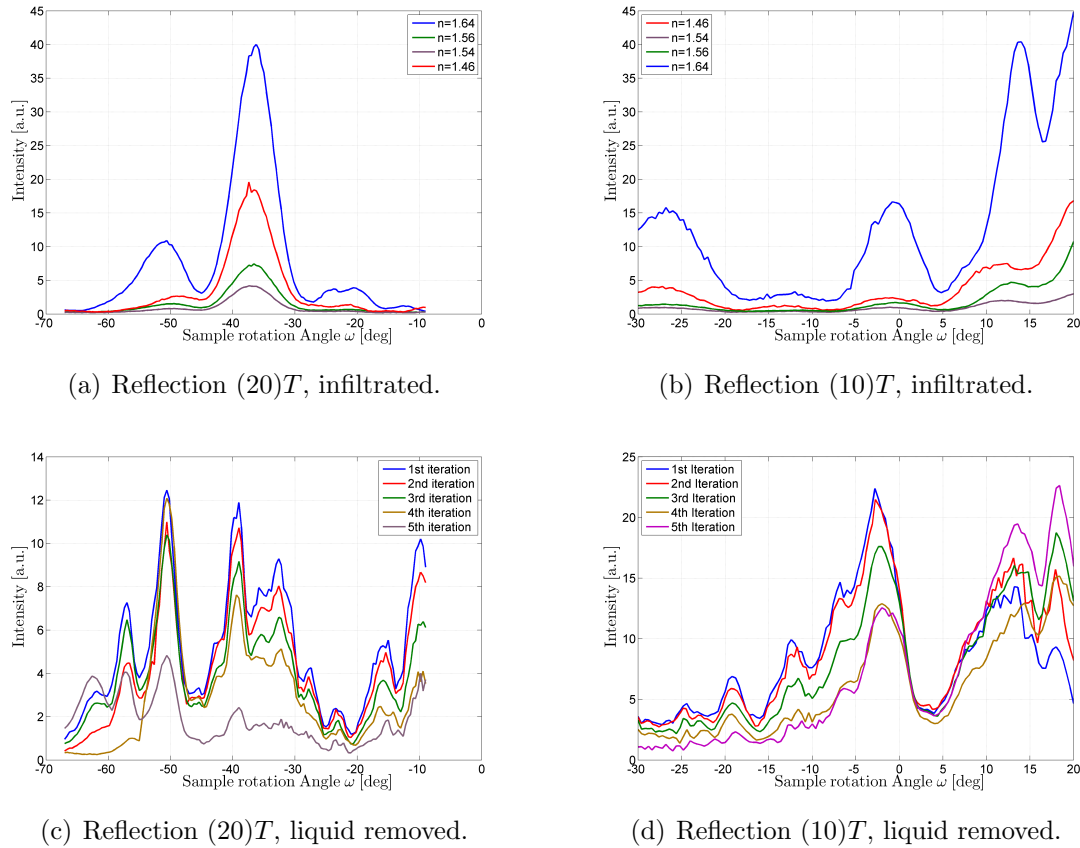

(a) Reflection $(20)T$, infiltrated.

(b) Reflection $(10)T$, infiltrated.

(c) Reflection $(20)T$, liquid removed.

(d) Reflection $(10)T$, liquid removed.

Fig. 6.13.: Compilation of scattering curves of the $(10)T$ and $(20)T$ reflections for a WP PC $(B-2)$ infiltrated with RI liquids in the range of $n \in [1.46; 1.64]$ and for comparison the scattering curves after deletion of the liquids.

scattering curves show a typical Bragg peak which is given at $\omega_B = -36.3°$. This deviates

considerably from the theoretical value of $\omega_{B,\text{theo}} = -32.8°$. Furthermore, there are asymmetries in the intensities of the side fringes of the Bragg peak which is best visible in figure 6.13(a) for the case of $n = 1.64$ due to the scale. Nonetheless, the same inconsistencies are also given for lower contrasts. These two facts point out a possible influence of the infiltration/sample quality like it was previously observed for other samples (SU-8). Additionally, the $(10)T$ reflections also deviate considerably from expectations (figure 6.13(b)). However, in this case it is necessary to mention that the scattered intensity increases with increasing RI contrast. The scattered curves without RI liquid show a good agreement with each other in their shape, but it has to be mentioned that for each iteration there is a small drop in the intensity. This is caused by the earlier discussed jet of IPA that very likely causes a small shift of the glass substrate causing a misalignment of the PC towards the incident beam. For the last iteration it can be said that the PC was completely misaligned due to the massive drop in intensity.
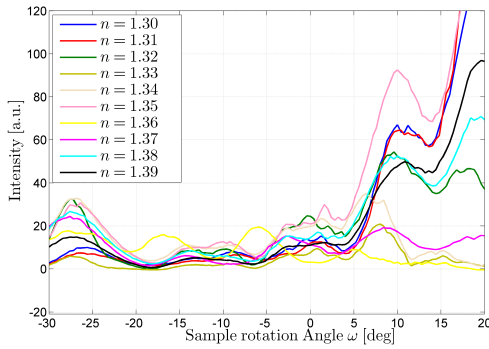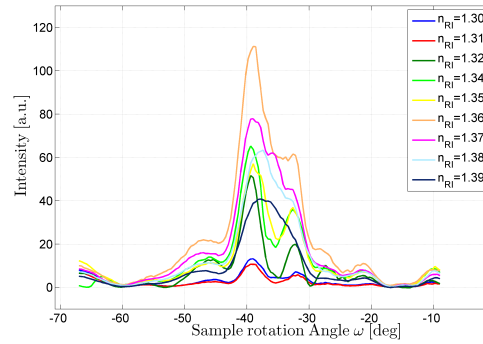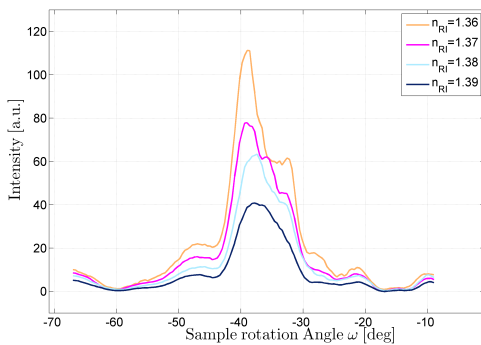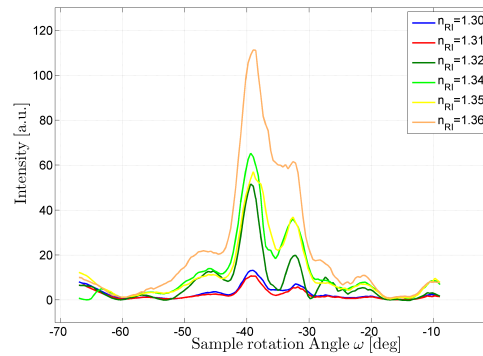

(a) Reflection $(10)T$, infiltrated.

(b) Reflection $(20)T$, infiltrated.

(c) Reflection $(20)T$, selected scans for lower contrast $n > 1.36$.

(d) Reflection $(20)T$, selected scans for higher contrast $n < 1.36$.

Fig. 6.14.: Compilation of scattering curves of the $(10)T$ and $(20)T$ reflections for a WP PC $(B-2)$ infiltrated with RI liquids in the range of $n \in [1.3; 1.39]$.

An addditional set of RI liquids made it possible to increase the RI contrast further (Cargille

Liquid Series AAA). Selected measurements of the scattering curves with this RI contrast are presented in figure 6.14. In order to have a better overview the $(20)T$ (cf. figure 6.14(b)) reflections were subdivided into two ranges from $\Delta n \in [0.13; 0.16]$ (cf. figure 6.14(c)) and from $\Delta n \in [0.16; 0.22]$ (cf. figure 6.14(d)). The $(20)T$ reflections in the range from $n \in [1.36; 1.39]$ show an increase in scattering intensity and more importantly a change in the scattering pattern which is visible in a splitting of the Bragg peak, starting from an RI contrast of $\Delta n = 0.14$. This splitting becomes more pronounced the higher the contrast gets, especially for $\Delta n = 0.14$ a shoulder of the Bragg peak is visible. Even higher contrasts amplify the effect of peak splitting. Moreover, the intensity is decreasing for increasing contrast. For the last scattering curves recorded at highest RI contrast ($n = 1.30$, $n = 1.31$) the intensity drop is not necessarily a physical effect due to the RI contrast but can be rather explained by a minor misalignment.

The scans of the $(10)T$ reflection have been summarized in figure 6.14(a). This reflection shows no clear tendency for different contrasts which is at first surprising because the $(20)T$ reflection showed a visible effect. But then the most probable reason for this is that the $(10)T$ reflection as a weak reflection is experimentally more sensitive to the infiltration procedure and to the quality of the sample alignment which can be influenced by the exfiltration of the RI liquid.
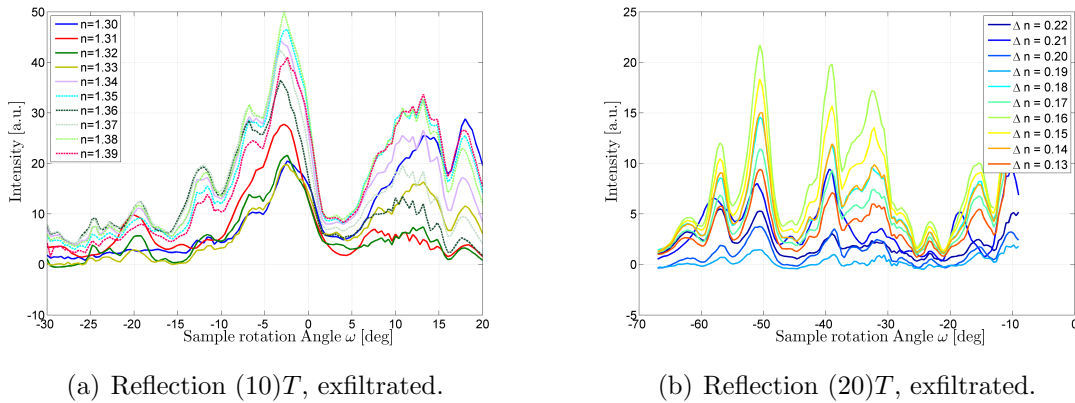

(a) Reflection $(10)T$, exfiltrated.

(b) Reflection $(20)T$, exfiltrated.

Fig. 6.15.: Compilation of scattering curves of the $(10)T$ and $(20)T$ reflections for a WP PC $(B-2)$ **after exfiltration** in the medium contrast regime. Given RI value indicates the coresponding liquid that was removed.

Problems in the alignment can be discussed by regarding figure 6.15. In this figure, it is clearly visible that for different iterations a profound change in the scattered intensity occurs. That is most likely due to a small misalignment which is caused by a shift of the glass substrate. Fortunately, this misalignment can be considered small because the angular scattering pattern is not influenced. By considering the intensity variation in the exfiltrated

state, one can recalculate/correct the intensities for the infiltrated state. In this case it is especially necessary to reconsider the $n = 1.3$, $n = 1.31$ cases.

6.2.5. Confirmation of scattering classification - sample C

Sample set C marks the final stage of the WP-structured PC development. For reasons of comparison the lattice parameters were kept at the same values as for sample set B. Since in the medium contrast regime there have been several inconsistencies this should be overcome with this set of samples. The quality of the samples has been analyzed by judging the transmission and reflectance spectra and it was found that this sample set should be of high quality [65].

The monochromatic measurements of the scattering curves have been done in the same way as for the previously discussed sample sets. Furthermore, the infiltration technique was not changed which means that it took place while the sample was mounted onto the diffractometer. The liquid removal process was done by using isopropyl alcohol.

In figure 6.16 a set of measurements of the $(10)T$ reflection has been drawn. In this case measurements of the infiltrated samples are shown. In order to make it clearer the set of scans over the entire refractive index range in figure 6.16(a) has been split into two sets. One includes the range from $n = 1.46$ to $n = 1.5$ (6.16(c)) while the other one includes the range from $n = 1.3$ to $n = 1.39$ (6.16(b)).

The first impression confirms qualitatively previous findings which have shown an increase in the diffraction efficiency for increasing contrasts.

In order to check if the removal process has had any permanent influence on the crystal the scattering curves are recorded before and after the measurements of a specific contrast. Moreover, it can give a hint of the reproducibility. One major issue is the mechanical stability of the setup that might be affected by the influence of the stream of liquid incident on the substrate for either removing or filling the sample.

In figure 6.17 the scans of the uninfiltrated and cleansed sample are depicted. In 6.17(a) the complete set of measurements is shown. However, due to poor comparability the set is subdivided into three other sets given in 6.17(b), 6.17(c) and 6.17(d) comparing different alignments with each other.

The same procedure has been done for measuring the $(20)T$ reflection. In figure 6.18 a compilation of scattering curves is shown for the WP PC infiltrated with RI liquids. For reasons of clarity and comprehensibility the entire set of scans (cf. figure 6.18(a)) has been subdivided into three sets representing different RI ranges. The scans of an RI range with lowest contrast (cf. figure 6.18(c)) show a clear Bragg peak with kinematic side fringes. This is also visible for an increased contrast with $\Delta n = [0.13; 0.16]$ which just differs from the lower
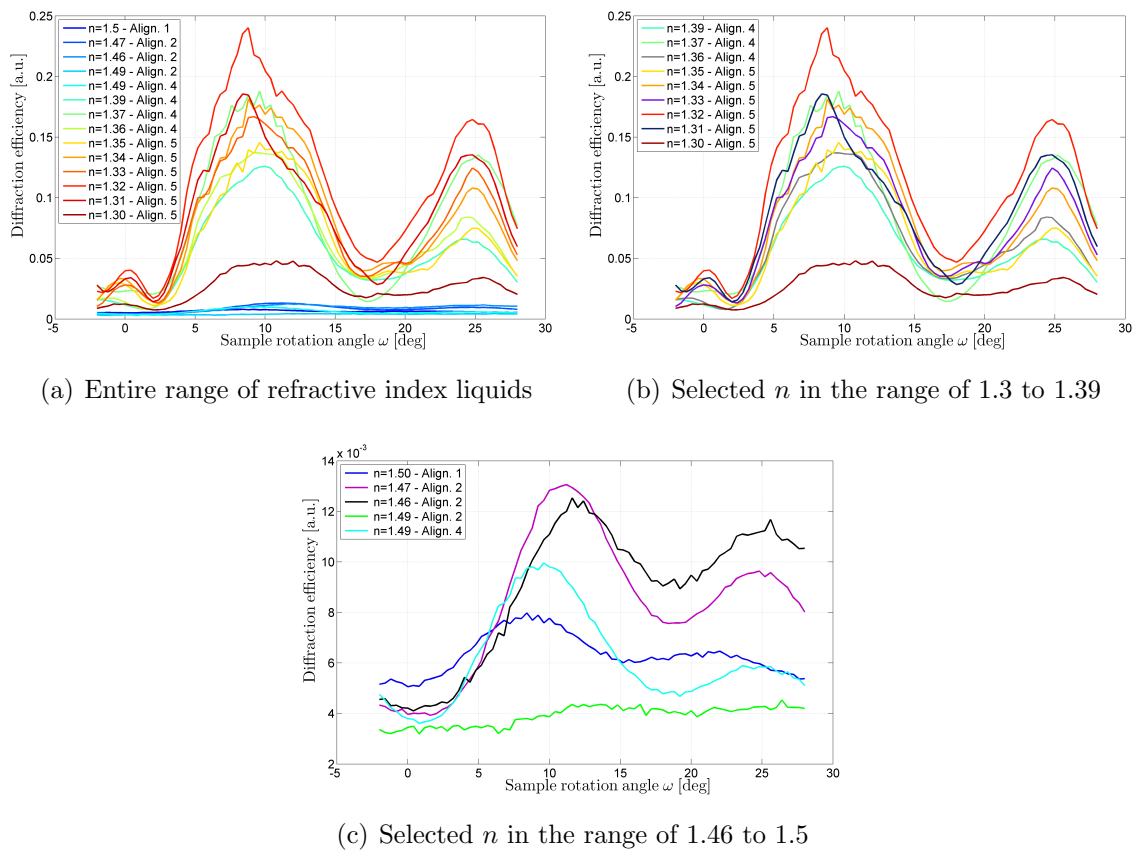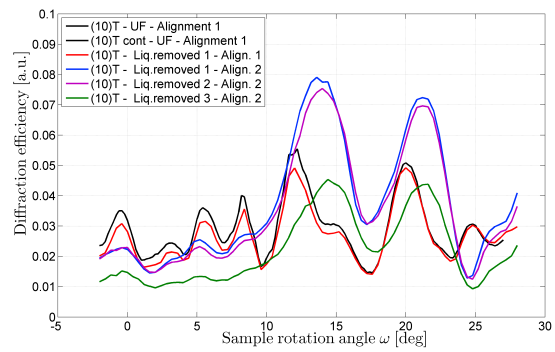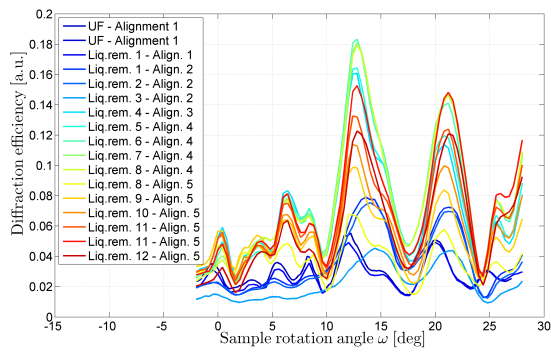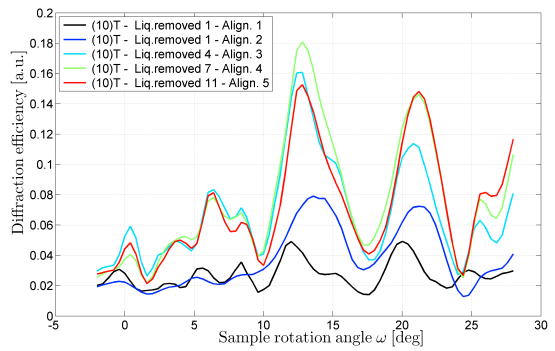
(a) Entire range of refractive index liquids

(b) Selected n in the range of 1.3 to 1.39

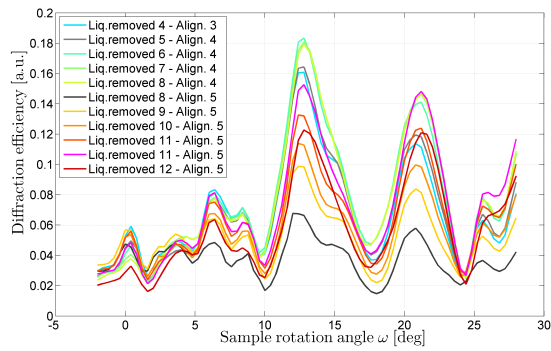(c) Selected n in the range of 1.46 to 1.5

Fig. 6.16.: Scans of the $(10)T$ reflection of sample C filled with refractive index liquids.

(a) Complete set of scans of the cleansed sample.

(b) Selected set of scans of the cleansed sample for sample alignment no. 1 and 2 .

(c) Selected set of scans of the cleansed sample for sample alignment no. 3, 4 and 5 .

(d) Selected set of scans of the cleansed sample for alignment 1, 2, 3, 4 and 5.

Fig. 6.17.: Scans of the $(10)T$ reflection of sample C before and after removing the refractive index liquids.

contrast by the intensity of the scattered beam. The highest contrast ($\Delta n = [0.17; 0.22]$) adjustable with the RI liquids (figure 6.18(b)) shows a variation from the kinematic Bragg peak structure and that is firstly a splitting of the central peak which is stronger the higher the RI contrast and secondly a scattered intensity almost independent of the RI contrast.
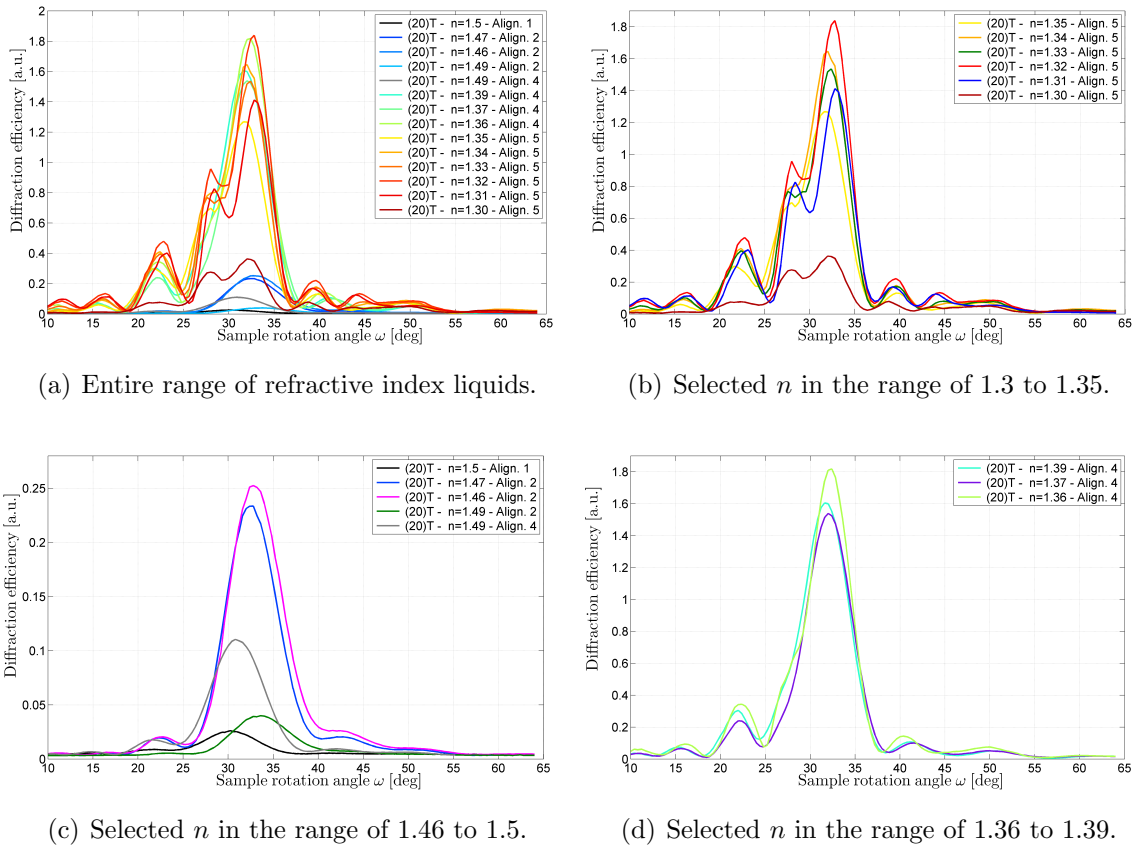

(a) Entire range of refractive index liquids.

(b) Selected n in the range of 1.3 to 1.35.

(c) Selected n in the range of 1.46 to 1.5.

(d) Selected n in the range of 1.36 to 1.39.

Fig. 6.18.: Scans of the $(20)T$ reflection of sample C filled with refractive index liquids.

The experimental quality of the alignment can be judged by taking a look at figure 6.19. An ensemble of scattering curves for the exfiltrated state has been depicted there. For clarity different scans have been compared again, this is due to the fact that for the experiment different alignments (five) were necessary. A comparison of the alignments revealed that most alignments resulted in the same scattering behaviour with different intensities. However, one alignment (no. 2) did not match the scattering behaviour and therefore one has to check for deviations in the corresponding scattering curves for this RI contrast. The respective scans affected by those deviations were the measurements for the low contrast regime ($\Delta n = [0.01; 0.06]$). In this case one can see that those alignments had an effect on the scattering curves. The scans corresponding to alignment no. 2 have a slight shift of the Bragg peak of a few degrees compared with the Bragg peak of alignment no. 4. This can be explained by the fact that the laser does not hit the sample completely in alignment no. 2. This

can be seen by comparing the green and grey curve both representing the same reflection of the same RI contrast. The scan corresponding to alignment no. 4 has a higher intensity which emphasizes the fact that in the second alignment case the incoming laser beam did not completely illuminate the PC. All the other alignments except no. 2 have a similar scattering behaviour, so it can be concluded that scans corresponding to the alignments no. 1, 3, 4 and 5 have the same experimental boundary conditions.

6.2.6. Discussion of the results

The experimental measurements that have been carried out require a discussion and further analysis. One main point of this work is to find out the validity of the kinematic approximation of the scattering curves for different RI contrasts. The experimental findings indicate that the dependence on the RI contrast is not independent of the considered reflection. Therefore, a discussion is made for each reflection separately. The two major points for a subclassification are

- the development of the scattering efficiency as a function of the RI contrast and

- the point of transition where the scattering curves change from a kinematic Bragg peak to a more complicated structure (for the $[02]T$ reflection only).

**Quantitative analysis of the scattering curves**

Up to now the measurements were discussed qualitatively, therefore a more quantitative analysis is necessary in order to make a reliable distinction of the scattering curves in terms of RI contrast. The data shown in previous figures were not corrected for any possible side effects. However, several aspects have to be taken into account. Firstly, it is necessary to subtract a background scattering. This means that for larger angles some regions of the crystal will not be illuminated with equal intensity resulting in a broadened interference condition which affects the scattered intensity especially close to the Bragg peak (cf. figure 6.21). This causes an angle-dependent background that needs to be subtracted. This is done by fitting a spline-function to the minima and subtracting this curve from the measured data. Secondly, experimental factors have to be considered like errors in the alignment of the angles, e.g. $\Delta\omega$. Lastly, optical corrections due to the Fresnel reflectivity has to be taken into account, however their influence is rather negligible. The whole procedure is demonstrated for one example in figure 6.20 for the $(20)T$ reflection of a PC infiltrated with an RI liquid of $n = 1.39$. The corrected curve can be used for comparison with the kinematic approximation. Especially the angle-dependent background can play an important role. Throughout the whole procedure it was assumed that the refractive index has no specific angle dependence.
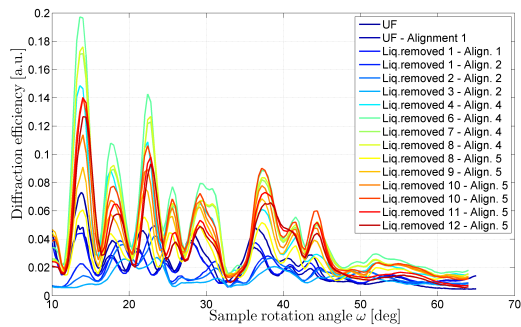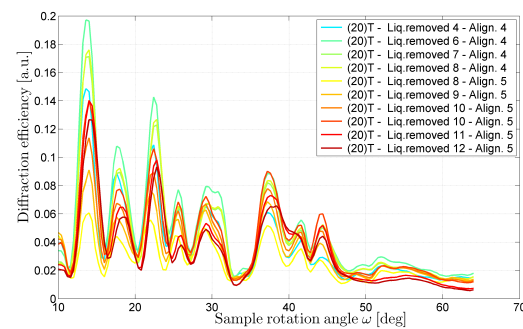
(a) Complete set of scans.
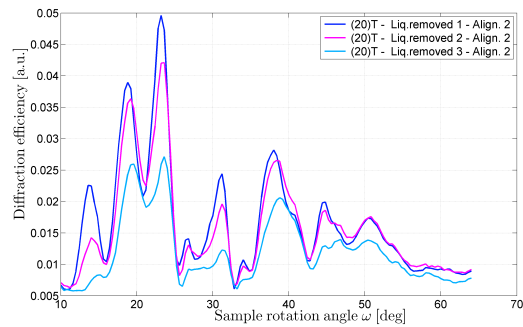
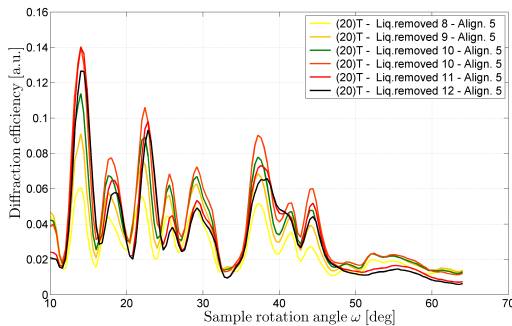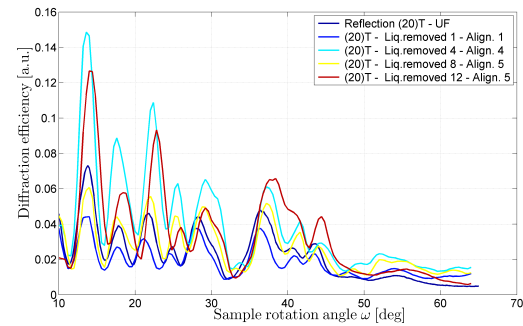(b) Comparison of scans of alignment no. 2.
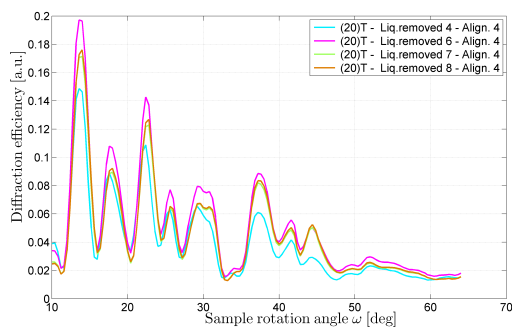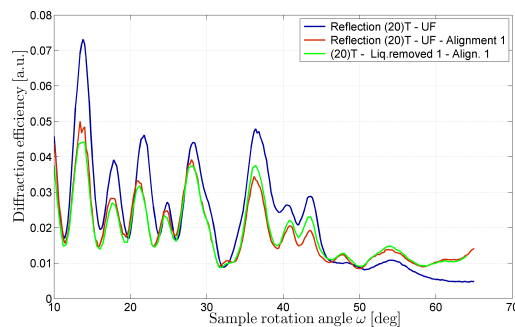
(c) Comparison of scans of alignment no. 4.

(d) Comparison of scans of alignment no. 4 and 5.

(e) Comparison of scans of alignment no. 5.

(f) Comparison of selected scans of all alignments.

(g) Comparison of scans of alignment no. 1.

Fig. 6.19.: Scans of the $(20)T$ reflection of sample C before and after removing the refractive index liquids.
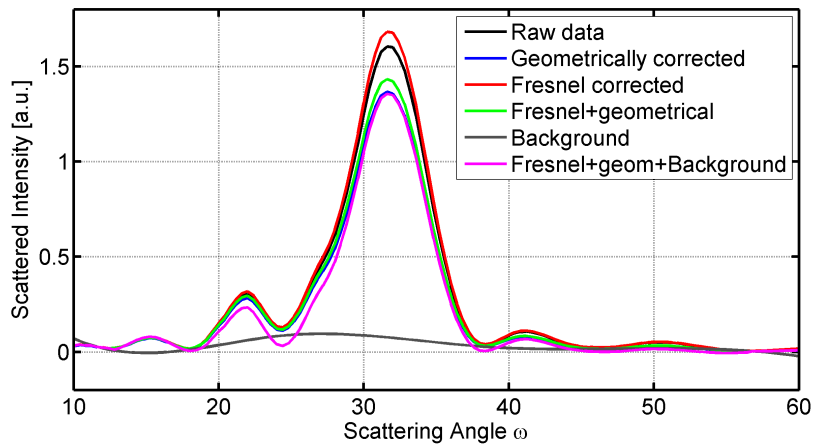
Fig. 6.20.: Scattering curve for the $(20)T$ reflection. PC is infiltrated with an RI liquid of $n = 1.39$. Black curve shows the raw data, blue curve represents the correction for geometrical reasons, the red one stands for the Fresnel-reflectivity corrected data while the green one takes into account both effects. The grey line shows the angle-dependent background which is subtracted from the data. The pink curve shows the fully corrected scattering curve.

For PCs with a high refractive contrast this assumption is definitely not true as was shown in chapter 2.2.1, however for a sufficiently low contrast the effective refractive index can be averaged.

(a) $\omega = 0°$ (b) $\omega = 32°$
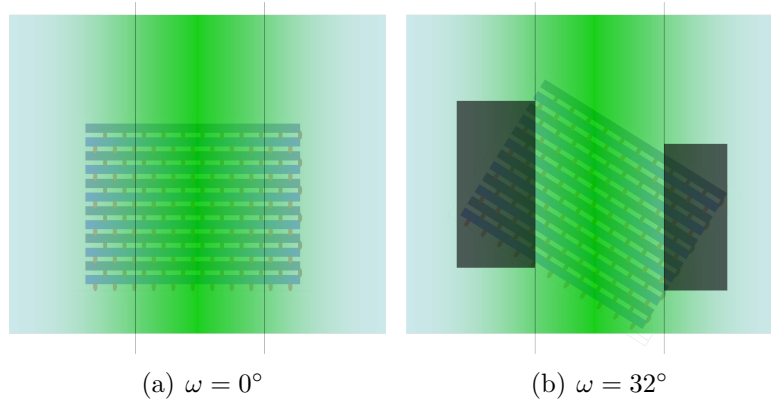
Fig. 6.21.: Gaussian laser beam is incident upon the PC. In the case for $\omega = 32°$ which corresponds approximately to the Bragg angle, there are regions (highlighted black) of the PC that are illuminated with light of different intensity. This causes a change in the phase summation and results in the broadening of the interference condition which is visible by an angle-dependent background.

Kinematic fit of the $(20)T$ **reflection**   As already done for the numerical simulations the experimental curves can be compared to the kinematic approximation. This is done by fitting a kinematic model to the experimental data. For the $(20)T$ reflection equation (6.2)

is used as a model.

$$I^{(20)T}(l) = I_0 \left(\frac{\sin\left(N_c\, B\, \pi \cdot (l - l_0)\right)}{N_c\, \sin\left(B\, \pi \cdot (l - l_0)\right)} \cdot \cos\left(\pi + \frac{\pi}{2} \cdot B\,(l - l_0)\right) \right)^2 \tag{6.2}$$

This model is based on three parts that were explained earlier (cf. 5.3.3 on page 65) and are shortly recaptured here, these are

1. the structure factor,

2. the form factor of a single scattering element and

3. the lattice sum.

The first one considers the phase-correct summation of the elements located in the unit cell and is in the model accounted for by

$$\left(\cos\left(\pi + \frac{\pi}{2} \cdot B\,(l - l_0)\right) \right)^2 .$$

While the form factor of the single scattering element is approximated by unity. The third term is considered by the well-known Laue function:

$$\left(\frac{\sin\left(N_c\, B\, \pi \cdot (l - l_0)\right)}{N_c\, \sin\left(B\, \pi \cdot (l - l_0)\right)} \right)^2$$

Before fitting the model, the experimental data is transferred to reciprocal space by the well-known transfer function. The results of these fits are tabulated in table 6.2 while selected fits are plotted in figure 6.22. The fitted parameters correspond to the following physical values. I_0 stands for the diffraction efficiency while B is a measure of the c-value of the PC. Smaller values might indicate a shrinking of the polymer. The l_0 value shows the validity of the Bragg condition. Deviations might occur due to misalignment. The R^2 statistic measures how successful the fit is in explaining the variation of the data [62]. In other words, R^2 is the square of the correlation between the response values and the predicted response values. It is defined as (cf. (5.5)):

$$R^2 = 1 - \frac{\text{sum of squares due to error}}{\text{total sum of squares}} \tag{6.3}$$

R^2 can have any value between 0 and 1. For a value of $R^2 = 1$ the fit accounts for all the variations in the data. For a value of 0.5 the fit explains 50 per cent of the variation of the
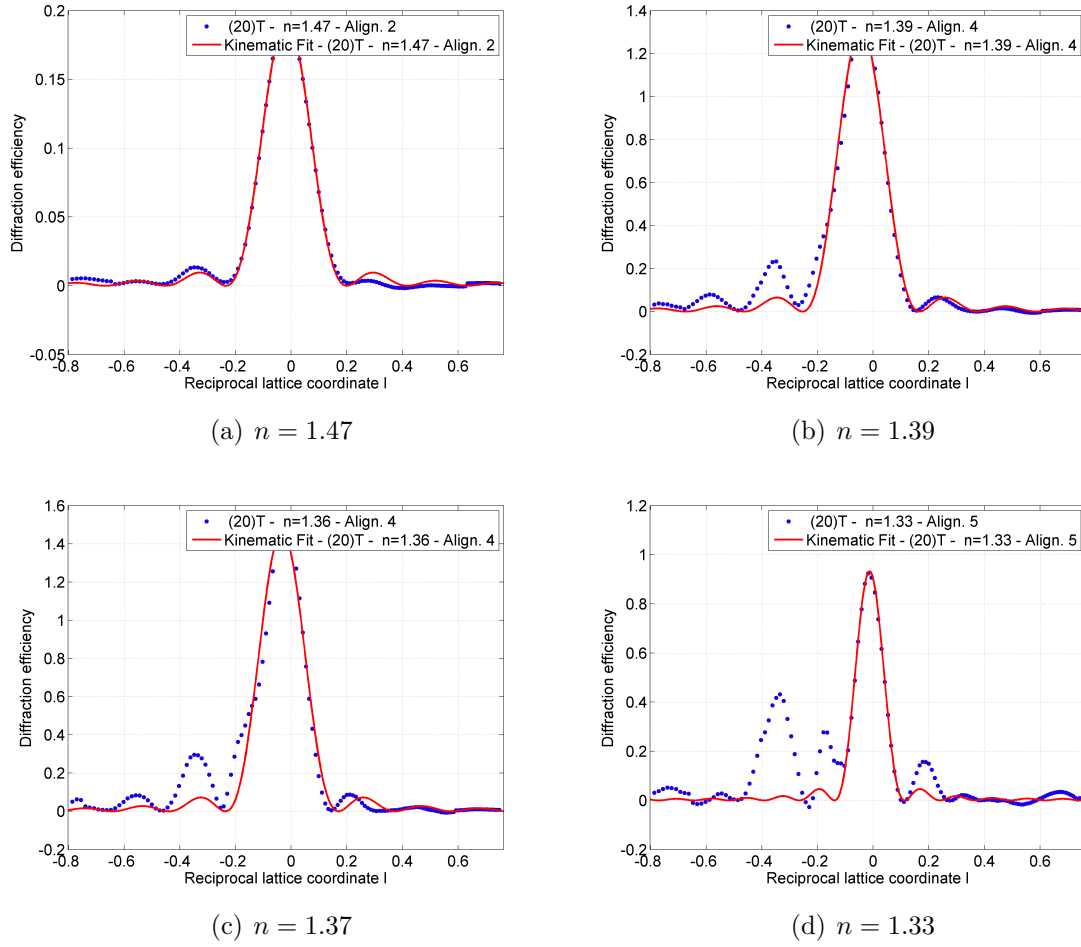
(a) $n = 1.47$

(b) $n = 1.39$

(c) $n = 1.37$

(d) $n = 1.33$

Fig. 6.22.: Selected kinematic fits to the corrected scattering curves.

RI Liq. (Align. no.)	B	ΔB	I_0	ΔI_0	l_0	Δl_0	R^2_{adj}
$n = 1.47$ - Align. 2	0.77	0.01	0.19	0	-0.017	0.001	1
$n = 1.46$ - Align. 2	0.76	0.01	0.21	0.01	-0.005	0.001	0.99
$n = 1.49$ - Align. 4	0.75	0.01	0.09	0	-0.062	0.001	0.99
$n = 1.39$ - Align. 4	0.79	0.02	1.32	0.04	-0.044	0.002	0.98
$n = 1.37$ - Align. 4	0.82	0.02	1.28	0.02	-0.032	0.002	0.99
$n = 1.36$ - Align. 4	0.82	0.03	1.47	0.06	-0.033	0.003	0.95
$n = 1.35$ - Align. 5	1.1	0.11	0.7	0.08	-0.034	0.006	0.73
$n = 1.34$ - Align. 5	0.78	0.04	1.26	0.06	-0.049	0.005	0.92
$n = 1.33$ - Align. 5	1.32	0.13	0.93	0.09	-0.013	0.005	0.74
$n = 1.32$ - Align. 5	1.39	0.14	1.14	0.12	-0.004	0.005	0.7
$n = 1.31$ - Align. 5	1.43	0.17	0.88	0.1	0.004	0.006	0.61
$n = 1.30$ - Align. 5	1.41	0.16	0.2	0.02	-0.018	0.007	0.63

Tab. 6.2.: Fit parameters of the kinematic model for the respective RI contrast scattering curves of the $(20)T$ reflection. The last column shows the adjusted R^2 value which gives an indication about the validity of the model.

data by the model. The degrees of freedom adjusted R^2 value takes also into account the number of parameters used for the model. That is why it is used in this case.

The adjusted R^2 value of the fit gives an indication of the validity of the kinematic approximation. As one can see in the tabulated results the validity of the model decreases for increasing RI contrast. For a contrast up to $\Delta n = 0.15$, $n_{\text{Liq}} = 1.37$, the kinematic fit can explain more than 98% of the total variation in the data about the average. The RI liquid with $n_{\text{Liq}} = 1.36$ marks the beginning of a change from a quasi-kinematic scattering regime to a regime of transition. Although the R^2_{Adj} value for the $n = 1.34$ liquid shows a quite good agreement, the general tendency of a decreasing coincidence is clearly visible.

Based on the analysed $(20)T$ reflection the following distinction of scattering regimes can be made.

1. Quasi-kinematic scattering regime: $\Delta n \in [0.1, \, 0.15]$ corresponding to infiltrated liquids $n \in [1.51, \, 1.37]$. An indication for this is the clear Bragg peak combined with an increase in the scattering efficiency.

2. Scattering regime of transition: $\Delta n \in [0.16, \, 0.22[$ where the higher value is given by the lowest RI liquid available. This regime might extend beyond the value of $\Delta n = 0.22$.

3. 'Dynamic' scattering regime: This regime is given for the uninfiltrated sample at $\Delta n = 0.52$.

Comparison of experiment and simulation based on kinematic approximation

In order to verify or falsify the experimental results, it is required to compare them with theoretical investigations. In the previous chapter the proper simulations have been presented. Due to the earlier discussed numerical issues of the simulation of the $(20)T$ reflection, this reflection should not be considered when comparing experiment and theory. Moreover, the simulations for the $(10)T$ reflection yielded more reliable results with a lesser number of divergences. For the experimental part the situation is vice versa. The measurement of the $(20)T$ reflection is less susceptible to experimental side effects compared to the $(10)T$ reflection.

The comparison focusses firstly on the kinematic fit results. For a better visualization, the fitted parameters are compared in figure 6.23. According to the adjusted R^2 value the kinematic approximation is in good agreement with experiment and simulation for a contrast up to $\Delta n = 0.13$ which means for the RI liquid that $n_{\text{Liq}} = 1.39$. The agreement slowly decreases for an increasing contrast until there is a small jump which indicates the transition into another regime. Therefore, it only makes sense to compare the fit parameters where the goodness of the fit is sufficiently high ($R^2 > 0.88\%$). The development of the scattering
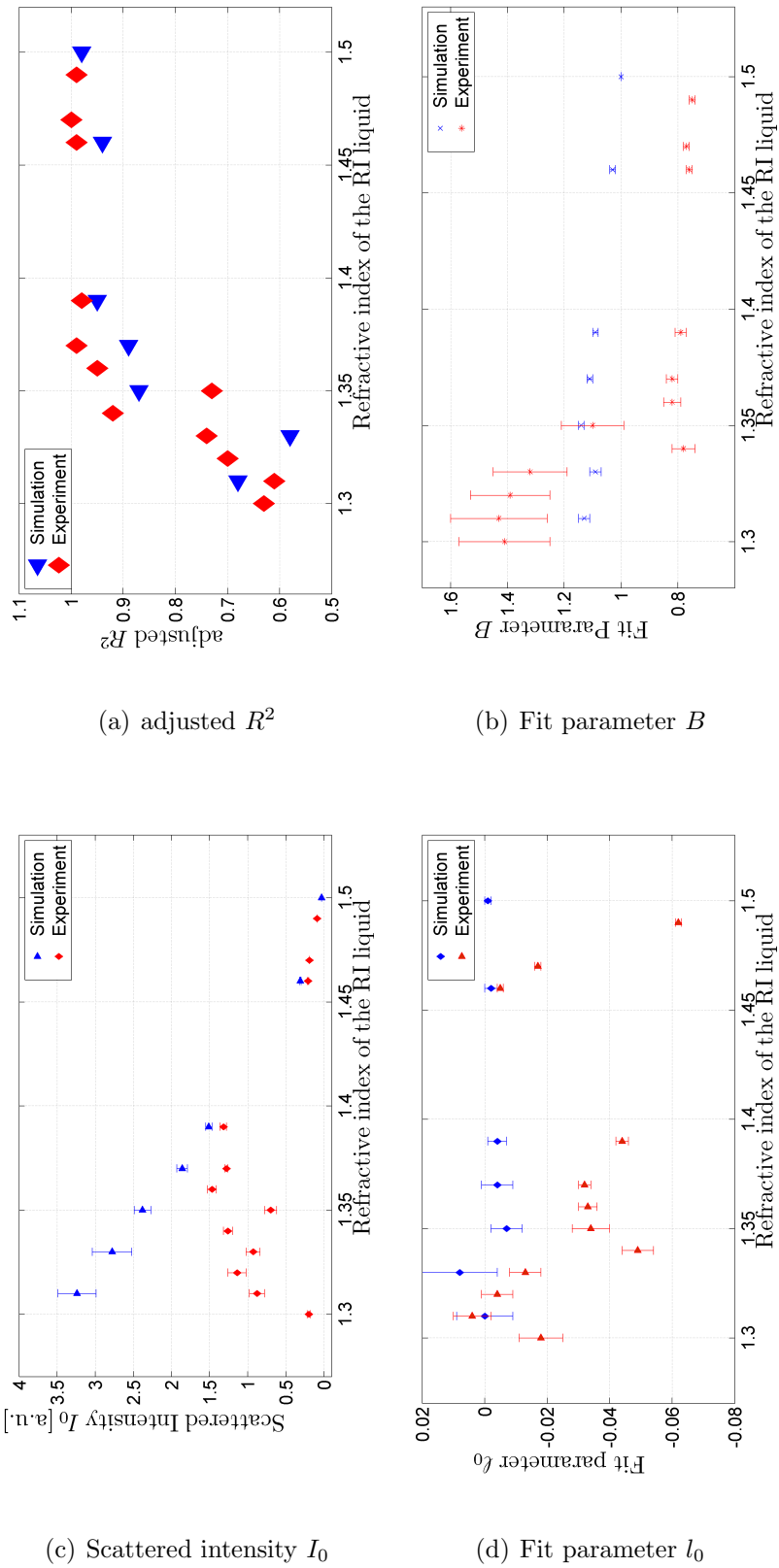
(a) adjusted R^2

(b) Fit parameter B

(c) Scattered intensity I_0

(d) Fit parameter l_0

Fig. 6.23.: Comparison of the fit results of the kinematic approximation for simulation and experiment.

efficiency of simulation and experiment as a function of contrast show a similar dependence (cf. figure 6.23(c)). In the quasi-kinematic regime, the calculated diffraction efficiency is constantly larger than the measured one. However, the error bars only indicate the error from the fit and not the experimental one, so that a deviation of less than 20% can still be considered very good. For a higher contrast the values are not comparable due to the already mentioned lack of validity of the model. The outcome of the comparison of the fit parameter B shows a constantly larger value for the simulation. The physical meaning of this parameter is the deviation from the assumed out-of-plane lattice constant $c = \sqrt{2}a$. While for the simulation this value is approximately one, the experiment indicates a significant smaller value. After consulting the sample producer, a possible explanation for this can be a shrinkage of the polymer. The l_0 parameter is a measure for the alignment of the sample rotation angle $\Delta\omega$. Here, the experiment shows only a minor misalignment.

Interpretation of the results

The achieved results allow a subdivision into different scattering regimes (cf.table 6.3). For samples with an inherent low RI contrast ($\Delta n \approx 10^{-3}$), it was shown that their scattering is strongly kinematic [11]. In order to tune the RI contrast, PCs were infiltrated with RI liquids. In the range from $\Delta n = [0.01 - 0.15]$ the obtained results show a clear Bragg peak with side fringes, with increasing RI contrast the diffraction efficiency increases. Therefore, this RI regime is called quasi-kinematic. An even higher increase in the RI contrast will not result in an increased diffraction efficiency, but instead the main Bragg peak will split into two peaks. This marks the beginning of the so-called regime of transition ($\Delta n = [0.16 - 0.22[$). The highest considered RI difference was the one for the uninfiltrated sample ($\Delta n = 0.52$). For this case no interpretation in terms of a kinematic Bragg peak is possible.

Δn	Scattering regime	Description
0.005	Kinematic	Bragg peak & Diffraction efficiency
$0.01 - 0.15$	Quasi-kinematic	Bragg peak & Intensity increase
$0.16 - 0.22$	Transition	Bragg peak splitting & Const. diffraction efficiency
0.5	Dynamic	No Bragg peak

Tab. 6.3.: Subdivision into scattering regimes.

Interpreting the results for the kinematic and quasi-kinematic regime can be done by a comparison with the already developed approximation methods for low contrast. The kinematic approximation is well-known from the 'X-ray community', as well as the corresponding approximation in the field of optics. During this work it was shown that this approximation is valid in the case of light scattering from WP PCs. The more interesting interpretation

is the approximative approach concerning the transition from a kinematic regime to a 'dynamic' regime which means in this case that considerably more than one Fourier component will contribute to the scattered intensity in the respective scattering order. This influence can be well understood by considering band structures for different RI differences. For computational reasons the rods of the WP structure were implemented with a variation in the RI instead of variation of the RI of the space in between the rods. In figure 6.24 the effect
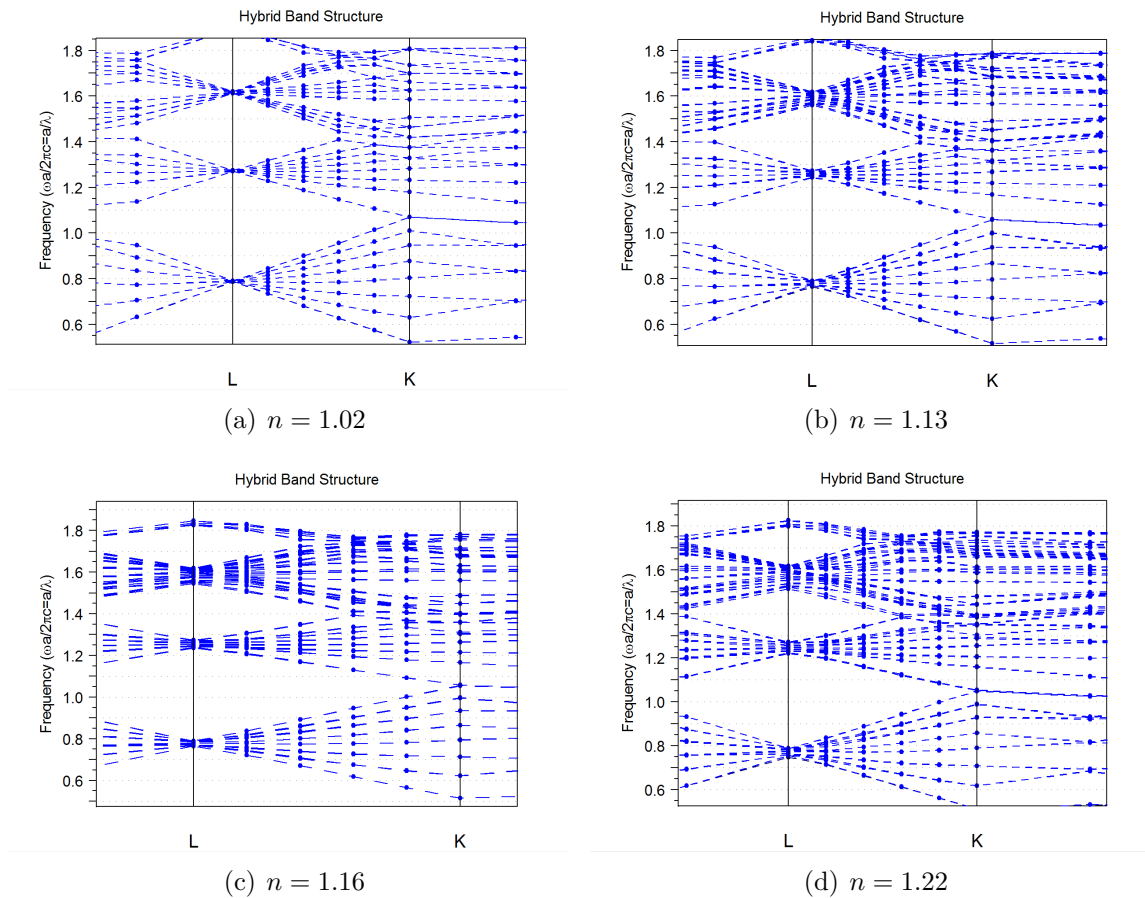

(a) $n = 1.02$ (b) $n = 1.13$

(c) $n = 1.16$ (d) $n = 1.22$

Fig. 6.24.: Development of the band structure for increasing RI. Ranges have been chosen in such a way to compare to the experimental results. The considered path is given by $\Gamma L K \Gamma$ (cf. figure 2.1(c)). The band splitting is especially visible at the important L point.

of splitting of bands is visible. The considered path is given by $\Gamma L K \Gamma$. The splitting of the bands is especially visible close to the L point. This results in a stronger coupling of the Fourier coefficients which causes at some point an increasing invalidity of the Bragg condition. Moreover, it is not only the coupling of the different Fourier coefficients, but an increase of Fourier coefficients other than the one responsible for the Bragg peak.

The calculations of the band structures are supposed to emphasize the previous statements qualitatively. However, they should not be viewed as an exclusive argument. The exact

mechanism of transfer of intensities between the Fourier coefficients is primarily intelligible via the RCWA or transfer matrix approach. Unfortunately, due to the usage of a commercial product this mechanism is not accessible.

6.2.7. Dispersive properties of WP PCs

The polychromatic laser was used to investigate the dispersive properties of the WP PC. Due to the limited size in stacking direction a classic Laue picture cannot be expected. The diffraction pattern itself resembles more the one of a 2D grating. In order to demonstrate the dispersive properties the $(02)T$ reflection was chosen over the $(01)T$ reflection because the Bragg peak structure for lower contrast has a more pronounced effect in the dispersive properties. Few contrasts have been chosen for a qualitative analysis. In figure 6.25 the reflection is shown for a maximum refractive index contrast of $\Delta n = 0.52$ while in figure 6.26 a contrast of $\Delta n = 0.19$, in figure 6.27 a contrast of $\Delta n = 0.13$ and in figure 6.28 a contrast of $\Delta n = 0.06$ is depicted.

All reflections show a rainbow-like broadening of the Bragg peak which was already expected because of the limited size in stacking direction. Moreover, the reflection of the uninfiltrated sample indicates a vertically broadened reflection and more importantly the reflection is not strictly split into a rainbow structure but shows a random colour distribution. This is understood by taking a look at the monochromatic reflection which also does not have any distinct Bragg beak.

The reflections for the infiltrated state show on the other hand a clear Bragg peak with a broadly-coloured $(\Delta\lambda)$ intensity distribution. Although the camera does not give a linear response in the intensity distribution it can be clearly seen that the diffracted intensity decreases for decreasing contrast while the broadness of the peak is not affected by the refractive contrast. This confirms the monochromatic measurements.
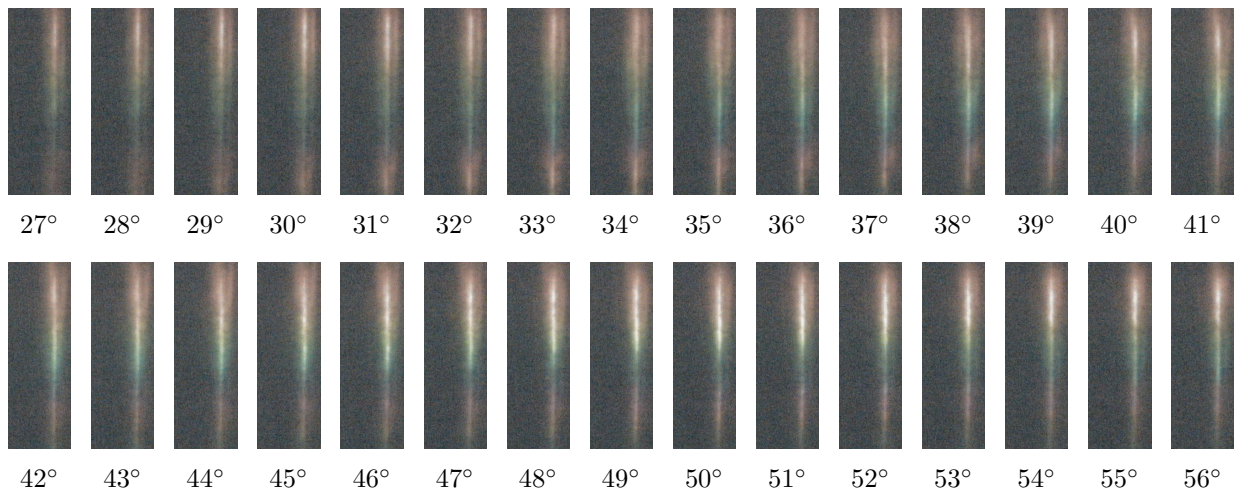
27° 28° 29° 30° 31° 32° 33° 34° 35° 36° 37° 38° 39° 40° 41°

42° 43° 44° 45° 46° 47° 48° 49° 50° 51° 52° 53° 54° 55° 56°

Fig. 6.25.: $(02)T$ Reflection of sample B without infiltrated liquid.

27° 28° 29° 30° 31° 32° 33° 34° 35° 36° 37° 38° 39° 40° 41°

42° 43° 44° 45° 46° 47° 48° 49° 50° 51° 52° 53° 54° 55° 56°

Fig. 6.26.: $(02)T$ Reflection of sample B with $n_{\mathrm{Liq}} = 1.33$

27° 28° 29° 30° 31° 32° 33° 34° 35° 36° 37° 38° 39° 40° 41°

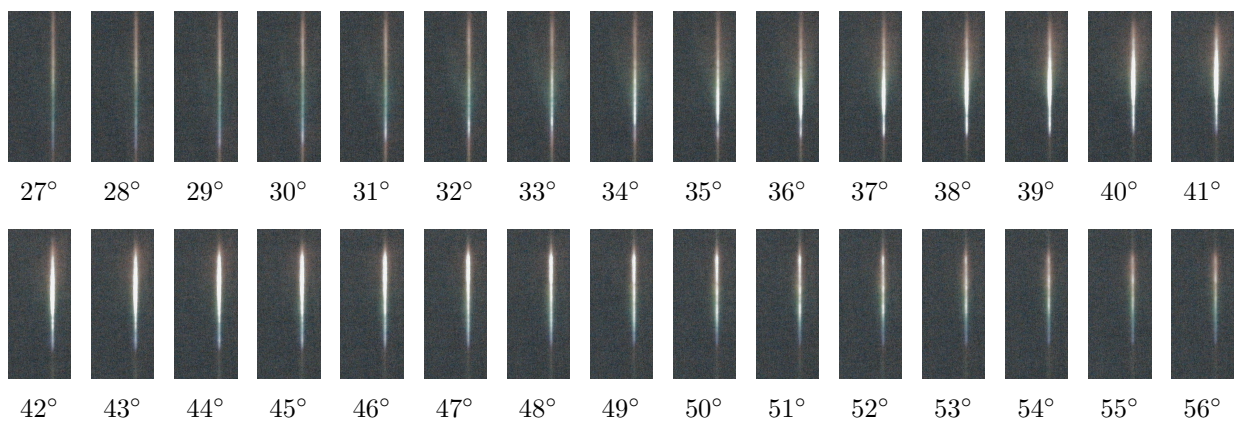42° 43° 44° 45° 46° 47° 48° 49° 50° 51° 52° 53° 54° 55° 56°
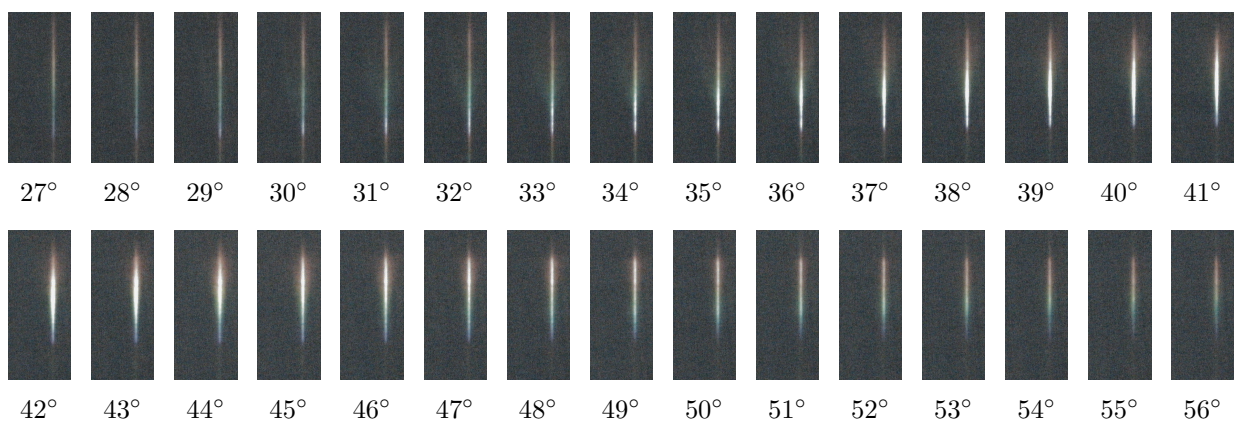
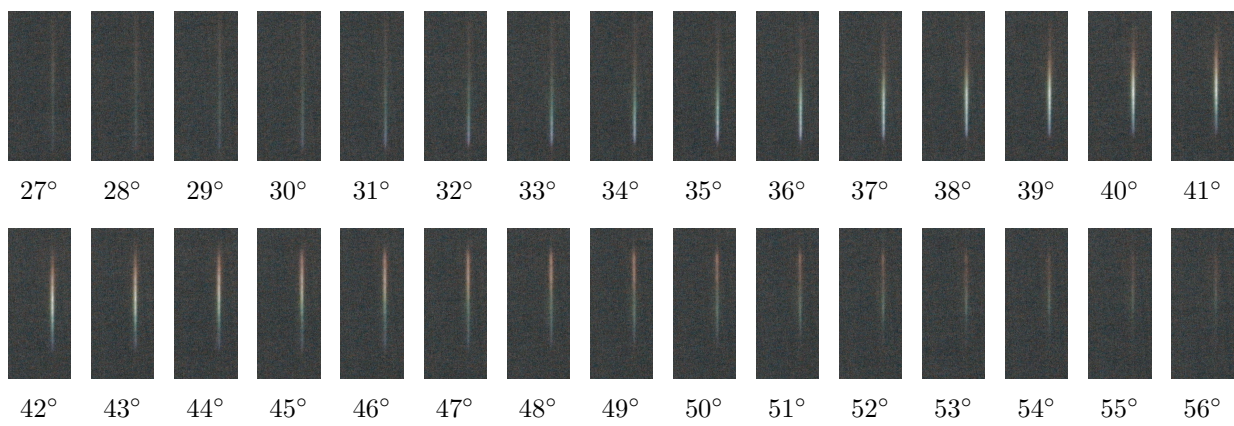**Fig. 6.27.:** $(02)T$ Reflection of sample B with $n_{\mathrm{Liq}} = 1.39$

Fig. 6.28.: $(02)T$ Reflection of Sample B with $n_{\text{Liq}} = 1.46$

7. Holographic Phase Lattices

The creation process of the three-dimensional phase lattices has been described in 1.2. The crucial part in this process is the light interaction with the used polymer. The structures investigated in this thesis have been inscribed in three different polymers. Two of these polymers are commercially available products while the third one was developed during the project with the aim to tailor it in such a way that its properties match the needs for the special applications they were intended for. That is why in the following sections the analysis of the light scattering will be done for each polymer separately and in the end a short comparison will be given.

7.1. InPhase

The first set of photonic lattices was inscribed into a polymer which is a product from InPhase Technologies (*InPhase Tapestry 59377*). Although this photo polymer was originally intended for the use in the framework of holographic data storage, it was used in this case as a base material for phase lattices intended for diffractive-optical applications.

The photo polymer itself is sandwiched between two glass plates which have the function of substrates. The glass substrates have a square shape of $5 \times 5 \text{cm}^2$. In this large area multiple lattices are inscribed with partly varying parameters. The positions of these lattices can be envisioned as an array with columns and rows of equidistant spacings.

The different parameters which have the most influence on the scattering process have been summarized in table 7.1. These are essentially the lattice parameters which allow the subdivision into two types of lattices. Each phase lattice located on the glass plate has

	Lattice constant a	Lattice constant c
Type 1	$1.12\mu\text{m}$	$8.91\mu\text{m}$
Type 2	$2.03\mu\text{m}$	$30.43\mu\text{m}$

Tab. 7.1.: Parameters given by the sample producers as predesign specification.

a diameter of a few millimetres. The extension is directly related to the radiation dose

the photo polymer is exposed to. If the radiation dose is too high, the polymer can be overexposed resulting in a destruction of the lattice.

7.1.1. Structure determination and confirmation

Firstly, several experiments were done to confirm the crystallographic structure. Chapter 1.2 discussed the fabrication of these kinds of lattices. According to that the structure should be trigonal. But since this set of samples was the first one created, confirmation of the structure is necessary. The most convenient way of structure determination is the Laue experiment. In figure 7.1 the diffraction pattern of such an experiment is depicted. In contrast to the classic Laue case, in this case the incident beam is monochromatic. Nevertheless, spots appear on the screen that stem from diffracted laser light. From the symmetry in the diffraction picture one can easily conclude that the structure is trigonal (cf. figure 3.1(b)). The Laue diffraction pattern with polychromatic light showed the same symmetry as the
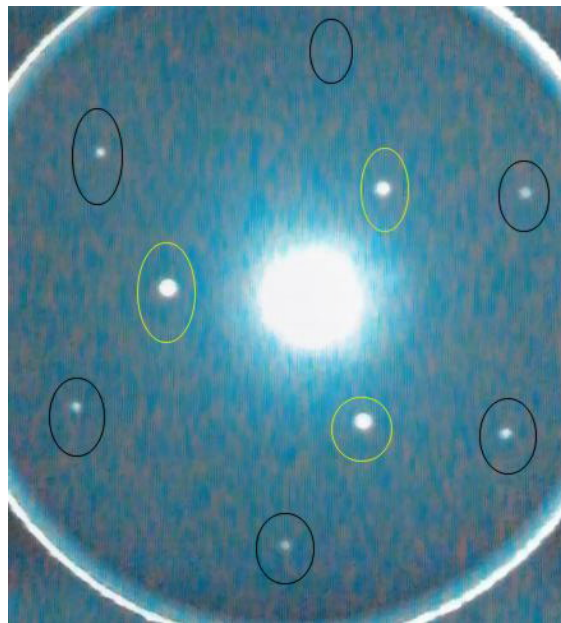

Fig. 7.1.: Diffraction pattern of the type 2 PC in transmission geometry. The incoming monochromatic beam ($\lambda = 488$ nm) is aligned parallel to the surface normal of the glass substrate. The large spot in the centre represents the non-diffracted beam. The yellow encircled spots correspond to the first order diffracted beams while the black encircled spots correspond to the second order diffracted beams.

aforementioned one. The special properties of the polychromatic case will be presented later when the dispersive properties of the photonic lattice are discussed.

Next to the qualitative determination of the symmetry, a quantitative analysis of the scattering properties of the photonic lattice can give preciser pieces of information about

the structure. From the exact knowledge of the position of the diffraction spots, the in-plane lattice constant a can be determined. The following equation, already derived in (3.4), explains the connection between the incident angle $-\omega$, the diffracted angle θ and the corresponding in-plane lattice spacing $d(\mathbf{G}_\parallel)$:

$$\theta(\omega) = \arcsin\left(-\sin(\omega) + \frac{\lambda}{d(\mathbf{G}_\parallel)}\right) - \omega \tag{7.1}$$

From the exact measurement of the angles ω and θ the lattice spacing is the only unknown variable and can therefore be calculated. As a reminder the well-known relation for hexagonal structures is given:

$$d(\mathbf{G}_\parallel) = d_{hk} = \frac{\sqrt{3}}{2}\frac{a}{\sqrt{h^2 + k^2 + h \cdot k}} \tag{7.2}$$

Since it is more convenient to use the hexagonal system for the trigonal structure one has to remember that not all possible reflections in the hexagonal system occur for a trigonal structure. h and k represent 2D - Miller indices. The different reflections with the same lattice spacing are summarized in table 7.2. The in-plane lattice constant a can be determined

Reflection	{10}	{11}	{20}	{22}	{30}
$d_{\{hk\}}$	$\frac{\sqrt{3}a}{2}$	$\frac{a}{2}$	$\frac{\sqrt{3}a}{4}$	$\frac{a}{4}$	$\frac{\sqrt{3}a}{6}$

Tab. 7.2.: Relation of 2D Miller indices and lattice spacing.

independently for each reflection. The mean value for each reflection is then given by the average:

$$\overline{d_{hk}} = \frac{1}{n}\sum_{\{h,k\}} d_{hk} \quad \text{n equals the number of peaks} \tag{7.3}$$

Hence, the mean value for the lattice constant is calculated as an average over all reflections. The results of this investigation are tabulated in table 7.3. From this table it is evident that the investigation was also done for light of different wavelength. The results indicate that the lattice constants a calculated from the measurement deviate by 11% for the type 2 photonic lattice from the inscribed parameters (cf. table 7.1) and by 8% for the type 1 photonic lattice. A deviation of this magnitude is realistic [66] because several aspects can influence the inscription process. Firstly, the chemistry inside the polymer is rather complex and therefore, it is possible that it can change after the creation of a photonic lattice. Furthermore, an error in the alignment of the laser beams can also have a direct influence on the crystal geometry. Nevertheless, it can be stated that this investigation has

confirmed the trigonality of the photonic lattice.

(a) Type 1 - Photonic Lattice

	$\overline{d_{\{10\}}}$	$\overline{d_{\{11\}}}$	$\overline{d_{\{20\}}}$	a
$\lambda = 488$nm	1.052	0.614	0.531	1.223
$\lambda = 568$nm	1.069	0.616	-	1.233
$\lambda = 647$nm	1.068	0.611	-	1.228

(b) Type 2 - Photonic Lattice

	$\overline{d_{\{10\}}}$	$\overline{d_{\{11\}}}$	$\overline{d_{\{20\}}}$	$\overline{d_{\{22\}}}$	$\overline{d_{\{30\}}}$	a
$\lambda = 488$nm	1.98	1.15	0.991	0.572	0.662	2.292
$\lambda = 568$nm	1.983	1.1466	0.987	0.573	0.662	2.289
$\lambda = 647$nm	1.993	1.147	0.988	-	0.661	2.292

Tab. 7.3.: Average values of the lattice spacing $\overline{d_{hk}}$ for different reflections (hk) and the overall average of the lattice constant a. All values are in μm.

7.1.2. Recording of the scattering curves

After confirming the crystal structure, the scattering properties of single reflections of the photonic lattices are investigated by employing the reflection scans described in (3.4). For the reflection scans the previously determined lattice spacings d_{hk} are used. The measurement of the scattering curves was done for nearly all available reflections. Due to the large diffraction efficiencies for several reflections a slit was used to avoid a saturation effect in the photo diode. Moreover, the reflection scans were recorded for the three wavelengths mentioned in table 7.3. Exemplary for these measurements three reflection scans for the same reflection are shown in figure 7.2. Several conclusions can be drawn from these scans. The first point
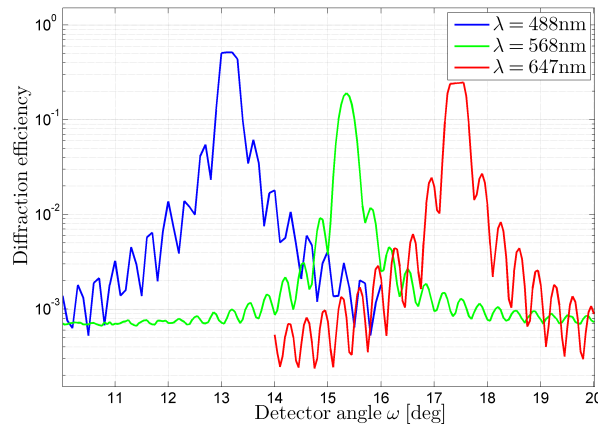

Fig. 7.2.: Scattering curves for three different wavelengths for the $(1-2)T$ reflection.

which is the Bragg peak shift for increasing wavelength is rather trivial. Issues related to the experimental setup are the obvious peak flattening for blue and red laser light, caused by a saturation of the photo diode although a slit was used, and a detector misalignment for the green light. Furthermore, the difference in magnitude of the scattering efficiency of the main Bragg peak and the side fringes are remarkable. That is why a logarithmic depiction of the scattering efficiency was chosen. Moreover, the fringes were quite narrow in angular space, so initially the step size of the scan for the blue light was chosen too large. It has been tried to minimize all these experimental error sources for the scans of the other reflections that will be discussed later on.
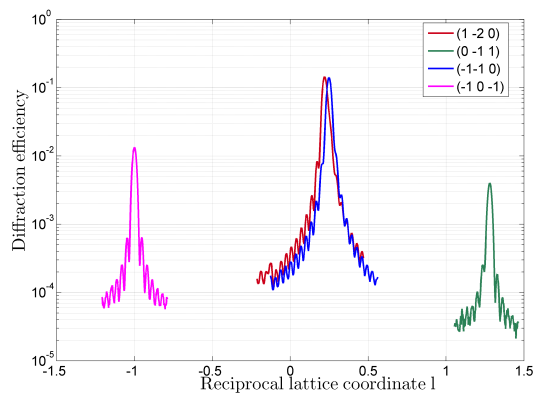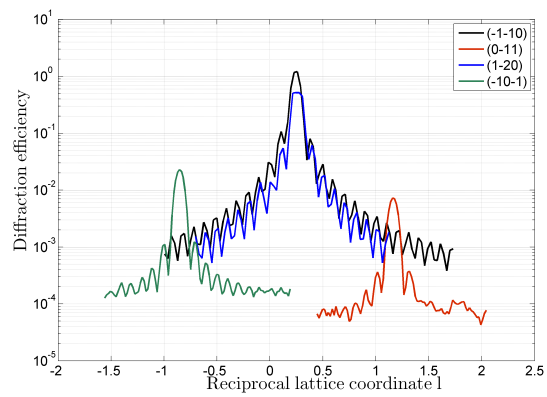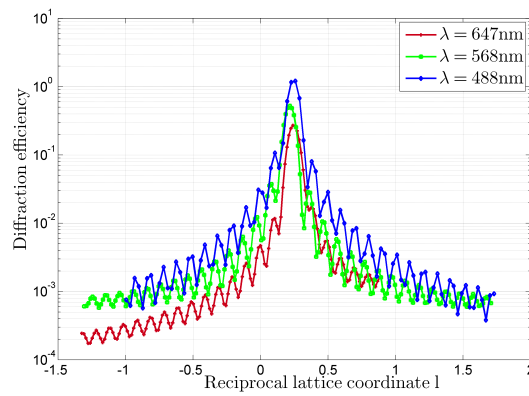
7.1.3. Transfer to reciprocal space

After performing the scans the transfer to reciprocal space gives a deeper insight into the scattering properties of the photonic lattice. The transfer was done by employing (3.6). A few selected scans are plotted in figure 7.3. In this case the last Miller index always represents the l-value closest to the main Bragg peak. At this point one has to be keep in mind that the hexagonal Miller indices are used and for a trigonal structure not all possible combinations of the (hkl) values are allowed. The selection rule is given by:

$$-h + k + l = 3 \cdot n \quad \text{with} \quad n \quad \text{being an integer} \tag{7.4}$$

The scans show major differences in the measured diffraction efficiency (the scale is logarithmic). The so-called 'uneven' diffraction orders which are given by the set of reflections symmetric to $\{-1-10\}$ show a much larger scattering efficiency (1 to 2 orders of magnitude) than the set of reflections symmetric to $\{-10-1\}$. The second order reflections ($\{20\}$ in 2D indices) that have been utilized in the previous section for structure determination have an even more than three magnitudes lesser efficiency than the $(-1-10)$ reflection. Furthermore, with decreasing diffraction efficiency the typically visible side fringes have too little intensity to be detected by the photo diode. From the transfer to the reciprocal space it can already be seen that the Bragg peaks are not positioned at the expected l-coordinates, but are mostly shifted to more positive values. Additionally, it can be stated that the transfer for different wavelengths shows the same results so that this can be viewed as a wavelength-independent offset.

7.1.4. Analysis of the scattering curves

A major difference of the holographic photonic lattices with other photonic crystals is the sinusoidality of the permittivity distribution. The creation of 1D-sinusoidal lattices (slanted

(a) Type 1 - photonic lattice - $\lambda = 568$nm

(b) Type 2 - photonic lattice - $\lambda = 488$nm

(c) Type 2 - photonic lattice - $(-1-10)$ reflection

Fig. 7.3.: Scattering curves transferred to reciprocal space for different reflections of the two types of holographic photonic lattices.

or unslanted) is already well-known [14], [67] and the interaction of light with them, too [68]. For the 3D case a rigorous analysis was recently done [15]. The sinusoidal permittivity distribution is the key to understand the diffraction properties of these kinds of lattices. Despite the low RI contrast ($\Delta n \approx 10^{-3}$) the diffraction efficiencies for certain reflections are rather high (up to 80%). To explain this one needs to know that the scattered intensity can be expressed as a Fourier transform of the permittivity distribution. Knowing that the Fourier transform of a single sine-function is only one single δ-function, one can conclude that for 3D lattices with a sinusoidal modulation in three independent directions the scattered intensity is only non-zero for three reflections corresponding to the three δ-functions. The experiments, however, clearly indicate multiple non-vanishing diffraction orders. For the currently considered sample set this means theoretically that besides the diffraction order corresponding to $\{-10-1\}$ no other diffraction orders should have any intensity. The deviation of experiment and theory can be explained by considering multiple factors:

1. The photonic lattice has a limited size in c-direction and moreover only few periods, therefore the condition for diffraction is softened resulting in the side fringes next to the Bragg peak.

2. The fabrication of the sample is strongly affected by the alignment of the inscribing lasers and especially the polarization to each other. This can result in an asymmetry of the modulation of the sine-functions which explains the difference in the scattering efficiency for symmetric reflections.

3. The most striking point is the much larger intensity of the $\{-1-10\}$ reflections which has to be caused by a more general error in the sample fabrication. The permittivity distribution has to be modulated asymmetrically and in such a way that the Fourier transform favours this set of reflections.

Modelling the scattered intensity can be done by employing methods of general electrodynamics. This means the numerical solution of Maxwell's equations. In an earlier section the RCWA which is a favourable tool for modelling was introduced. A comparison of RCWA modelled curves with the measured data has been done extensively in [15]. Here, the simple approach and well-known kinematic model is used as a tool to analyse the data.

The basic approach results in a contribution of the scattered signal into two parts. The lattice sum and the unit cell structure factor. The latter one can be decomposed into a structure sum and an 'atomic' factor which refers to the scattering from the smallest possible constituent. The lattice sum is usually approximated by the well-known Laue function for small crystals while the structure sum considers the trigonal arrangement of the unit cell (in our case, a hexagonal unit cell with ABC stacking). The 'atomic' factor should be

approximated by the Fourier transform of a sine function. This model is summarized in (7.5) with the corresponding factors given in (7.6), (7.7) and (7.8).

$$I \propto a \cdot (F_{\text{Lattice}} \cdot F_{\text{Structure}} \cdot F_{\text{Atom}})^2 \tag{7.5}$$

However, the already mentioned problems might give a hint that several adjustments have to be made to the model to yield agreeable results. This is mainly due to the fact that reflections with lesser intensity do not show the typical $\left| \frac{\sin(x)}{x} \right|^2$ envelope which corresponds to an approximation of the mentioned δ-function (cf. (7.7)).

$$F_{\text{Lattice}} = \frac{\sin(N_c \cdot B \cdot \pi \cdot (l - l_0))}{N_c \cdot \sin(B \cdot \pi \cdot (l - l_0))} \tag{7.6}$$

$$F_{\text{Atom}} = \frac{\sin[2\pi g_0 (l - l_0)]}{\pi (l - l_0)} \tag{7.7}$$

$$F_{\text{Structure}} = \left| 1 + \exp\left(2\pi i \left(\frac{2}{3} h + \frac{1}{3} k + \frac{1}{3} B \cdot (l - l_0) \right) \right) + \right.$$
$$\left. + \exp\left(2\pi i \left(\frac{1}{3} h - \frac{2}{3} k + \frac{2}{3} \cdot B \cdot (l - l_0) \right) \right) \right| \tag{7.8}$$

The results of the fit parameters for this model are shown in table 7.4 (type 2). The values where $g_0 = 0$ correspond to fits where the respective term was omitted. Therefore, a lot of reflections are mentioned twice in the table. It is evident that the assumed model gives only partially good results, the vast majority of reflections is influenced by the missing intensity. This is also why several times the fits indicate a different l_0 value as the obvious value from the experiment. The values for the type 1 photonic lattice deviate comparably and are not listed here. The goodness of the fit was also determined. In this case the adjusted R^2 value is not that meaningful since the fit of the main Bragg peak is the most dominant factor in its determination and that is always fitted very well, whereas the deviations in the side fringes do not contribute much to its value. As an example two fits are shown in 7.4. The diffraction efficiency is plotted linear in order to show the significance of the Bragg peak compared to the side fringes.

7.1.5. Improvements in sample fabrication

The earlier achieved results contributed to an optimization of the sample production. The sample was again inscribed into the same InPhase photo polymer (*InPhase Tapestry 59378*) with parameters that result in an in-plane and out-of-plane lattice constant that is equal to the Type 1 photonic lattice. In order to distinguish it from the previous one the new sample set is therefore called ***Type 1b***. The scattering curves from the corresponding sample (cf.

Refl.	B	ΔB	I_0	ΔI_0	l_0	Δl_0	g_0	Δg_0	R^2
(0-11)	0.68	0.02	0.027	0.026	2.38	0	0.27	0.134	0.99
(01-1)	0.65	0.02	0.009	0.02	-1.48	0.01	0.45	0.497	0.99
(-1-10)	0.64	0.02	0.899	0.127	2.23	0	0.6	0.047	1
(0-11)	0.68	0.01	0.001	0	0.92	0.03	0	0	0.99
(01-1)	0.69	0.05	0.008	0.012	0.95	0.17	0	0	-0.21
(-1-10)	0.67	0.01	0.127	0.038	0.76	0.03	0	0	0.28
(1-20)	0.51	0.03	0.168	0.01	0.29	0.11	0	0	0.95
(1-1-1)	0.59	0	0.007	0	1.02	0.01	0	0	0.98
(-1-10)	0.52	0.03	4.049	21.545	2.27	0.01	0.19	0.507	0.96
(1-1-1)	0.65	0.01	0.047	0.007	-0.67	0	0.35	0.025	1
(0-11)	0.61	0	0.004	0.001	2.48	0	0.78	0.065	1
(-1-10)	0.64	0.01	0.364	0.028	2.5	0	0.6	0.024	1
(0-11)	0.63	0	0.001	0	0.89	0.01	0	0	1
(-1-10)	0.66	0.01	0.053	0.011	1	0.02	0	0	0.29
(1-20)	0.67	0.01	0.02	0.004	1.13	0.02	0	0	0.29
(1-1-1)	0.65	0.01	0.003	0	0.98	0.02	0	0	1
(1-20)	0.62	0	0.559	0.034	2.65	0	0.29	0.007	1
(0-11)	0.61	0.01	0.002	0.001	2.61	0	0.91	0.222	1
(-1-10)	0.6	0.01	1.104	0.585	2.87	0	0.25	0.068	1
(0-11)	0.63	0.01	0.001	0	1.02	0.01	0	0	1
(-1-10)	0.65	0.01	0.109	0.03	1.74	0.03	0	0	0.17
(1-20)	0.51	0.02	0.08	0.003	0.99	0.06	0	0	0.96
(1-1-1)	0.67	0.01	0.003	0	1.06	0.01	0	0	0.99
(1-20)	0.6	0.01	1.292	1.324	2.98	0	0.27	0.138	0.99
(1-1-1)	0.76	0.03	0.035	0.047	-0.42	0.01	0.25	0.167	0.94

Tab. 7.4.: The fit parameters are shown for the corresponding reflections. The colour of the reflection indicates the used wavelength. For $g_0 = 0$ the fit was used without this parameter. The type 2 photonic lattice was considered here.
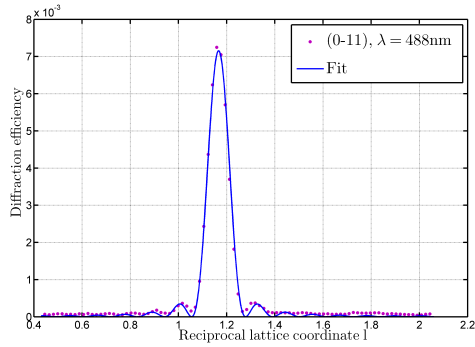
(a) Type 2 - photonic lattice - $\lambda = 488$nm
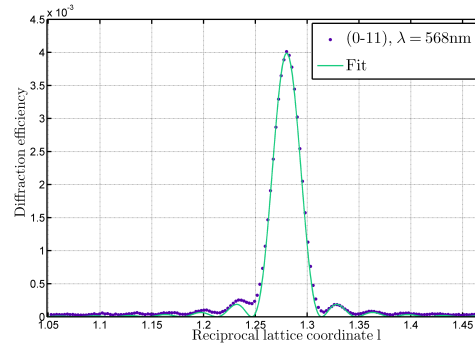
(b) Type 1 - photonic lattice - $\lambda = 568$nm

Fig. 7.4.: Kinematic fits for both types of samples.

figure 7.5) show a behaviour which is different from the first generation of samples. Here, the scattering efficiency is much larger for the first-order diffracted beams ($l = \pm 1$) than for the mixed ($l = 0$)-order peaks. It is furthemore significant that there is a deviation from the measured peak position to the predicted one, especially for $l = 0$. Another observable issue is the change in the diffraction efficiency in the symmetric diffraction orders. The
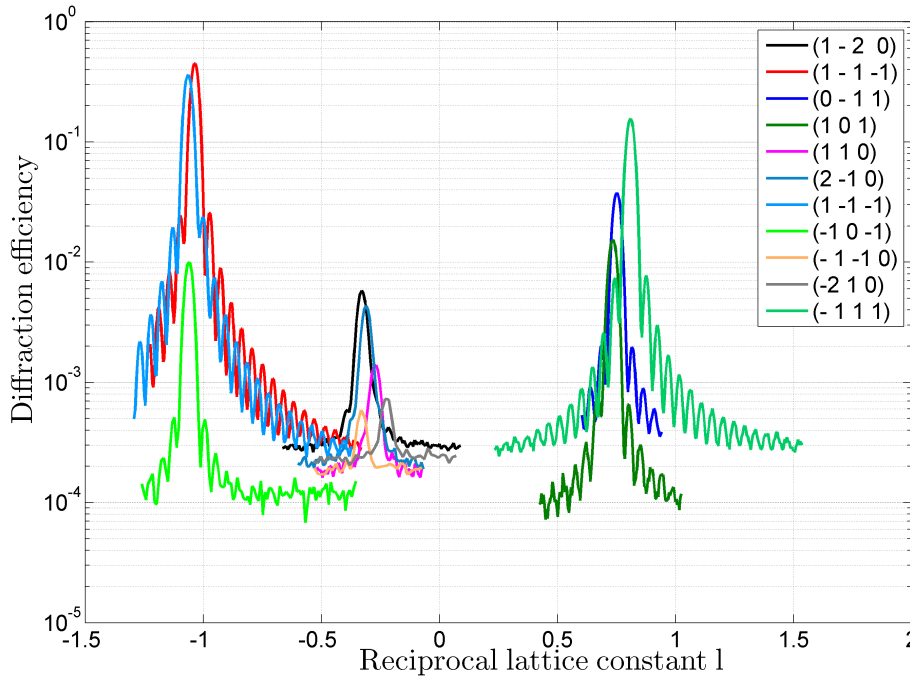

Fig. 7.5.: Scattering curves for *Type 1b* photonic lattice with a probing wavelength of $\lambda = 488nm$.

reason for this can on the one hand still be found in the crucial polarization dependence of the inscribing beams which means that contrasts in certain directions of the polymer are higher than in other directions. On the other hand, slight misalignments can also cause lesser diffraction efficiencies. This is visible for scans where the peak maximum is shifted in reciprocal space.

The latter point is due to the very sharp Bragg peaks in angular space. This necessitates an adjustment of the scattering parameters for each measured Bragg peak because the experimental Bragg condition does not always correspond to the values expected from the inscription process. Due to the peak sharpness, deviations of around one thousandth of a degree can cause a drop of the scattering efficiency up to 50%.

The scattering curves were again analysed by a kinematic fit model. This time the structure factor was omitted to limit the number of parameters. The effect on the general model is negligible since the influence of this factor proved to be of lesser importance for this type of photonic structures. From the results of the kinematic fit model (cf. table 7.5) one can

Refl.	B	ΔB	I_0	ΔI_0	l_0	Δl_0	g_0	Δg_0	R^2
(0-11)	1.38	0.01	0.099	0.816	1.69	0	0.31	1.275	0.997
(1-1-1)	1.46	0	0.223	0.022	-1.03	0	0.71	0.034	0.999
(01-1)	1.39	0.01	0.197	0.028	-1.04	0	0.68	0.049	0.998
(101)	1.31	0.01	0.019	0.024	1.68	0	0.44	0.27	0.998
(-111)	1.3	0	0.099	0.004	1.82	0	0.63	0.014	0.999
(-10-1)	1.39	0.02	0.007	0.001	-1.05	0	0.62	0.029	0.996

Tab. 7.5.: The fit parameters are shown for the corresponding reflections. The structure factor was not considered in this case. ($\lambda = 488$nm)

conclude that the diffraction curves can be explained by this simple approach to some extent. The adjusted R^2 value shows that most of the deviations of this model can be accounted for. However, several points have to be considered when studying the results. Firstly, the fit is dominated by the strength of the Bragg peak. Secondly, the fewer the number of side fringes measured the larger the error in the function of the envelope model described by the fit parameter g_0. Due to the addition of the previously mentioned function the interpretation of the other parameters has to be changed and they cannot be compared to the classical kinematic model, i.e. I_0 does not give the diffraction efficiency directly. For this a deconvolution of the results is necessary.

7.1.6. Dispersive properties

Previous experiments were done monochromatically with selected wavelengths from the Ar-Kr multi-modal laser. However, the classic Laue experiment necessitates white light incident upon a three-dimensional crystal-like structure. Thus, the pulsed fibre laser was used as a
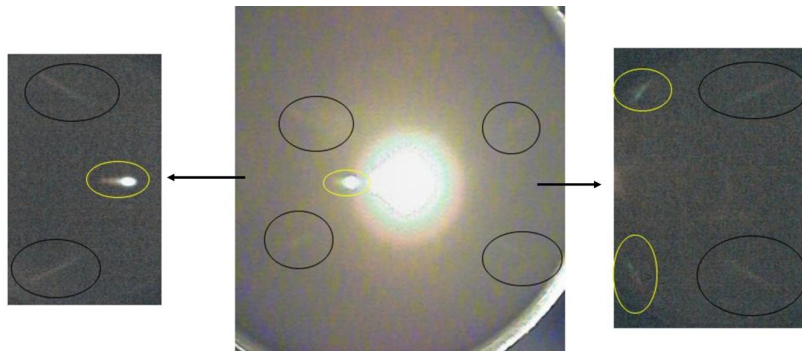

Fig. 7.6.: Shown here is a transmission picture ($\omega = 0°$) of the type 2 photonic lattice for white laser light. The intense spot in the center is the non-diffracted beam. The diffracted beams can hardly be recognized and for better visualization the spots are shown to the left and to the right again.

source of coherent white light. Unlike the classic Laue experiment where several sharp

diffraction spots are expected which correspond to diffraction of light of special wavelengths, for the type of photonic lattices considered here this is not the case. In figure 7.6 the corresponding white light diffraction for photonic lattices is shown. From that picture it is very clear that the diffracted spots are broadened over almost the whole light spectrum. The intensity is distributed in such a way that at a certain wavelength a maximum occurs while the intensity of the other wavelengths is suppressed. The size of this suppression depends on the considered reflection and especially on the general diffraction efficiency of the peak.
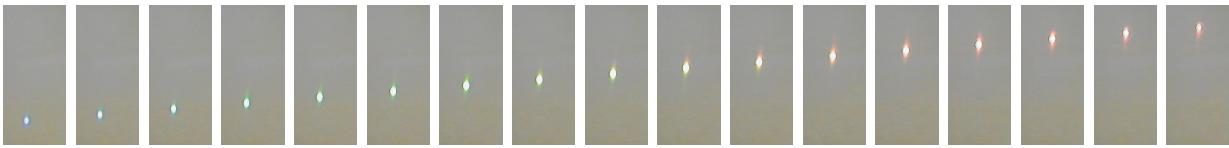
(a) Single reflection of the Type 1 photonic lattice.
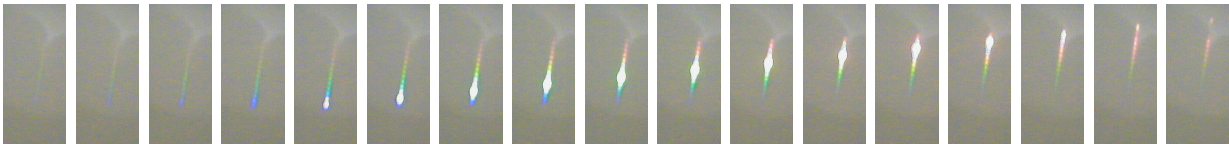
(b) Single reflection of the Type 2 photonic lattice.

Fig. 7.7.: Selected reflections of the type 1 and 2 photonic lattices. For frames at the very left the lowest possible angles were chosen where the diffracted beam became visible on the screen. The adjacent frames to the right were recorded when increasing the incident beam angle. The step size is not larger than $\Delta\omega = 0.1°$.

In order to investigate the angle-dependent behaviour of the scattering peaks, single reflections were chosen and observed while changing the incident angle. For two reflections this is depicted in figure 7.7. For a weaker reflection the change in position and in the colour of the spot can be observed. For a stronger reflection the most instense spot appears white due to the insensitivity of the recording camera, although the colour and position of this spot changes similarly to the first case. The important point for this reflection is to observe the vicinity of the Bragg peak. Clearly visible are diffracted signals not corresponding to the wavelength of the Bragg condition. This broadening $\Delta\lambda$ can be explained by the limited thickness of the photo polymer and is theoretically and experimentally well-known for the 1D case [48]. For the 3D case this was also studied in [15].

7.2. Aprilis

Another set of photonic lattices was inscribed into a different commercial photo polymer (*Aprilis Holographic Media Card E-type*). The 300μm thick photo polymer was sandwiched between two 0.6mm thick glass plates. The designated use of this kind of polymer is for

the holographic data storage. However, a usage for the creation of photonic lattices is also possible. The sensitivity of the photo polymer for lattice creation is especially high for a wavelength of the inscribing beams of around 405nm. The maximum refractive index modulation for the inscribed photonic lattices should be around $\Delta n = 5 \cdot 10^{-4}$ for $\lambda = 405$nm. The exact value of the refractive index was not given by the polymer manufacturer but was expected to be in the range of $n = 1.5$ to 1.6 [15].

7.2.1. Sample fabrication

The three-dimensional photonic lattices that were inscribed into the polymer differ in their creation process. The lattice created with the same technique like for the previously described InPhase material is further referred to as *Aprilis-1* photonic lattice. Other lattices were not created by this multi-beam interference technique but by a technique widely known as multiplexing. This means that instead of four interfering beams only two beams interfere and create a 1D lattice. By extreme precise rotation of the sample table of 120° around the normal of the glass substrate another two 1D lattices are inscribed. Effectively, the final inscribed structure resembles a 3D photonic lattice of hexagonal structure. Such kinds of lattices are referred to as *Aprilis-2* photonic lattice. The exact configuration of the inscribing beams are given in table 7.6. For the *Aprilis-1* sample all four beams *abcd* from table 7.6

Angle	Beam a	Beam b	Beam c	Beam d
θ	13.7°	13.7°	0°	13.7°
ϕ	120°	0°	0°	240°

Tab. 7.6.: Parameters of the lattice creation process. For angle definitions see chapter 1.2.2.

were used simultaneously while for *Aprilis-2* sample the beam pairs $ac + bc + dc$ were used sequentially. This beam configuration results in a lattice with an in-plane lattice constant of around $a = 1.97\mu$m. This was calculated by assuming a recording wavelength of 405nm and an average refractive index of the Aprilis polymer of $n = 1.6$. The c/a-ratio is given by 7.2 resulting in an out-of-plane lattice constant of $c = 14.24\mu$m.

7.2.2. Laue experiments

A classic Laue experiment was performed to confirm the structure of the sample. The *Aprilis-1* sample shows a clear trigonal structure under illumination of blue laser light (cf. figure 7.8). In contrast to the previous sample, there are circular rings visible in the diffraction pattern. They can be interpreted as unwanted side effects of the sample creation. Significant for the trigonal structure are the three symmteric spots around the central beam, as well

as the six weaker spots arranged in a hexagon which represent the mixed-order diffracted beams. Furthermore, weak spots are visible at positions located at the horizontally mirrored positions of the first-order diffracted beams. This, combined with the polychromatic Laue picture which shows spots having a rainbow-like pattern, indicates a larger $\Delta\lambda$ for the Bragg condition.
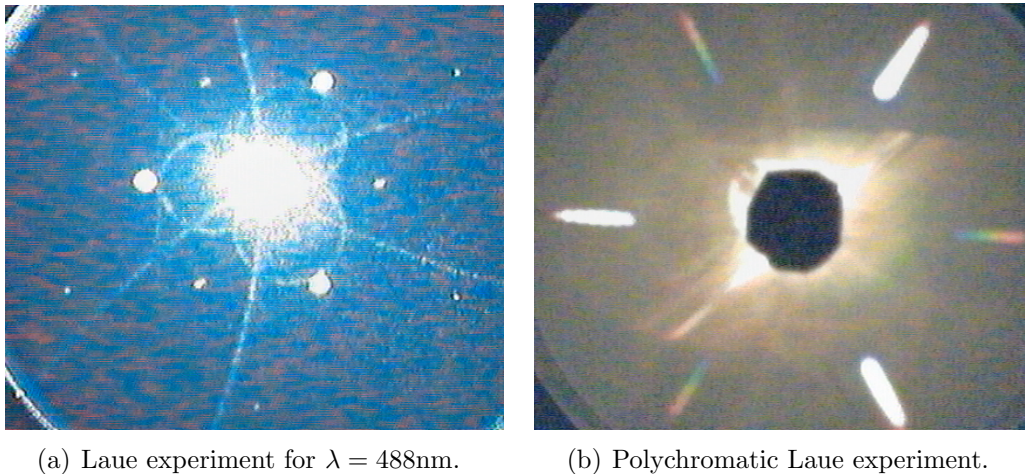

(a) Laue experiment for $\lambda = 488$nm.   (b) Polychromatic Laue experiment.

Fig. 7.8.: Polychromatic and monochromatic Laue experiments of the *Aprilis-1* sample. For the polychromatic case the primary non-diffracted beam was blocked in order to emphasize the diffracted beams.

7.2.3. Scattering Curves

Next to the qualitative interpretation made by the Laue experiments the intensities of several diffracted beams were analysed as a function of the incident angle. After the scans of the intense reflections were recorded they were transferred to reciprocal space with the same methods described earlier. Those reflection scans have been compiled in figure 7.9. Several important points can already be concluded by regarding the measurements. Firstly, the difference in the available reflections for the two types of photonic lattices can be directly seen. The missing reflections for the *Aprilis-2* sample have negligible intensity and were not recorded. For the *Aprilis-1* sample the mixed-order reflections have a comparable intensity like the first-order reflections. Secondly, the diffraction efficiencies for the Bragg peaks of different reflections from the same order are of comparable magnitude. This gives a hint to the refractive index modulation. It can be concluded that for these samples the modulation is symmetric in its maximum contrast. This can be viewed as an improvement to the lattices fabricated in the *InPhase* polymer. However, it is not due to the polymer but rather due to an improved inscribing setup which takes into account issues like the polarization of the incoming beam properly. The third point is a slight asymmetry in the side fringes.
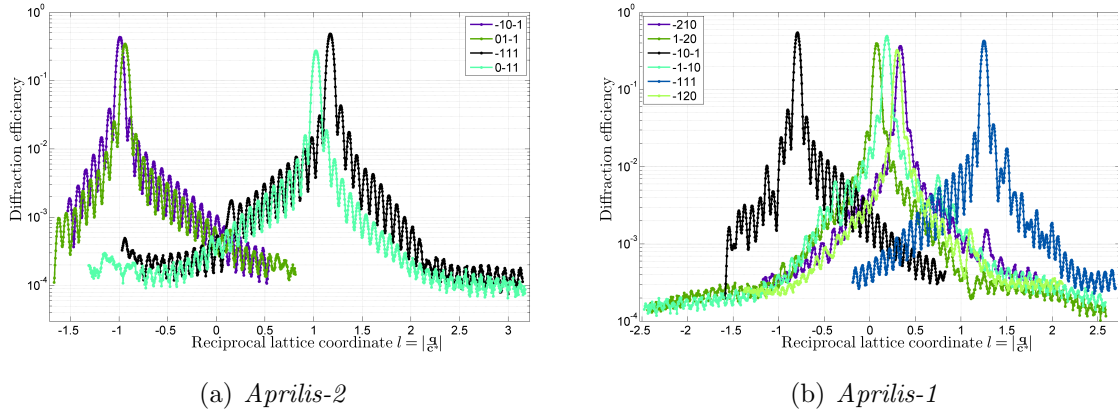
(a) *Aprilis-2*   (b) *Aprilis-1*

Fig. 7.9.: Scattering curves after transfer to reciprocal space recorded for a wavelength of $\lambda = 488$nm for both types of lattices.

7.2.4. Analysis

For interpreting the results a more simple model was used. It was found that a single sinc-function is sufficient to fit the diffraction efficiency [69]. The efficiency can be analytically expressed as:

$$I = I_0 \cdot \left(\frac{\sin\left(B\pi(l - l_0) \right)}{B\pi(l - l_0)} \right)^2 \tag{7.9}$$

This model has the advantage that the fit parameter I_0 directly yields the maximum diffraction efficiency while l_0 corrects for the considered reflection and furthermore indicates the deviation from the predicted value. The fit parameter B indicates the number of planes in stacking direction. Deviations from integer numbers can result in a different c-value as expected from the theoretical value. Experimentally, a shrinking of the polymer is possible and could be one explanation of such kind of deviations.

The difference to previously discussed models is the absence of terms related to the in-plane diffraction order (hk) and to the limited size of the crystal in stacking direction. Both terms have proved to be negligible in describing the scattered intensity. The cause for this is that the form factor variation is so small that it does not affect the scattered intensity much. Moreover, the structure factor plays a more important role for weaker reflections (cf. WP PCs), that is why it can be omitted for stronger reflections.

In table 7.7 the results of the fits for the Aprilis sample have been summarized. From the indexing of the reflections it is visible that reflections as well as their inverse counterparts have been measured, i.e. for the *Aprilis-2* sample the $(0 - 11)$ reflection was measured as well as the $(01 - 1)$ reflection.

(a) *Aprilis-2*

Refl.	B	ΔB	I_0	ΔI_0	l_0	Δl_0	R^2
(0-11)	12.41	0.04	0.274	0.001	1.023	0.001	0.998
(-111)	12.74	0.05	0.485	0.003	1.171	0.001	0.996
(-10-1)	12.75	0.08	0.435	0.003	-0.991	0.001	0.996
(01-1)	12.26	0.04	0.343	0.003	-0.939	0.002	0.998

(b) *Aprilis-1*

Refl.	B	ΔB	I_0	ΔI_0	l_0	Δl_0	R^2
(-10-1)	13.53	0.1	0.543	0.004	-0.796	0.002	0.992
(-111)	13.17	0.07	0.427	0.003	1.251	0.001	0.995
(-210)	11.45	0.09	0.36	0.004	0.335	0.003	0.990
(1-20)	11.61	0.07	0.393	0.003	0.075	0.003	0.993
(-1-10)	11.55	0.1	0.484	0.004	0.185	0.003	0.988
(-120)	11.34	0.08	0.32	0.003	0.299	0.003	0.993

Tab. 7.7.: Parameters of the fits to the experimental scattering curves recorded for the photonic lattices made of the Aprilis photo polymer.

The fits of the assumed model to the experimental data yielded agreeable results. The adjusted R^2 value was higher for all reflections than 0.98 indicating a good agreement. However, a closer look to the fit parameters reveals a deviation for the l_0 value from the theoretical value which should be given by $l_0 \in \{-1, 0, 1\}$ in this case. A deviation of $\Delta l \approx 0.32$ can be explained by a misalignment of the sample rotation angle by $\Delta \omega \approx 0.8°$ [69]. The angle-alignment was done by adjusting the substrate perpendicular to the incident beam. An error of $0.8°$ seems rather large, a value of $0.3° - 0.4°$ is more realistic. Nevertheless, adding a possible misalignment of the photonic lattice **c**-direction to the normal of the substrate of circa $0.1°$, the measurements can be considered to be within the experimental error. The experimental error should not be confused with the statistical error of the fits given in table 7.7. The determination of the scattering efficiency can be done considering the I_0 column. For the samples scattering efficiencies of more than 50% can be observed for selected reflections. Furthermore, the maximum diffraction efficiencies of the reflections vary by only a factor of two. This can be viewed as a big improvement in the sample production, compared to earlier results, since it can be concluded that the photonic lattices now have a maximum refractive index difference which is of the same order in all three dimensions which has already been qualitatively concluded in the previous section. The variation of the diffraction efficiencies for different reflections are not only due to the sample fabrication but can also be influenced by experimental factors. Those factors include especially a possible misalignment of angles in the Bragg condition which is quite likely due to the very sharp Bragg peak in angular space. A rough estimate of the error of the maximum diffraction efficiency therefore

yields a value of $10\% - 20\%$. Finally, the determination of the B-parameter can give a hint to the out-of-plane component of the photonic lattice. In order to interpret these values it is firstly necessary to take a look at the graphical depiction of the fits. In figure 7.10 a fit for the (0-11) reflection of the *Aprilis-2* photonic lattice was representatively chosen for discussion. On the one hand, it is clearly visible that the main Bragg peak is the most prominent feature in terms of diffraction efficiency and is therefore fitted very accurately. On the other hand, there is a visible discrepancy in the measured side fringes and the fitted
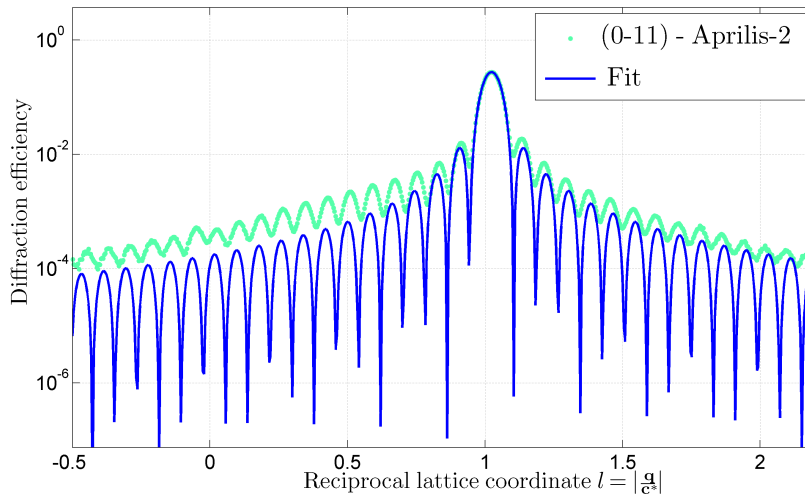
Fig. 7.10.: Fit to the experimental scattering curve of the (0-11)-reflection for $\lambda = 488$nm.

curve which is due to the lesser intensity. The effect of this fitting procedure is an obviously larger gap between neighbouring side maxima/minima which is better visible for higher order side peaks. Information about the out-of-plane component can be gathered from this gap. The simple assumption

$$\Delta l = \frac{\Delta q}{c^*} = \frac{c \cdot \Delta q}{2\pi} \tag{7.10}$$

with $\Delta q = \frac{2\pi}{d}$ where d stands for the thickness and Δl is the distance of two neighbouring peaks leads to:

$$d = \frac{c}{\Delta l} \tag{7.11}$$

The c-value for a refractive index of $n = 1.6$ was earlier calculated to be $c = 14.24\mu m$, for an external polar angle of $13.7°$. For the transfer to reciprocal space a refractive index of $n = 1.5$ was assumed, that is why either the values for Δl need to be properly adjusted or a different out-of-plane lattice parameter should be assumed. Instead of manually determining the gaps

to calculate d, one can use the fit parameter B which is a measure for this component. As a result one finds that $d = 248.3\mu$m for the *Aprilis-2* sample and $d = 239.7\mu$m for the *Aprilis-1* sample. Both values show a considerable smaller value than the 300μm given by the photo polymer fabricators, however the same argument as for the scattering intensity holds true and that is an estimated error of around 20% for the determination of the thickness. The reason for this is that a small misalignment in the angles can cause a scan that is not parallel to the c^*-direction in reciprocal space but has an inclination angle with this axis. Due to this the distance in reciprocal space of the side fringes appears larger. This explains that a smaller thickness of the polymer was determined.

7.3. NAMIROS

Aside from the commercially available photo polymers, one aim of the NAMIROS project was dedicated to the development of a unique photo polymer which should allow a better tailoring of the properties of the photonic lattices. In this part the first experiments with this newly-developed photo polymer are presented. The PCs inscribed into this photo polymer still have a sinusoidal RI modulation. In contrast to that one idea of the project was to develop a polymer that would have non-linear response to the inscribing laser beam pattern. However, up to now this has not yet been achieved, so the investigated PCs are expected to have a similar scattering behaviour.

7.3.1. Sample fabrication

The created photo polymer, still having a linear response, was alternatively illuminated by the already described multiplexing technique with a set of six beams (*Nam313*) as well as a simultaneous illumination of six beams (*Nam315*).

The geometry of the inscribing beams is listed in table 7.8. Compared to previous setups a central beam ($\theta = \phi = 0°$) is missing in this arrangement. Calculations by the sample

Angle	Beam a	Beam b	Beam c	Beam d	Beam e	Beam f
θ	7.5°	18°	7.5°	18°	7.5°	18°
ϕ	0°	0°	120°	120°	240°	240°

Tab. 7.8.: Parameters of the lattice creation process. For angle definitions see chapter 1.2.2.

fabricators yielded an in-plane (a) and out-of-plane (c) lattice constant equal to 5μm [70].

7.3.2. Qualitative Laue experiment for Nam315

The white light diffraction pattern of the multi-beam exposed photo polymer *Nam315* was recorded. In figure 7.11 Laue diffraction pictures for different incident angles are shown. Independently of the incident angle a vertical streak is visible across the screen. Very weakly diffracted beams appear at different positions on the screen for different incident angles hinting a low diffraction efficiency of the polymer. Due to both observations a subsequent recording and analysis of the scattering curves was left out and instead focus was directed to the sample *Nam313*.
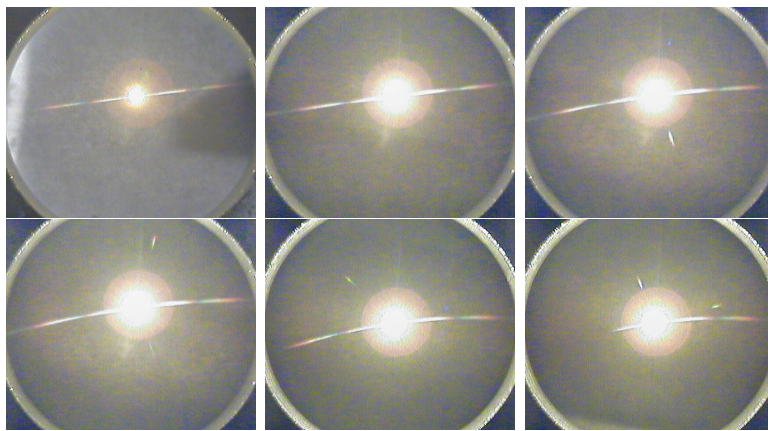
Fig. 7.11.: Laue diffraction pictures for different incident angles ω for *Nam315*. Clearly visible is a streak that goes through all pictures.

7.3.3. Qualitative Laue experiment for Nam313

The photonic lattice *Nam313* was created by the multiplexing technique. This means that not all six beams used for the creation process (cf. table 7.8) have been used simultaneously; instead three different beam pairs have been used sequentially. With this technique one-dimensional lattices are created and superposed so that the resulting lattices are again three-dimensional. Firstly, the photonic lattice was investigated by white light experiments. Except for the vertical streak the qualitative scattering behaviour is similar to the *Nam315* sample. For more detail two reflections have been exemplarily depicted in figure 7.12. The initial observation seems to correspond with results from previous commercial photo polymers. This means an increasing Bragg diffraction angle for increasing wavelength. However, the angle selectivity $\Delta\lambda$ is broader than for commercial photo polymers. This is expectable since $\Delta\lambda$ depends on the thickness of the polymer which is less than $200\mu m$.
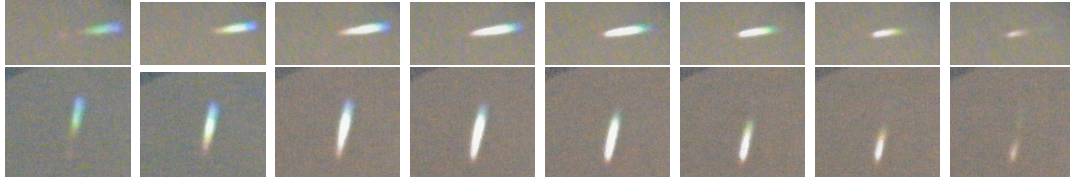
Fig. 7.12.: Laue diffraction pictures for different incident angles ω.

7.3.4. Polychromatic reflection scans for Nam313

In addition to the analysis of the wavelength-selective diffraction with the photo camera, the electronic photo diode system has been used to measure the Bragg peaks of certain reflections. Only reflections that have had a certain intensity have been chosen for measurement, otherwise the pulsed working principle of the laser would result in incorrect scattering efficiencies.

Since the samples did not show the classic Laue diffraction pattern, revelation of the symmetry and identification of the reflections is not trivial, but can be done by analysing the scattering angles. For the polychromatic scans a slit has been used in order to select a certain wavelength range $\Delta\lambda$ and block all other wavelengths. Firstly, two different spots have been considered which can be indexed by 2D Miller-indices as the $(11)T$ and $(-20)T$ reflections. Identification of these spots is done by determining the d-values which have to

(a) Reflection $(11)T$ (b) Reflection $(-20)T$
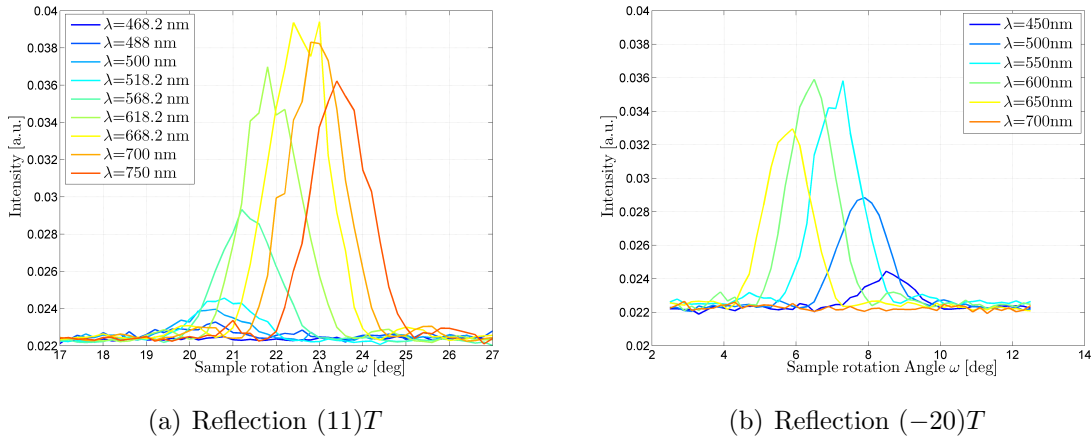
Fig. 7.13.: Laue Diffraction curves for different wavelengths λ.

be set for measuring the scattering curves. The d-value for the $(11)T$ reflection (cf. figure 7.13(a)) was found to be $d = 0.4\mu$m corresponding to the in-plane lattice parameter of nearly 5μm. The reflection depicted in figure 7.13(b) shows an opposite direction of colour-splitting. The d-value in this case indicates a $(-20)T$ reflection. However, the azimuthal angle between both reflections differ from the expected value by a value of $\Delta\phi = 30°$.

In order to get a deeper understanding of this issue further reflections have been investigated, as can be seen in figure 7.14 and figure 7.15. The inverse reflections have been measured, namely the $(20)T$ and the $(-1-1)T$ reflection. The identification of the diffracted beams based on the d-values revealed a similar angle offset $\Delta\phi$ as for the two previous reflections.

Those findings indicate a deviation in the structure from a trigonal one. An explanation for this deviation can be found by considering the holographic nature of the inscription process. According to this approach a trigonal structure should occur when the multiplexed beams do not couple with different orders. This means that a beam incident in one of the directions of the three beam combinations ab, cd and ef should only be able to reconstruct the respective beam pair. A coupling between e.g. a and d is possible but should be suppressed which does not seem to be the case for these PCs.
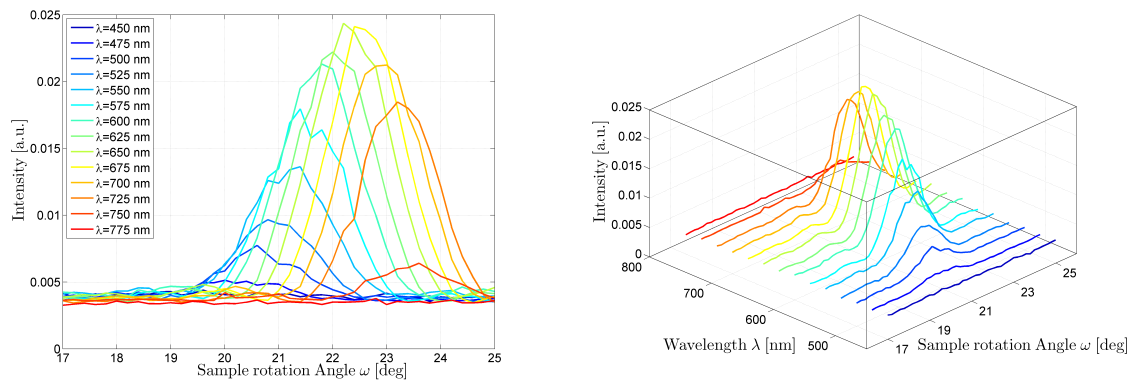
(a) Visible is the shift of the Bragg peak to higher angles.

(b) Better visualization of curves with lower intensity.

Fig. 7.14.: Laue diffraction curves for different wavelengths λ of the $(20)T$ reflection.

7.3.5. Monochromatic reflection scans for Nam313

Due to the fact that a slit has been used, the recorded intensity is rather low and also the diffraction efficiencies cannot be determined correctly. Moreover, the slit cannot select single wavelengths but only wavelength ranges $\Delta\lambda$ (which explains the Gaussian envelope to the polychromatic Bragg peaks). Therefore, monochromatic measurements have been done additionally.

The curves depicted in figure 7.16(a) show a diffraction efficiency that is of the order of one percent. This is far less than for the commercial photo polymers. This is also the reason for the limited number of peaks. Reflections which are even weaker cannot be identified and thus, the number of peaks available for the structure determination is also not sufficient.
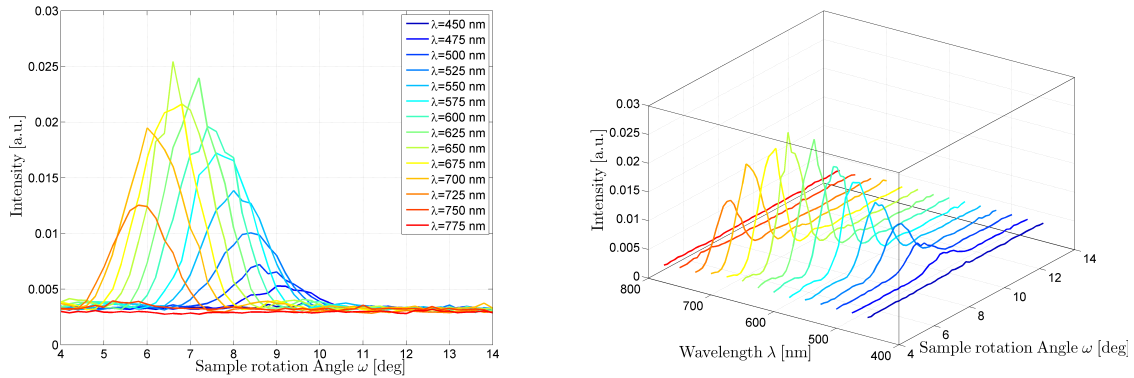
(a) 2D-plot: Visible is the shift of the Bragg peak to higher angles.

(b) Isometric view for a better visualization.

Fig. 7.15.: Laue diffraction curves for different wavelengths λ of the $(-1-1)T$ reflection.

Moreover, the transfer to reciprocal space yields further inconsistencies. The transferred
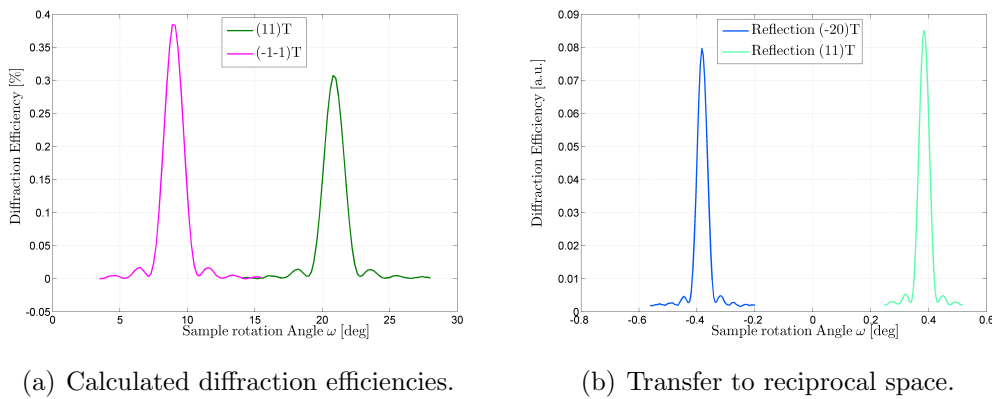
(a) Calculated diffraction efficiencies.

(b) Transfer to reciprocal space.

Fig. 7.16.: Scattering curves for selected reflections in angular as well as reciprocal space.

reflections do not have the proper l-coordinate. For the $(-20)T$-reflection an l-value of $l = -1$ is expected but the experimental one deviates by more than $\Delta l = 0.6$. The same holds true for the $(11)T$ reflection where the deviation is about $\Delta l = 0.4$.

A more detailed analysis of the scattering curves for this sample would not be meaningful since the low diffraction efficiency allows only the measurement of the Bragg peaks but not a sufficient quantity of the side fringes.

7.3.6. Conclusions

In comparison with results obtained from commercial photo polymers the NAMIROS photo polymers are not yet compatible in terms of stability, thickness and most importantly diffrac-

tion efficiency of the inscribed photonic lattices. One lack of the comparison is however the designated use of the photo polymers while the commercial ones are intended for holographic data storage, the NAMIROS photo polymers are supposed to allow an inscription of a lattice that can be used as a diffractive-optical element inside a 3D sensor system. Moreover, a photonic lattice is desired which has a sufficient amount of lattice parameters and exhibits a classic Laue diffraction pattern upon illumination by white light. Therefore, a non-linear response of the material is required to allow inscription of a non-sinusoidally modulated lattice.

The above mentioned features were not observed for the created samples mostly because the response of the material is still linear and therefore it can be concluded that the development of such kind of lattices still requires a more detailed study of the chemistry behind the polymer creation.

7.4. Discussion

In this part a comparison of the achieved results with alternative approaches will be done. This concerns only the *Aprilis* and *InPhase* polymers. The measurements of the diffraction curves for several reflections were conducted and later analysed by the kinematic approximation. As discussed earlier this approximation is in principle based on a geometric description of the scattering process and not on Maxwell's equations. Despite this, a fitted model based on kinematic approximation was used and yielded a good agreement with the measurements. The diffracted intensity was set as a fit parameter and so the diffraction efficiencies for each reflection could be determined.

In another work [15] the same type of samples was analysed with a different approach, namely the already (cf. chapter 2.2.2) mentioned rigorous coupled-wave analysis. This approach solves Maxwell's equations rigorously on a numerical basis. Experimental scattering curves of different reflections were compared with expectations from RCWA theory and a good agreement was found. The advantage of this rigorous theory is the ability to predict the diffraction efficiencies. The model also requires preciser knowledge about the polymer properties like for instance absorption, when this property is unknown it can be used inside the model as a free parameter. The disadvantage is the rather high computational effort that is necessary.

An approximative approach based on the RCWA theory is the two-wave coupled-wave approach. This approach is valid in the limit of small refractive contrast Δn. For a one-dimensional lattice (diffraction grating) analytical expressions were already derived in the 1960s [14]. The diffraction efficiency for a 1D transmission grating (without absorption) can

be calculated by:

$$I = \nu^2 \frac{\sin^2\left(\sqrt{\nu^2 + \xi^2}\right)}{\nu^2 + \xi^2} \tag{7.12}$$

In this approach ν and ξ are functions of the incident as well as diffracted angle, the lattice periodicity and the wavelength as well as the thickness of the grating. The reason for writing (7.12) in such a way is the striking similarity with the used kinematic model like the one in (7.9). More sophisticated models also account for beam polarization and aborption [61].

The important outcome of this investigation is the possibility to describe scattering curves with a simple kinematic model in a sufficiently precise method.

8. Summary

Light scattering from periodic micrometer-sized media has been investigated under two aspects. The first one was the theoretical description of the scattering process and the second one was the experimental investigation of the scattering process. Moreover, two different photonic crystals were available, the holographic photonic lattices and the woodpile-structured photonic crystals. While for the holographic structure-type the investigation was limited to the measurement, analysis and explanation of the scattering curves, the woodpile-structured crystals were treated with optical refractive index liquids in order to scrutinize the scattering patterns in terms of a refractive index difference. In the following a summary of the conclusions is given which were derived in this thesis.

8.1. Holographic lattices

Inside different photo polymers three-dimensional photonic lattices with a trigonal crystal structure were inscribed based on a holographic approach. The scattering curves of different reflections were measured and depending on the polymer, diffraction efficiencies of up to 60% were recorded. The functional behaviour of the scattering curves were described by a simple kinematic model. A comparison with other approximative approaches such as the two-wave coupled-wave approximation yielded a good agreement of the functional behaviour.

Additionally, the dispersive properties were analysed by diffraction of polychromatic ('white') laser light. For the *InPhase* photo polymers the Bragg condition was valid for a very narrow wavelength range $\Delta\lambda$ while the *Aprilis* photo polymer allowed Bragg diffraction in a wider range $\Delta\lambda$.

8.2. Woodpile-structured photonic crystals

The light diffraction of WP PCs was investigated in terms of an adjustable refractive index. The adjustment was done with commercial RI liquids (Cargille). The stability and reproducibility of the infiltration procedure were discussed elaborately. The conclusions from the experimental and theoretical investigations are given as follows:

- The influence of the refractive index difference on the scattering curves strongly depends on the considered reflection, e.g. $(01)T$ and $(02)T$. From the experimental point of view a pronounced effect regarding the second-order reflections has been found. The first-order reflections showed this effect only partially which can be explained by the sensitivity of this reflections to experimental issues like misalignment. In contrast to the experiment, the numerical simulation of the $(01)T$ reflection yields a more robust result than the $(02)T$ reflection.

- Experimentally, the refractive-index-dependent scattering curves could be subdivided into different scattering regimes. Basing on the set of second-order reflections, the regimes are labelled

  1. quasi-kinematic regime with a $\Delta n = 0.01 - 0.15$,

  2. regime of transition with a $\Delta n = 0.16 - 0.22$ and

  3. dynamic regime with a $\Delta n = 0.5$.

- The scattering curves basing on the numerically modelled data are subdivided into the

  1. (quasi-)kinematic regime with a $\Delta n = 0.01 - 0.12$,

  2. a regime of transition with a $\Delta n = 0.13 - 0.21$ and

  3. a dynamic regime with a $\Delta n = 0.22 - 0.5$.

- A comparison of the classifications of modelled and measured data reveals an agreement which is quite well within the margin of error.

9. Outlook

In this chapter the technological perspective for an implementation in a diffractive-optical device for each type of PC is discussed. Moreover, suggestions for improvements in the experimental and theoretical work are presented.

9.1. Implementation of PCs in diffractive-optical devices

For the idea to use three-dimensional photonic crystals or photonic phase lattices as preselective elements inside an optical sensor system a precise knowlegde of the light scattering behaviour is required. In this thesis the required knowledge was gathered and presented for both types of lattices.

The holographic lattices have the big advantage of a high reproducibility in the production process, a large-sized and defect-free sample area which is useful for the implementation inside technical devices. Furthermore, they have a large diffraction efficiency and a very sharp angle selectivity. Unfortunately, one of the drawbacks is that mostly only one diffraction order is available which is caused by the RI nature of this type of lattice structure. One way to overcome this drawback is the development of a polymer which has an explicit non-linear response to the inscription process. Such kind of research is currently carried out where one idea to induce a non-linearity is based on the insertion of small nano-particles inside a photo polymer.

The advantage of the WP PCs is the tunability of the RI with the help of RI liquids. Furthermore, the diffraction pattern resembles a classic Laue diffraction pattern. The drawbacks for this type of PCs are clearly the limited macroscopic in-plane size $(100 - 150\mu\text{m})$ as well as the small number of stacked layers. The first point makes this type of PC difficult to implement in diffractive-optical instrumentations whereas the second point causes a broadening of the Bragg condition for diffraction. Another drawback is the missing reproducibility in sample fabrication (quality) which has been extensively documented in this thesis.

The bottom line is that the favourable preference of PCs for technical applications concerning diffractive-optical purposes is given by the holographic phase lattices.

9.2. Further improvements of the experimental and theoretical analysis

Concerning the experimental investigation of the scattering behaviour, an improvement could be made by replacing the used diffractometer which is rather bulky. Moreover, the used photo diode is a zero-dimensional point detector which has the advantage of a high dynamic range regarding the determination of scattering efficiencies but a two-dimensional detector could improve the experiment in such a way that the simultaneous recording of multiple reflections enhances the understanding of the interplay between these reflections. The latter point is especially interesting when considering the polychromatic diffraction.

The enhancement from a theoretical point of view concerns mainly the WP PCs. Here, the development of a non-commercial software would be useful for the explicit understanding of the interaction of the different orders of Fourier components for different reflections. This could prove especially useful when considering an increased RI contrast.

A. Derivation of the Scattering Geometry

In chapter 3 the scattering geometry was shortly introduced. In this part a thorough derivation of the scattering geometry, which is necessary for an understanding of the used scanning methods, will be given. The so-called analytical approach is mainly based on the nomenclature given in [41]. This derivation is based on the consideration of the interplay of different wave vectors. Another comprehensible approach is the geometrical approach which makes use of the Ewald sphere construction (cf. figure 3.3), a description of this can be found in [11].

A.1. Analytical approach

The light transmission through a thin PC is considered. The z-direction (out-of-plane ($\perp$)) corresponds to the direction where the PC has its smallest extension, i.e. the stacking direction. The incident beam is first refracted at the PC, then the interaction with the lattice takes place. Afterwards the exiting beams are once more refracted. In this part the beams are considered to be within the PC, unless stated otherwise.

The wave vector $\mathbf{k}$ of the scattered beam can be decomposed into a parallel ($\mathbf{k}_{\parallel}$) and a perpendicular ($\mathbf{k}_{\perp}$) part whereas the incoming beam is referred to as $\mathbf{k}_0$.

$$\mathbf{k} = \mathbf{k}_{\parallel} + \mathbf{k}_{\perp} = k_{\parallel} \cdot \mathbf{e}_{\parallel} + k_{\perp} \cdot \mathbf{e}_{\perp} \tag{A.1}$$

In (A.1) the coordinate system ($\mathbf{e}_{\parallel}, \mathbf{e}_{\perp}$) was introduced. Due to Bloch's theorem the in-plane ($\mathbf{k}_{\parallel}$) component equals the one of the incident beam plus an in-plane reciprocal lattice vector ($\mathbf{k}_{\parallel} = \mathbf{k}_{\parallel,0} + \mathbf{G}_{\parallel}$). However, Bloch's theorem is not valid for the z-direction. The out-of-plane component can be calculated by further considering (A.1).

$$k_{\perp}^2 = k^2 - (k_{\parallel,0} + G_{\parallel})^2 \Rightarrow k_{\perp} = \sqrt{\frac{\omega^2 n_{\text{eff}}^2}{c^2} - (k_{\parallel,0} + G_{\parallel})^2} \tag{A.2}$$

In (A.2) the relation $|k| = \frac{\omega n_{\text{eff}}}{c}$ was employed.

A.1.1. Relation between incident and diffracted angle

The diffracted and incident angles are connected with the wave vector via

$$k \sin(\theta - \omega_{\text{inc}}) = k_{\parallel} \tag{A.3}$$

$$\Rightarrow \sin(\theta - \omega_{\text{inc}}) = \frac{k_{\parallel}}{k} = \frac{k_{\parallel,0} + G_{\parallel}}{k} \tag{A.4}$$

In equation (A.4) the following terms can be simplified, $\frac{k_{\parallel,0}}{k} = \sin \omega_{\text{inc}}$ and $\frac{G_{\parallel}}{k} = \frac{\lambda}{d(G_{\parallel})}$. This yields the final relation

$$\theta = \arcsin\left(\sin \omega_{\text{inc}} + \frac{\lambda}{d(G_{\parallel})}\right) + \omega_{\text{inc}}. \tag{A.5}$$

A.1.2. Transfer to reciprocal space

The transfer wave vector $\mathbf{q}$ is of special interest when considering diffraction. For a specific reflection it is defined as the difference between diffracted and incident beam.

$$\mathbf{q} = \mathbf{k} - \mathbf{k}_0 \tag{A.6}$$

Furthermore, the $\mathbf{q}$-vector can be split into a parallel and perpendicular component, $\mathbf{q} = \mathbf{q}_{\parallel} + \mathbf{q}_{\perp}$. The parallel transfer wave vector is given by a reciprocal lattice vector and the perpendicular component can be received by considering (A.2).

$$\mathbf{q}_{\parallel} = \mathbf{k}_{\parallel} - \mathbf{k}_{\parallel,0} = \mathbf{G}_{\parallel} \tag{A.7}$$

$$q_{\perp} = (\mathbf{k} - \mathbf{k}_0) \cdot \mathbf{e}_{\perp} = k_{\perp} - \mathbf{k}_0 \cdot \mathbf{e}_{\perp} \tag{A.8}$$

With $\mathbf{k}_0 \cdot \mathbf{e}_{\perp} = 2\pi \cos(\omega_{\text{inc}}) n / \lambda$ and replacing the frequency ω in (A.2) by $2\pi c / \lambda$, the perpendicular component can be rewritten as

$$\mathbf{q}_{\perp} = \frac{2\pi n_{\text{eff}}}{\lambda} \left(\sqrt{1 - \left(-\frac{\sin(\omega)}{n_{\text{eff}}} + \frac{\lambda}{d(\mathbf{G}_{\parallel}) n_{\text{eff}}}\right)^2} - \cos\left(\arcsin\left(\frac{-\sin(\omega)}{n_{\text{eff}}}\right)\right) \right) \cdot \mathbf{e}_{\perp} \tag{A.9}$$

where the out-of-plane direction ($\mathbf{e}_{\perp}$) corresponds to the $\mathbf{c}^*$-direction for the considered lattices in this thesis. Moreover, the symbol ω in (A.9) does not represent the frequency anymore, but stands for the so-called sample rotation angle ω which is related to the angle of the incident beam ω_{inc} **inside** the PC via $\omega_{\text{inc}} = \arcsin\left(\sin(-\omega)/n_{\text{eff}}\right)$.

B. Woodpile Photonic Crystals - SU8 Photo Resist

All of the WP PCs made from SU8 were cylindrical with a diameter of around 150 μm (cf. figure 1.8) and a height of six layers. They were also confined by a massive wall in order to prevent any possible broadening of the structure due to some instabilities. The in-plane lattice constant was given by $a = 1\mu m$ and the out-of-plane lattice constant can be calculated by $c = a\sqrt{2}$.

B.1. First set of photonic crystals

The first investigations in this work with WP PCs were done in such a way that scattering curves were recorded in the uninfiltrated state. Afterwards the sample was removed from the diffractometer and infiltrated with a refractive index liquid. Then scattering curves were recorded for the infiltrated sample. This procedure was accompanied by an investigation with optical microscopy.

B.1.1. Description of the infiltration technique

By the simple technique of dropping the refractive index liquid onto the sample it is assumed that with time the liquid will fill the voids in between the logs. Since the scattering curves are recorded with the sample's surface mounted 90° tilted to the Earth's surface (vertical) it was expected that the liquid would flow out of the PC. Therefore, the very first idea was to cover the filled crystal with a glass plate. However, this results in more severe problems such as a damaging of the crystal while putting the glass cover on top of it. Another additional inconvenience is that once the cover is fixed it is not removable and so the RI difference is also fixed. That is why the idea of covering the remaining samples of this set was abandoned. The liquid was just dropped onto the glass plate in horizontal position and after a while mounted onto the diffractometer where the measurements were made with the sample in vertical position.

B.1.2. Experimental investigation

Firstly, Laue diffraction patterns in transmission geometry have been recorded by using the $\lambda = 488$nm emission line of the Ar-Kr-laser. Figure B.1(a) shows an isometric view of
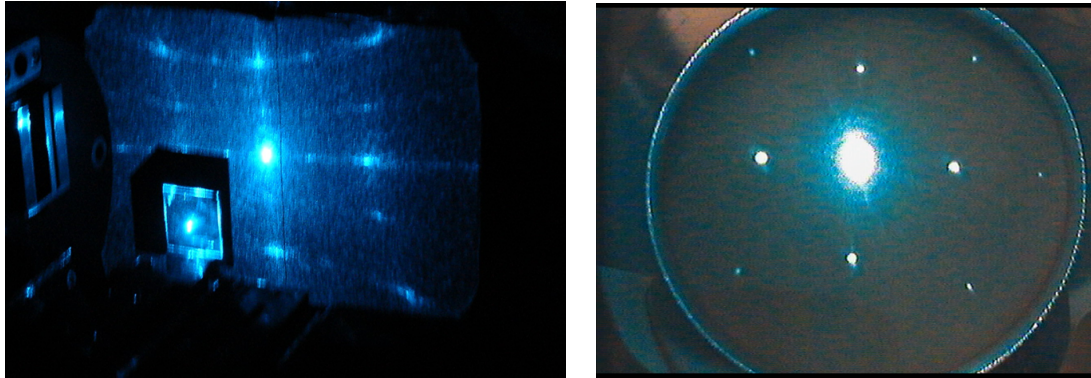
(a) Laue diffraction pattern prior to infiltration.

(b) Laue diffraction pattern after infiltration.
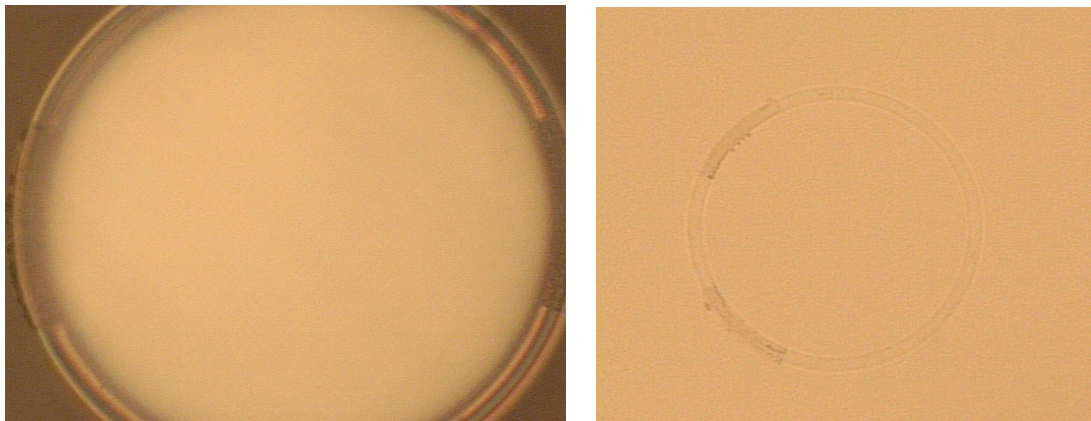
(c) Magnified picture with a microscope (50x) prior to infiltration.

(d) Magnified picture with a microscope (20x) after infiltration.

Fig. B.1.: Laue diffraction patterns of a WP PC caused by illumination with blue laser light as well as photographs of a WP PC magnified via an optical microscope.

the experiment. In the front one can see the illumination spot at the crystal and laterally displaced behind the crystal the Laue diffraction pattern before infiltration with an RI liquid. In figure B.1(b) one can see the Laue diffraction pattern in transmission geometry for the same PC which has been infiltrated with an optical RI liquid with a value of $n_D = 1.58$. A change in the diffraction pattern is visible. After the infiltration one observes that the Laue diffraction spots located symmetrically around the primary non-diffracted beam become more pronounced. These more pronounced spots represent diffracted beams that obey the Laue equations. Prior to infiltration those spots are also visible, but firstly they are smeared out and secondly there are additional elements of diffraction that cannot be explained by the Laue equations.

In figure B.1(c) an image of an unfilled WP PC magnified 50 times by a microscope is depicted and in figure B.1(d) an image of the same PC is visible directly after infiltration with an optical liquid. While in figure B.1(c) the structure is clearly visible, it cannot be seen in figure B.1(d) due to the fact that the refractive contrast is too small, the only part remaining visible is the boundary ring.

Measurements of the scattering curves were done before and after infiltrating the PC with an optical RI liquid of refractive index $n_D = 1.58$ which yield a contrast of $\Delta n \cong 0.03$. The scattering curves of the $(01)T$ and $(02)T$ diffraction curves have been plotted in figure B.2 and compared with curves based on the very simple kinematic model of diffraction. The intensities in figure B.2 have been normalised for better comparison.

(a) (01)T Reflection
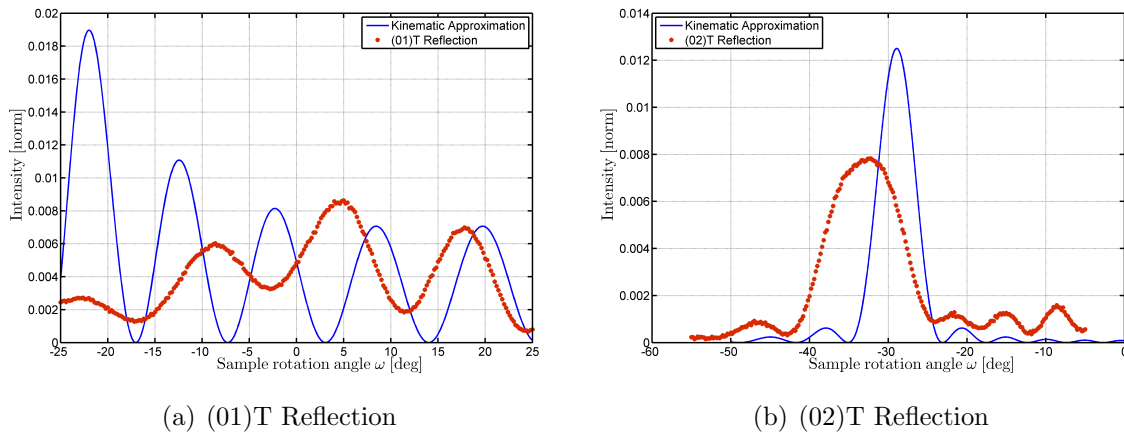
(b) (02)T Reflection

Fig. B.2.: Scattering curves of a WP PC for $\lambda = 488$nm and for comparison curves expected from kinematic theory.

For the $(02)T$ reflection one can see a distinct Bragg peak, compared to the kinematic curve the main peak is broadened and the intensity ratio of side peaks and main peak is higher. Due to the structure factor the $(01)T$ reflection has no Bragg peak but exhibits the intensity oscillations as seen in figure B.2. Because of the absence of a Bragg peak the $(01)T$ reflection is a so-called weak reflection. For comparison with theory the measurements of the $(02)T$ reflections are not so strongly influenced by experimental side effects.

As earlier mentioned the sample was not sealed and vertically aligned, so that the liquid is able to flow out of the sample by means of gravity. After leaving the sample in this position for a longer period ($>$ several days) an effect that has been observed is the development of ring-like diffraction patterns that surround the primary beam. Furthermore, additional peaks of weaker intensity become visible. The corresponding picture was recorded and is depicted in figure B.3 Further investigations made with an optical microscope show a ring-like structure that surrounds the circular boundary wall. Additionally, the liquid is not
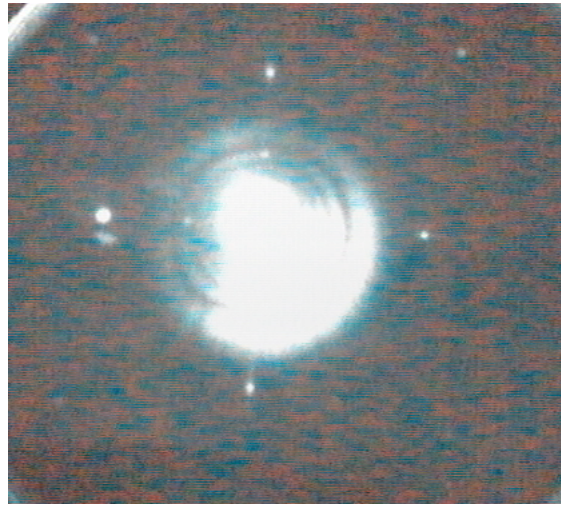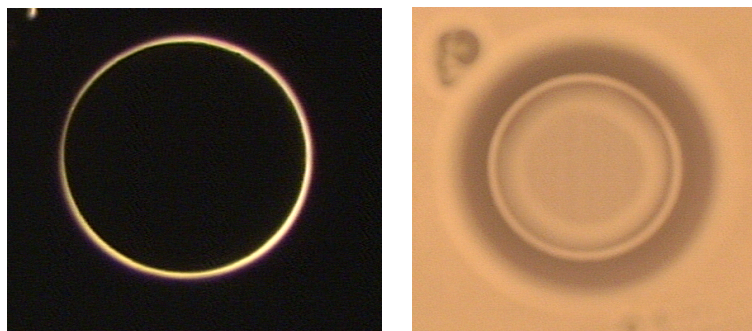
Fig. B.3.: Change of the diffraction pattern after one week.

distributed homogeneously inside the sample anymore which can be seen by the increasing circular contrast in figure B.4.

(a) Dark field microscopy image of the sample.

(b) Bright field microscopy image of the sample.

Fig. B.4.: Microscope images that show changes in the infiltration of the sample. Especially in the bright field image a change in the contrast is visible.

The effect of the change in the distribution on the scattering curves was also investigated. Therefore, measurements of the scattering curves of the $(0-1)T$ and $(0-2)T$ have been conducted (cf. figure B.5). The analysis of the scattering curves show that the scattering intensity reduces after a longer storage of the sample in vertical position. This is the case for both investigated reflections.

The possibility of refilling the sample with RI liquid was further investigated. The refill was done in such a way that the sample was exposed to several drops of RI liquid in horizontal position. After a short time the sample was again mounted and further investigated by recording the scattering curves and by optical microscopy.

(a) (0-1)T Reflection
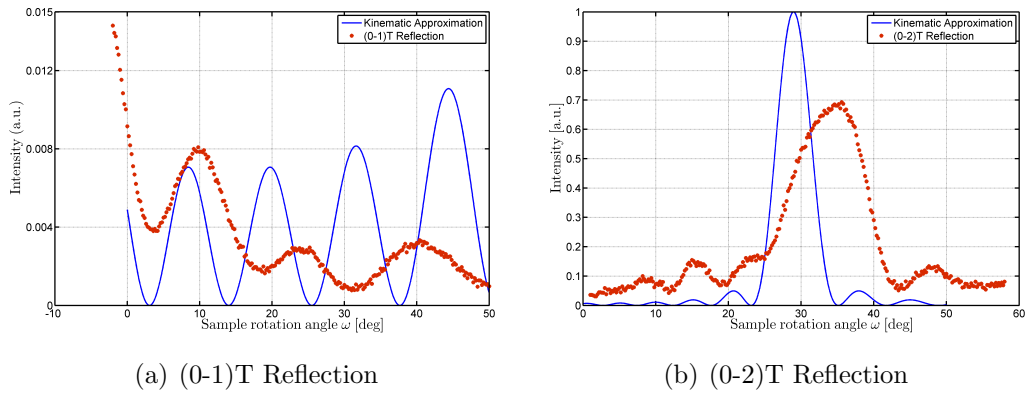
(b) (0-2)T Reflection

Fig. B.5.: Scattering curves of $(0-1)T$ and $(0-2)T$ reflections to analyse the long-term effect of the infiltration. Red curves are measurement and blue curves are kinematic curves for comparison.

(a) (01)T Reflection (1st refill)

(b) (02)T Reflection (1st refill)

(c) (01)T Reflection (2nd refill)

(d) (02)T Reflection (2nd refill)
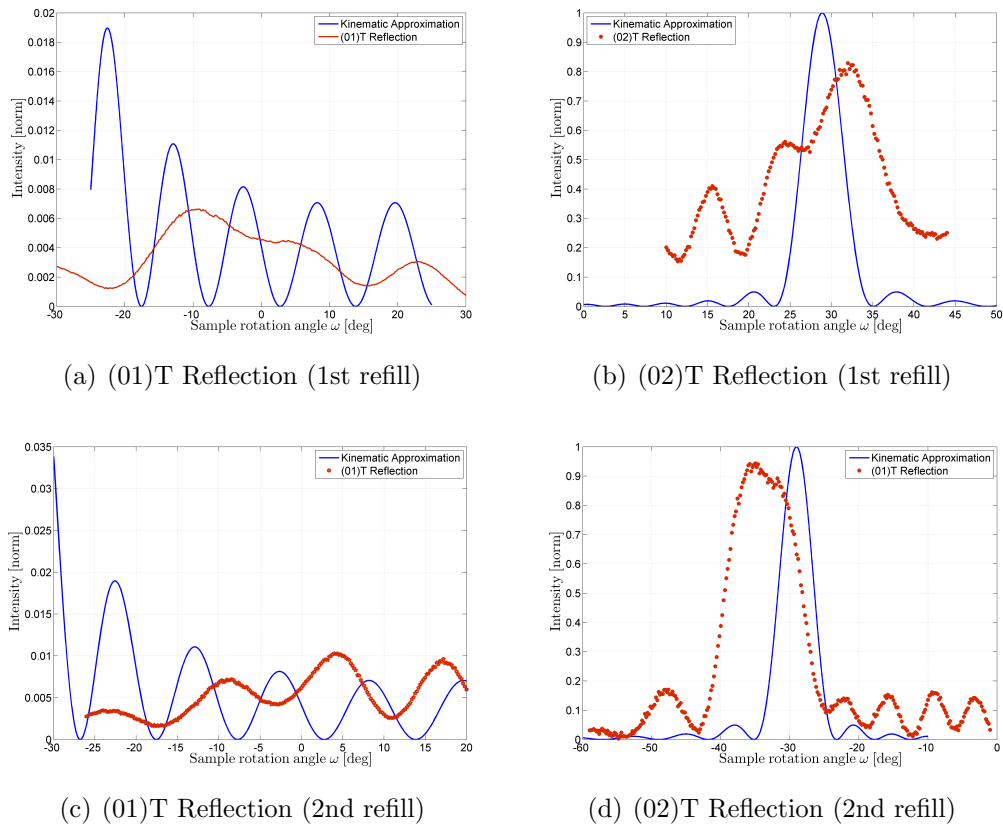
Fig. B.6.: Measurement of the scattering curves after the first and second refill.

The scattering curves are shown in figure B.6. The curves of the $(0-1)T$ and $(0-2)T$ reflections correspond to the ones of the $(01)T$ and $(02)T$ reflections which were shown as the first measurements after infiltration. The refill process was done two times due to the fact that the first curves did not have the expected form and also the images from microscopy revealed a larger contrast than before. That is why for the second refill the sample was kept in a horizontal position for a longer time to allow for a better distribution of the RI liquid inside the PC. The result of this is that the scattering curves correspond better to previous measurements.

B.1.3. Conclusions

This first investigation was done to find out the influence of RI liquids infiltrated into WP PCs. The RI contrast was chosen to be small in order to be able to compare the scattering curves with kinematic theory. However, the investigation and also the analysis was done rather qualitatively which means that no statement can be made on the following points: Images from optical microscopy can can only be used for an investigation of the RI liquid distribution on the surface. Therefore, statements about the degree of filling of the PC cannot be made. That is also why the effect of peak broadening is not necessarily due to the RI contrast.

The important conclusions that **_can_** be drawn from this investigation are given in the following:

1. An RI liquid infiltration of the sample with subsequent sealing with a glass plate can cause a damage of the sample and is therefore not recommendable.

2. Sample infiltration with RI liquids show considerable change in the diffraction pattern towards a structure that comes closer to a classic Laue image and therefore it can be concluded that the process of infiltration can be in principle a useful method for investigating diffraction for different RI contrast. This point is also supported by the fact that the diffraction curves show a clearly visible Bragg peak.

3. After some time portions of the RI liquid will flow out of the sample, but the experiments have shown that a proper refill can be made and it will produce comparable scattering curves.

B.2. Second set of photonic crystals

The second set of samples was originally intended to tune the RI contrast of the PCs with liquids of different RI values. Inital investigations of the PC after RI liquid infiltration under

ambient conditions indicated an incomplete infiltration of the PC. Therefore, a different technique for infiltration has been used which will be described in the following paragraph. Subsequently, the experimental investigations by diffraction experiments are presented.

B.2.1. Infiltration technique

The filling was accomplished by using a desiccator (figure B.7). The air was sucked out and a vacuum of around 10^{-2} was established inside a sealed glass dome. Before establishing the vacuum a small spot of the refractive index liquid was dropped onto the glass substrate next to where the sample was located. After the vacuum was established the desiccator was tilted in order to allow the liquid to flow inside the sample. Then the sample was kept in vacuum for some time. The used RI liquid had the an RI value of $n = 1.58$. After examining the sample the impression of an incompletely infiltrated sample remained. This impression is based on a comparison with the behaviour of the first set of SU8 WP PCs. The expectation is that the almost matched contrast would cause a vanishing of the visibility of the structure like in figure B.1(d). Since this vanishing was not observed to this degree two preliminary conclusions can be drawn. The first one is that the infiltration of the samples in this set is independent whether being employed under vacuum (at least for the one we used) or ambient conditions. The second one is that the infiltration is incomplete either way. Nevertheless, a thorough investigation of the scattering properties has been done.

Fig. B.7.: Desiccator for infiltration under vacuum.

B.2.2. Experimental investigation

The measurements of the scattering curves were carried out in our experimental setup (cf. figure 4.1). Although for larger 3D crystals all symmetric reflections, e.g. {01} arising from (01), (0 − 1), (10) and (−10) lattice planes, are supposed to have the same scattering curves, it is possible that for the considered thin PCs surface effects might play a role. When refering to surface effects especially one point needs to be addressed and this is the orientation of the first layer towards the beam. The same holds true for the {02} reflections resulting from (02), (0 − 2), (20) and (−20) planes.

Two PCs of this sample set have been investigated. In the following they are referred to as sample A and B. Before recording the curves the sample quality was moreover judged by band structure measurements which revealed that sample B was of higher quality. That is why the investigation was focussed more on this sample.

Before the scattering curves are analysed, a comparison of the diffraction pattern is shortly mentioned. The difference between infiltrated and uninfiltrated state was clearly visible, however the pattern still had a much more dynamic structure than the first set (cf. figure B.1(a)). A considerable difference between the infiltration under vacuum and under ambient conditions was not visible.
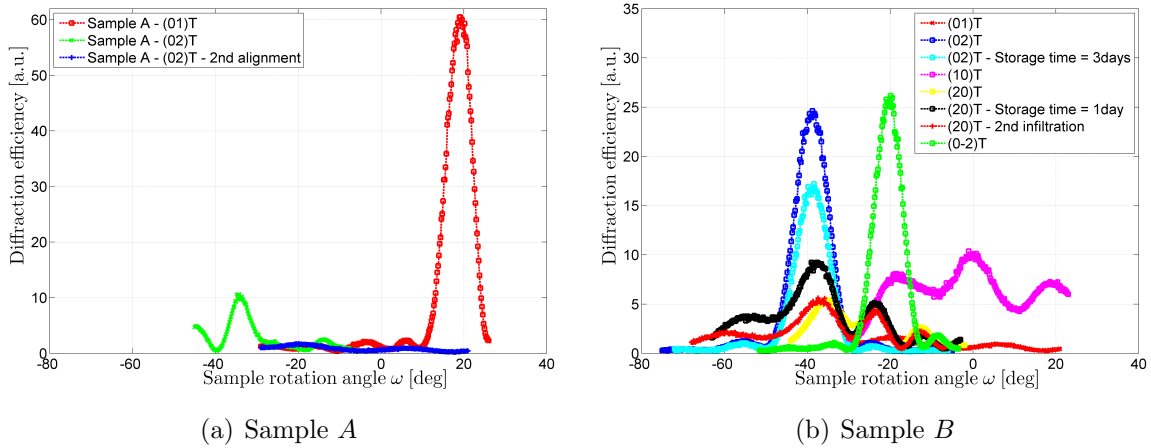
(a) Sample A

(b) Sample B

Fig. B.8.: Compilation of scattering curves of different reflections of the second set of SU8 WP PCs.

A compilation of all scattering curves for both samples can be found in figure B.8. While a specific comparison for the $(20)T$ and $(02)T$ reflections is shown in figure B.9. The scattering curves of sample A indicate a strong deviation compared to kinematic approximation which should be valid at this Δn. Therefore, this sample was not considered for further investigations. The focus is now mainly directed to the $(20)T$ and $(02)T$ reflections. From the measurements one can see that those reflections have different scattering curves (cf.

figure B.9(a) and figure B.9(b)). In figure B.9(a) scattering curves of the $(20)T$ reflection are shown. They deviate strongly from the kinematic approximation which would predict a single Bragg peak with side fringes. Moreover, it was investigated how the structure behaves after re-infiltration and it was found that similar scattering curves can be recorded. Similar scattering curves can also be obtained after the sample is stored for more than a day in vertical position. In contrast to the $(20)T$ reflection, the scattering curves of the $(02)T$ reflection exhibit a structure which is well comparable to kinematic approximation except for one point which is the obvious deviation of the Bragg angle. The angular difference of the experimental Bragg angle of the $(02)T$ reflection is approximately $-10°$ while it is $+10°$ of the $(0-2)T$ reflection. A possible explanation to this is an inclination angle between the normals of the crystal surface and the glass substrate.

The second point is a comparison of scattering curves of an infiltrated PC where the infiltration took place under vacuum and under ambient conditions. In figure B.9(c) scattering curves of the $(20)T$ reflection have been compiled where the PC was infiltrated under ambient conditions multiple times. The scattering curves indicate reproducible results which deviate similarly from kinematic approximation as the curves in figure B.9(a). An interesting observation is the difference in the scattering efficiencies for different iterations of the infiltration. This is due to the fact that each time after infiltration the PC has to be realigned and because of the small dimensions of the PC small misalignments can cause such kind of deviations. Furthermore, a comparison of scattering curves of PCs infiltrated under vacuum and under ambient conditions is given in figure B.9(d). The structure of the curves do not deviate much, except for the offset of circa $20°$ which was also seen earlier for the $(02)T$ and $(0-2)T$ reflections.

Since these PCs showed an unexpected scattering behaviour another type of analysis was employed which is the recording of SEM images (cf. figure B.10). From those pictures it is clearly visible that the quality of the PC is rather low, because the rods are not aligned parallel anymore but they are rather vermiculated. It is unclear if this is due to the interaction with RI liquids.

## B.2.3. Analysis of the scattering curves

The obtained scattering curves were discussed qualitatively in the previous section. In this section the scattering curves are analysed by employing a simple kinematic model. Obviously, the $(0\pm2)T$ reflections are the only two reflections that can be approximated by a kinematic approach. A model based on (B.1) has been fitted to the $(02)T$ and $(0-2)T$ reflections after conversion from angular space to reciprocal space. Furthermore, the intensity was normalized. It was assumed that the PC consisted of $N_c = 6$ layers in c-direction.
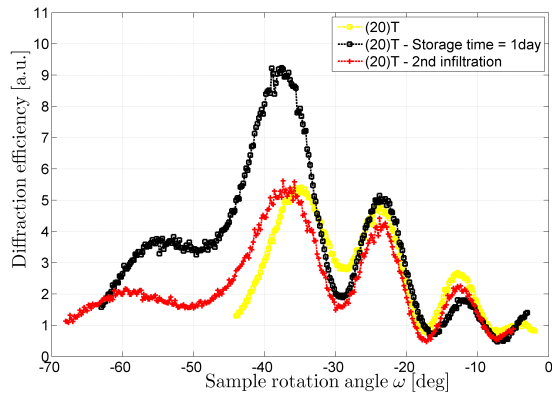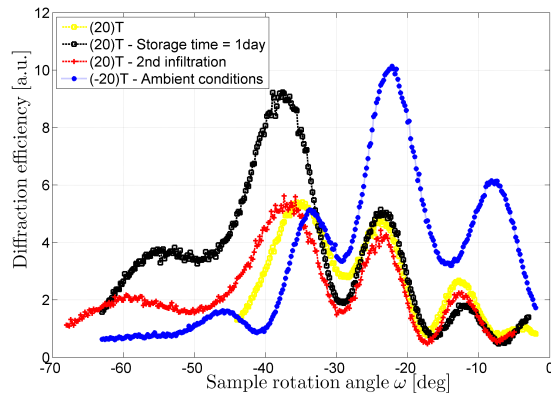
(a) $(20)T$ Reflection. PC infiltrated under vacuum.
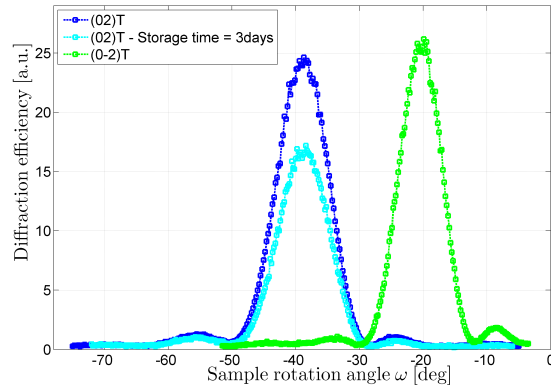
(b) $(02)T$ Reflection. PC infiltrated under vacuum.
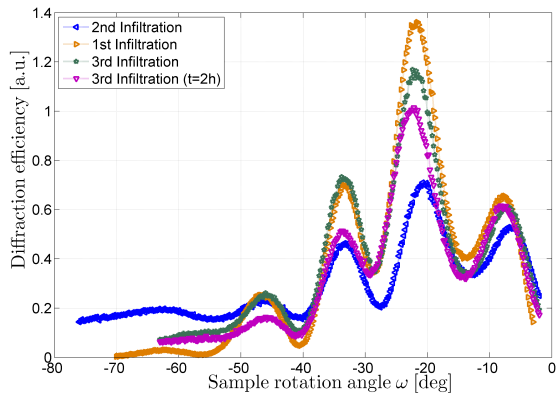
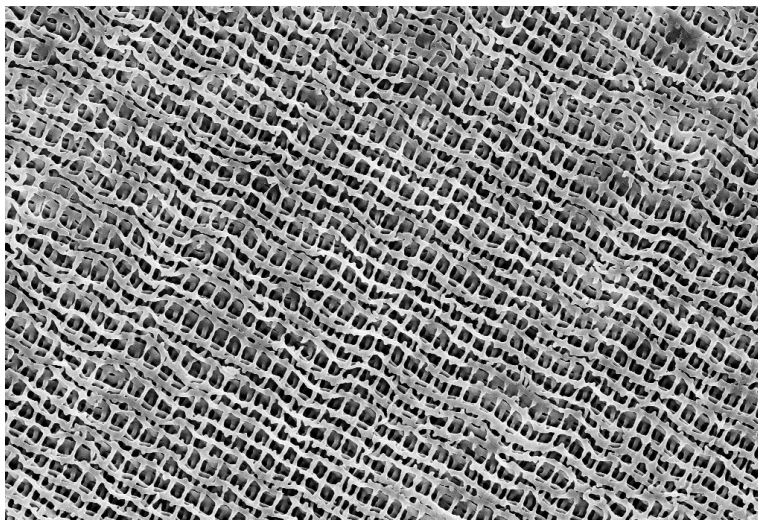(c) $(-20)T$ Reflection. PC infiltrated under ambient conditions.

(d) $(20)T$ and $(-20)T$ Reflection. Comparison between infiltration under vacuum and under ambient conditions.
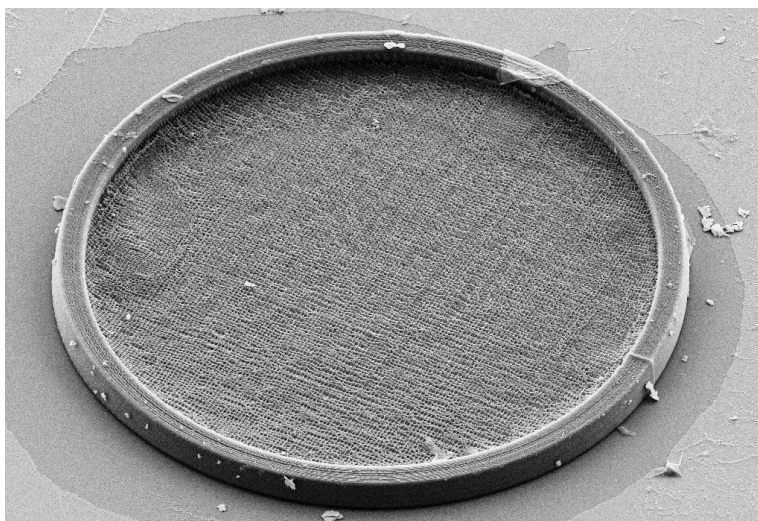
Fig. B.9.: Selected scattering curves of the $(02)T$ and $(20)T$ reflections of sample B. It is indicated whether the infiltration took place under vaccum or under ambient conditions.
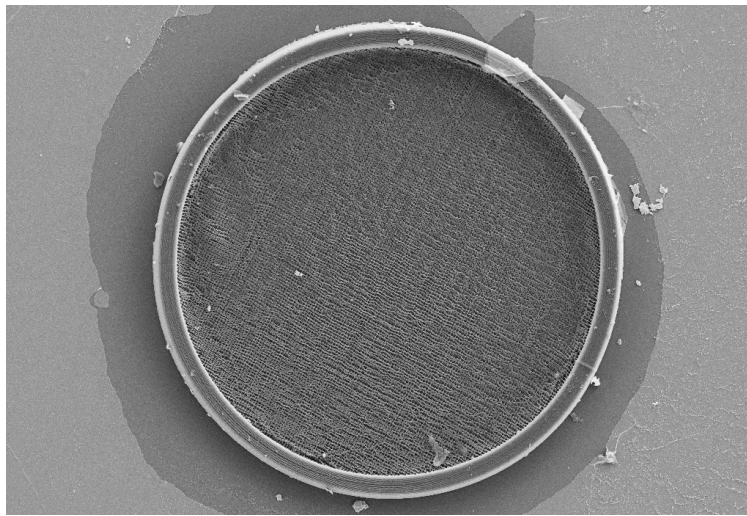
(a) Magnification factor 450.

(b) Magnification factor 2500.

(c) Magnification factor 600. 45° tilt of stage.

Fig. B.10.: PC images after deletion of the RI liquid made with a scanning electron microscope (SEM).

$$I^{(0\pm2)T}(l) = I_0 \cdot \left(\frac{\sin(6 \cdot B \cdot \pi \cdot (l - l_0))}{6 \cdot \sin(B \cdot \pi \cdot (l - l_0))}\right)^2 \cdot \cos\left(\pm\pi + \pi/2 \cdot B \cdot (l - l_0)\right)^2 \qquad (B.1)$$

The fitted curves along with the experimental data can be seen in figure B.11. A symmetric deviation from $l = 0$ is visible and is quantified along with the fitted parameters in table B.1. The parameter B indicates that a smaller amount of layers contributed to the scattering. By taking a look at the SEM images (cf. figure B.10) it can be concluded that the surface layer of the PC with the wiggly rods does not give a contribution to the scattering signal but rather adds to diffuse scattering. The layers beneath the top layer seem to have a sufficient symmetry to cause Bragg diffraction. However, this does not explain the asymmetry in the reflections.
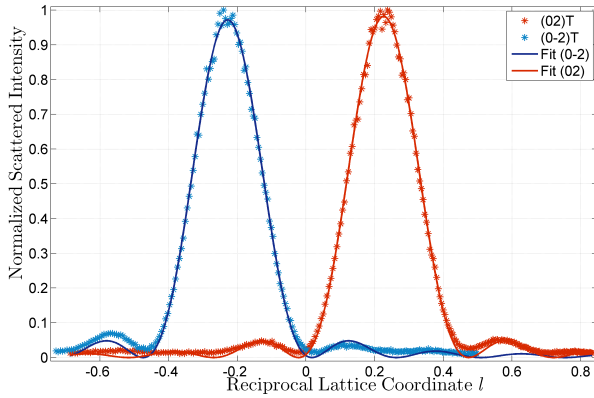
Fig. B.11.: Kinematic fit of the scattering curves of the $(0 \pm 2)T$ reflections

Tab. B.1.: Obtained fit parameters

	$(0-2)T$	$(02)T$
B	0.678 ± 0.005	0.673 ± 0.004
I_0	0.972 ± 0.007	0.981 ± 0.006
l_0	-0.228 ± 0.001	0.226 ± 0.001

Bibliography

[1] P. P. Ewald. Crystal Optics for Visible Light and X Rays. *Review of Modern Physics*, 37(1):46–56, Jan 1965.

[2] C. López. Materials aspects of photonic crystals. *Advanced Materials*, 15(20):1679–1704, 2003.

[3] Eli Yablonovitch. Inhibited spontaneous emission in solid-state physics and electronics. *Phys. Rev. Lett.*, 58(20):2059–2062, May 1987.

[4] Sajeev John. Strong localization of photons in certain disordered dielectric superlattices. *Phys. Rev. Lett.*, 58(23):2486–2489, Jun 1987.

[5] C. Dux and H. Versmold. Light Diffraction from Shear Ordered Colloidal Dispersions. *Physical Review Letters*, 78:1811–1814, 1997.

[6] H. M. van Driel and W. L. Vos. Multiple Bragg wave coupling in photonic band-gap crystals. *Phy. Rev. B*, 62:9872–9875, October 2000.

[7] S. Romanov. Structure of light scattering spectra in opal photonic crystals. *JETP Letters*, 79:614–619, 2004. 10.1134/1.1790018.

[8] G. M. Gajiev, V. G. Golubev, D. A. Kurdyukov, A. V. Medvedev, A. B. Pevtsov, A. V. Sel'Kin, and V. V. Travnikov. Bragg reflection spectroscopy of opal-like photonic crystals. *Phys. Rev. B*, 72(20):205115–+, November 2005.

[9] Willem L. Vos, Rudolf Sprik, AD Lagendijk, Gerard H. Wegdam, Alfons Van Blaaderen, and Arnout Imhof. *Photonic Band Gap Materials*, chapter Influence of optical Band Structures on Diffraction of Photonic Colloidal Crystals, pages 107–118. 1 edition, 1996.

[10] Alexandra Ledermann, Ludovico Cademartiri, Martin Hermatschweiler, Costanza Toninelli, Geoffrey A. Ozin, Diederik S. Wiersma, Martin Wegener, and Georg von Freymann. Three-dimensional silicon inverse photonic quasicrystals for infrared wavelengths. *Nat Mater*, 5(12):942–945, December 2006.

[11] Marcel Roth. *Kinematische und dynamische Lichtstreuung an dünnen photonischen Kristallen.* Master's thesis, Universität Siegen, 2007.

[12] Jesper Serbin and Min Gu. Superprism phenomena in polymeric woodpile structures. *Journal of Applied Physics*, 98(12):123101, 2005.

[13] Peng Zhang, Robert Egger, and Zhigang Chen. Optical induction of three-dimensional photonic lattices and enhancement of discrete diffraction. *Opt. Express*, 17(15):13151–13156, Jul 2009.

[14] Herwig Kogelnik. Coupled wave theory for thick hologram gratings. *The Bell System Technical Journal, Vol.˜48, no.˜9, November 1969, pp.˜2909-2947*, 48:2909–2947, November 1969.

[15] Christian Müller. *Herstellung und Analyse Photonischer Raumgitter für diffraktiv-optische Abbildungen.* Sierke Verlag, 2010.

[16] Christian Mueller, Henning Markoetter, Alexander Schloesser, and Susanna Orlic. 3d photonic gratings for optical sensing and image processing. volume 7053, page 70530A. SPIE, 2008.

[17] W. Kleber. *Einführung in die Kristallographie.* Verlag Technik, 1956.

[18] John D. Joannopoulos, Robert D. Meade, and Joshua N. Winn. *Photonic Crystals: Molding the Flow of Light.* Princeton University Press, 1995.

[19] Bahaa E. A. Saleh and Malvin Carl Teich. *Fundamentals of Photonics.* Wiley John and sons, 2007.

[20] Joseph W. Goodman. *Introduction to Fourier Optics.* Roberts & Company Publishers, 2005.

[21] G. Hesse, R. Kowarschik, and A. Richter. Volume holograms as frequency-selective elements. *Optical and Quantum Electronics*, 11:87–96, 1979. 10.1007/BF00624060.

[22] L. Z. Cai, X. L. Yang, and Y. R. Wang. All fourteen bravais lattices can be formed by interference of four noncoplanar beams. *Opt. Lett.*, 27(11):900–902, Jun 2002.

[23] L. Z. Cai, X. L. Yang, and Y. R. Wang. Formation of three-dimensional periodic microstructures by interference of four noncoplanar beams. *J. Opt. Soc. Am. A*, 19(11):2238–2244, Nov 2002.

[24] Xiulun Yang, Luzhong Cai, and Qing Liu. Polarization optimization in the interference of four umbrellalike symmetric beams for making three-dimensional periodic microstructures. *Appl. Opt.*, 41(32):6894–6900, Nov 2002.

[25] G. Grynberg and C. Robilliard. Cold atoms in dissipative optical lattices. *Physics Reports*, 355(5-6):335 – 451, 2001.

[26] K. I. Petsas, A. B. Coates, and G. Grynberg. Crystallography of optical lattices. *Phys. Rev. A*, 50(6):5173–5189, Dec 1994.

[27] Semen Gorfman. personal communication, 2007.

[28] http://en.wikipedia.org/wiki/Trigonal_crystal_system.

[29] Alvaro Blanco, Kurt Busch, Markus Deubel, Christian Enkrich, Georg von Freymann, Martin Hermatschweiler, Wolf-Peter Koch, Stefan Linden, Daniel C. Meisel, and Martin Wegener. *Photonic Crystals: Advances in Design, Fabrication and Characterization.* Wiley-VCH Verlag GmbH & Co KGaA, 2004.

[30] Satoru Shoji, Hong-Bo Sun, and Satoshi Kawata. Photofabrication of wood-pile three-dimensional photonic crystals using four-beam laser interference. *Applied Physics Letters*, 83(4):608–610, 2003.

[31] K. Busch, G. von Freymann, S. Linden, S. F. Mingaleev, L. Tkeshelashvili, and M. Wegener. Periodic nanostructures for photonics. *Physical reports Elsevier*, 444:101–202, 2007.

[32] James E. Smay, Joseph Cesarano, and Jennifer A. Lewis. Colloidal inks for directed assembly of 3-d periodic structures. *Langmuir*, 18(14):5429–5437, 2002.

[33] M. Deubel, G. von Freymann, M. Wegener, S. Pereira, K. Busch, and C. Soukoulis. Direct laser writing of three-dimensional photonic crystal templates for telecommunications. *Nature Materials*, 3:444, 2004.

[34] Georg von Freymann, Alexandra Ledermann, Michael Thiel, Isabelle Staude, Sabine Essig, Kurt Busch, and Martin Wegener. Three-dimensional nanostructures for photonics. *Advanced Functional Materials*, 20(7):1038–1052, 2010.

[35] Shigeki Takahashi, Katsuyoshi Suzuki, Makoto Okano, Masahiro Imada, Takeshi Nakamori, Yuji Ota, Kenji Ishizaki, and Susumu Noda. Direct creation of three-dimensional photonic crystals by a top-down approach. *Nature Materials*, 8:721–725, 2009.

[36] Li Wang, Sasa Zhang, Qingpu Wang, Jiaqi Chen, Wei Jiang, and Ray Chen. Fabrication of three-dimensional (3d) woodpile structure photonic crystal with layer by layer e-beam lithography. *Applied Physics A: Materials Science And Processing*, 95:329–334, 2009. 10.1007/s00339-009-5076-7.

[37] Isabelle Staude. personal communication, 2010.

[38] P. Kopperschmidt. Tetragonal photonic woodpile structures. *Applied Physics B: Lasers and Optics*, 76:729–734, 2003.

[39] Dennis W. Prather, Ahmed Sharkawy, Shouyuan Shi, Janusz Murakowski, and Garrett Schneider. *Photonic Crystals, Theory, Applications and Fabrication*. Wiley Publishing, 2009.

[40] Kazuaki Sakoda. *Optical Properties of Photonic Crystals*. Springer-Verlag, 2005.

[41] K. Inoue and K. Othaka. *Photonic Crystals: Physics, Fabrication and Design*. Springer-Verlag, 2004.

[42] Max Born and Emil Wolf. *Principles of optics*. Camebridge University Press, 7. expanded edition edition, 1999.

[43] H. S. Sözüer, J. W. Haus, and R. Inguva. Photonic bands: Convergence problems with the plane-wave method. *Phys. Rev. B*, 45(24):13962–13972, Jun 1992.

[44] `http://de.wikipedia.org/wiki/Brillouin-Zone`.

[45] Allen Taflove and Susan C. Hagness. *Computational Electrodynamics: The Finite-Difference Time-Domain Method*. Artech House, 2005.

[46] Steven Johnson and John Joannopoulos. Block-iterative frequency-domain methods for maxwell's equations in a planewave basis. *Opt. Express*, 8(3):173–190, Jan 2001.

[47] Hanfei Yan, Jörg Maser, Albert Macrander, Qun Shen, Stefan Vogt, G. Brian Stephenson, and Hyon Chol Kang. Takagi-taupin description of x-ray dynamical diffraction from diffractive optics with large numerical aperture. *Phys. Rev. B*, 76(11):115438, Sep 2007.

[48] T. K. Gaylord and M. G. Moharam. Planar dielectric grating diffraction theories. *Applied Physics B: Lasers and Optics*, 28:1–14, 1982. 10.1007/BF00693885.

[49] T.K. Gaylord and M.G. Moharam. Analysis and applications of optical diffraction by gratings. *Proceedings of the IEEE*, 73(5):894 – 937, May 1985.

[50] *DiffractMod User Guide.*

[51] Jens Als-Nielsen and Des McMorrow. *Elements of Modern X-Ray Physics.* John Wiley & Sons Ltd., 2001.

[52] André Authier. *Dynamical theory of x-ray diffraction.* Oxford university press, 2001.

[53] Boris W. Batterman and Henderson Cole. Dynamical diffraction of x rays by perfect crystals. *Rev. Mod. Phys.*, 36(3):681–717, Jul 1964.

[54] C. G. Darwin. Dynamical diffraction of x rays by perfect crystals. *Phil. Mag.*, 27:675, 1914.

[55] M. Deubel, M. Wegener, S. Linden, and G. von Freymann. Angle-resolved transmission spectroscopy of three-dimensional photonic crystals fabricated by direct laser writing. *Applied Physics Letters*, 87:1104–+, November 2005.

[56] John M. Dudley, Goëry Genty, and Stéphane Coen. Supercontinuum generation in photonic crystal fiber. *Rev. Mod. Phys.*, 78(4):1135–1184, Oct 2006.

[57] Lifeng Li. Multilayer modal method for diffraction gratings of arbitrary profile, depth, and permittivity. *J. Opt. Soc. Am. A*, 10(12):2581–2591, Dec 1993.

[58] Chung-Hsiang Lin, K. Ming Leung, and Theodor Tamir. Modal transmission-line theory of three-dimensional periodic structures with arbitrary lattice configurations. *Journal Optical Society America*, 19(10):2005, 2002.

[59] Lifeng Li. New formulation of the fourier modal method for crossed surface-relief gratings. *J. Opt. Soc. Am. A*, 14(10):2758–2767, Oct 1997.

[60] M. G. Moharam, Drew A. Pommet, Eric B. Grann, and T. K. Gaylord. Stable implementation of the rigorous coupled-wave analysis for surface-relief gratings: enhanced transmittance matrix approach. *J. Opt. Soc. Am. A*, 12(5):1077–1086, May 1995.

[61] Chung-Hsiang Lin, K. Ming Leung, and Theodor Tamir. Modal transmission-line theory of three-dimensional periodic structures with arbitrary lattice configurations. *J. Opt. Soc. Am. A*, 19(10):2005–2017, Oct 2002.

[62] Matlab 2008b. Matlab User Guide, 2008.

[63] Theodore T. Allen. *Introduction to engineering statistics and six sigma.* Springer-Verlag London, 2006.

[64] Isabelle Staude. personal communication, 2010.

[65] Isabelle Staude. personal communication, 2010.

[66] Alexander Schlösser. personal communication, 2009.

[67] R. Kowarschik. Diffraction efficiency of attenuated sinusoidally modulated gratings in volume holograms. *Optica Acta: International Journal of Optics*, 23:1039–1051, 1976.

[68] Shun-Der Wu, Thomas K. Gaylord, Elias N. Glytsis, and Yu-Ming Wu. Three-dimensional converging-diverging gaussian beam diffraction by a volume grating. *J. Opt. Soc. Am. A*, 22(7):1293–1303, Jul 2005.

[69] B. Brüser and U. Pietsch. Kinematic and dynamic light scattering from 3d photonic crystals. volume 7487, page 748709. SPIE, 2009.

[70] Alexander Schlösser. personal communication, 2010.

Acknowledgements

Eidesstattliche Erklärung

Hiermit versichere ich die vorliegende Arbeit selbstständig und unter ausschließlicher Verwendung der angegebenen Literatur und Hilfsmittel erstellt zu haben.

Die Arbeit wurde bisher in gleicher oder ähnlicher Form keiner anderen Püfungsbehörde vorgelegt und auch nicht veröffentlicht.

Siegen, 11.05.2011   _____

Curriculum Vitae